Simulation of Degradation Processes in Lithium-Ion Batteries

Maxim Taralov

Vom Fachbereich Mathematik der
Technischen Universität Kaiserslautern
zur Verleihung des akademischen Grades
Doktor der Naturwissenschaften
(Doctor rerum naturalium, Dr. rer. nat.)
genehmigte Dissertation

Datum der Disputation:
11. Mai 2015

1. Gutachter: Prof. Dr. Oleg Iliev
2. Gutachter: Prof. Dr. Arnulf Latz

D386

Acknowledgements

First and foremost, I would like to thank my supervisor Prof. Oleg Iliev for his support and guidance during my thesis.

The time and effort of my PhD Committee put into reviewing my thesis are also greatly appreciated.

I would like to express my gratitude towards Dr. Jochen Zausch and Prof. Arnulf Latz who were always willing to help me understand the physical aspects involved. Further, I would like to thank Prof. Raytcho Lazarov for the fruitful discussions that we had and his useful advices related to my work. I am also grateful to Prof. Yalchin Efendiev for the invitation to visit Texas A&M University and the hospitality while I was there. This visit gave me the opportunity to discuss topics related to my thesis with other researchers in this field.

I gratefully acknowledge Fraunhofer ITWM for the financial support provided for my thesis work.

I would also like to thank my colleagues from the Flow and Material Simulation department for creating a welcoming and fruitful working environment.

Last, but not least, I would like to thank my family and friends and especially my wife Vasilena Taralova for her continuous support.

Contents

Chapter 1

Introduction

In this chapter we lay the foundation for the rest of the thesis. We give the motivation behind simulating the operation of a Li-ion battery in Section 1.1. Specifically, we discuss why we are interested in simulating electrochemical and degradation phenomena inside them. To this end we also present the battery structure on the scale we consider in Section 1.2. In Section 1.3 we give a brief overview of degradation phenomena in batteries and state the main goals and results of the thesis. Finally, in Section 1.4 we summarize the structure of the thesis.

1.1 Motivation

In the last couple of decades there has been an exponential growth in the development and integration of portable consumer electronics in our everyday lives. Many of us cannot imagine what would we do without our smartphones, tablets or laptops. With the race for bigger and better screens, while decreasing thickness and weight of the devices, the need for designing batteries that are smaller but with higher capacity and longer calendar life is becoming more important for both consumers and the companies producing the electronics. And these are not the only places where one has a need for a battery. We can find batteries also in tools like drills, cars and even airplanes. For many of these applications manufacturers are turning to Lithium-ion batteries. This is due to their high energy density and long cyclability without the memory effects present in other types of rechargeable batteries.
However, with the increasing number of applications for Li-ion batteries, they are more and more pushed to their limits. Many of the main building blocks of the batteries are originally designed and tested only for small devices which

do not need very high currents. But since nowadays people also use them from high-end laptops to cars and airplane electronics, their actual uses can be in places where very high power is required. This necessitates additional testing procedures and verification for such applications. There are several notable failures in recent years where we can see the importance of careful investigation of the degradation processes in batteries. In 2006 laptops from several manufacturers, using certain Sony batteries had to be recalled due to catching fire [27]. In 2014 a whole line of Sony laptops, Vaio Fit 11A, had to be recalled for the same reason [93]. In 2013 all airline operators using the Boeing 787 Dreamliner had to ground the planes [77] due to problems with the lithium ion batteries leading to smoke and fire on some planes [25]. After an investigation, the reason for at least one of the incidents was determined as a short circuit in one of the battery cells, leading to a thermal runaway [68].

1.2 Battery fundamentals

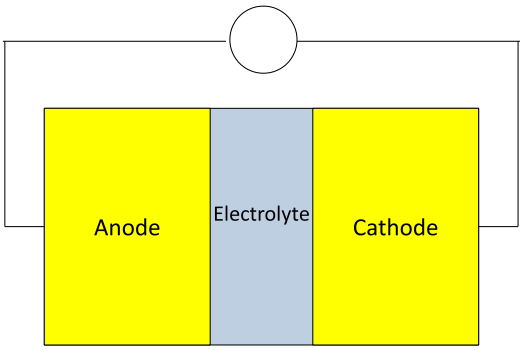

Figure 1.1: Macroscopic view of a battery cell

Here we give a short overview of the structure and operation of Li-ion batteries. For more details, see e.g. [63, 67]. Batteries in application are multiscale systems. We first focus on the scale we are interested in, and then explain where it fits in. We call this scale, the microscale.

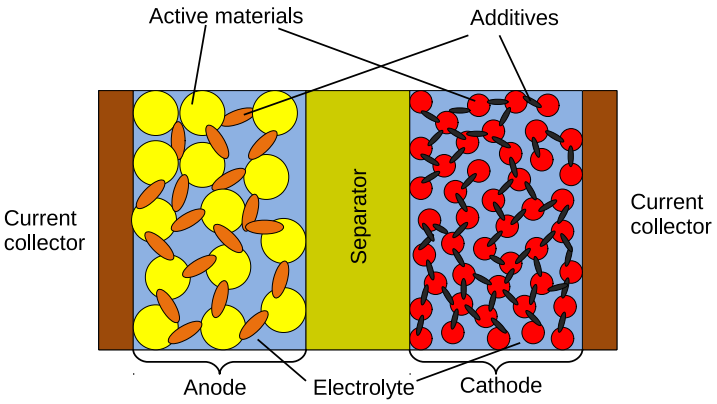

Figure 1.2: Microscopic view of a battery cell

The first thing to consider is the structure of a lithium-ion battery cell. In lithium ion batteries we have a negative and positive electrodes which are called anode and cathode, respectively (Figure 1.1). They are typically in the range of tens to hundreds of micrometers in thickness. Each electrode is composed of multiple solid particles connected together (Figure 1.2). These particles could be in the range of tens of nanometers to tens of micrometers. The space between the particles is filled with an ion-conducting non-aqueous electrolyte solution. Note that in some batteries the electrolyte can also be solid but we are not considering such types of batteries currently. Between the two electrodes there is a porous separator making sure they do not touch and short-circuit the battery. In order to improve certain properties like electrical conductivity some additives are usually mixed with the active material or special coatings can be applied on the particles. Binders are needed to keep the structure intact and connected to the rest of the battery. Each electrode connects to the outside world through the metallic current collectors. After the description of the main building blocks of a battery cell, let us also explain briefly how all these components fit together in action.
Both the anode and the cathode are materials which can accommodate lithium in their structure. The process of lithium insertion into the electrode material is called intercalation. The inverse process when the lithium leaves the active material is called deintercalation. Both processes are initiated when an electric current flows between the two current collectors. When the device we need to power is turned on (i.e. discharging the battery), positively charged lithium ions are formed in the anode. They leave the active material for the electrolyte, move through the separator and ultimately intercalate into the cathode. The corresponding electrons leave the battery through the current collector and travel through the external circuit to the

cathode since they cannot enter the electrolyte. Also due to lithium being highly reactive with water, the electrolyte is a non-aqueous organic solution. When we charge the battery, the opposite happens and the lithium ions move from the cathode to the anode. The transport in the electrodes themselves can be quite complex. While mainly modeled as diffusion, in some types of materials there are also other phenomena occurring. For example in lithium iron phosphate ($LiFePO_4$) according to some experiments larger particles can charge before smaller particles [33]. In silicon there are recent experiments which indicate a loading regime where first the whole particle is charged to a partial state ($Li_{2.5}Si$), before the full capacity ($Li_{3.5}Si$) is reached at any point [98]. Also sharp gradients in the lithium concentration can be observed.
The final important component to note are the electrochemical surface reactions between the solid particles and the electrolyte. They are responsible for the intercalation and deintercalation of lithium from and to the electrolyte. Also, during the first couple of charge-discharge cycle, on the surface of the particles in the anode a solid-electrolyte interphase layer (SEI layer) forms. This is due to chemical reactions of the organic solvent with the lithium. In the formation of the SEI layer some lithium is lost.
Let us now specify where our material-resolved microscopic view of the battery cell stands among the different scales of the battery. A schematic is shown in Figure 1.3

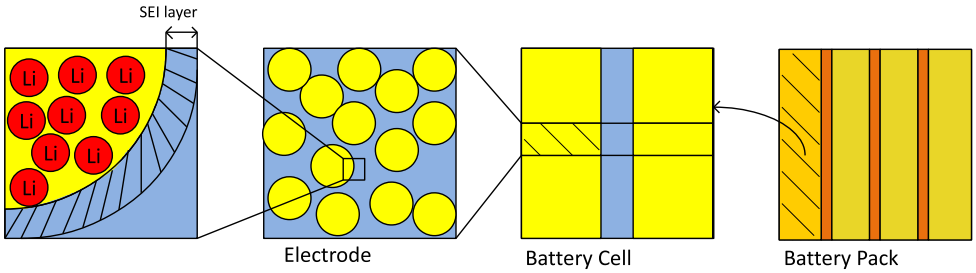

Figure 1.3: Multiple scales of a battery

One could go further down, to even smaller scales, where kinetic effects can be considered for single particles. We could also include a spatially resolved SEI layer. We consider the surface kinetics right now as simply occurring on a domain with zero volumetric measure and include them as a surface reaction. When we go in the other direction, we can see that the battery cell is usually much bigger in the other two directions compared to the thickness. These cells are stacked next to each other in a battery pack. In some big

batteries (e.g. in electromobility) multiple such packs can also be stacked together.

1.3 Degradation processes and main contribution of the thesis

In this section we start with a brief overview of some degradation mechanisms and how they could affect the operation of the battery, and then specify our main focus and the contribution of this work.
The degradation processes can lead to capacity fade or unsafe operating conditions. It has been shown that high currents and low temperatures can result in plating, which is to say that a Li-metal layer can form on the surface of the active particles at the anode [46]. This of course results in reduced capacity of the battery. Should this process continue, dendrites can form on the metal layer [2]. If these dendrites grow enough they can puncture the porous separator and connect the two electrodes, resulting in a short-circuit which in turn may lead to ignition of the electrolyte. However, our main focus is on the deterioration of the electrode materials. Such an effect could be a result of thermal processes [51, 80] or even the intercalation of lithium. Due to the change in composition of the materials resulting from intercalation and deintercalation of lithium, a series of important effects can be observed. These include the volumetric changes of the particles [100, 4], the internal mechanical forces, i.e. stresses induced by the process, fracturing and pulverization of the active particles [78], change of the structure of the underlying material, e.g. crystalline to amorphous [62] etc. In some materials these effects are especially pronounced. For example in silicon electrodes the volume expansion can reach 300-400% [4] and macroscopic cracks can form after only a small number of charge/discharge cycles. While not as severe as silicon, every electrode material degrades with time and cracks appear [99]. This results in loss of capacity since on the new interfaces a new SEI layer has to be formed. It can also result in reduced or lost connectivity between particles. For additional degradation mechanisms, see e.g. [96, 14, 100, 2], etc.
The main contribution of this work is the numerical solution of several electrochemical and mechanical models and comprehensive numerical study of related degradation phenomena in a realistic three dimensional setting. This is accomplished using a finite element method framework, developed in C++ as part of this thesis. Several important contributions of this thesis are

- Simulation of the isothermal model [59] in three dimensions and a com-

parative study between finite element method solution and voxel based finite volume method solution

- Simulation of the non-isothermal model [58] and study of the behavior of the temperature and heat sources
- Coupling of the full electrochemical model from [59] to the small strain model from [105] and numerical study of the resulting model
- Comparison between two finite strain elastic models to study the sensitivity of the intercalation induced deformation and its related quantities on the mechanical model
- Reproducing the general behavior of mechanical stress from certain experimental results of Silicon [84], using finite strain elastic models and taking into account the softening of the Silicon anode with respect to the li-ion concentration

First, we present and solve an isothermal electrochemical model [59] on the microscale level, which is subsequently also used as part of a more complicated simulation with coupling to a linear elasticity model. We also do a comparative study between FEM and voxel based FVM on this model to illustrate the sensitivity of the solution on the discretization. The next model considered is the thermal extension of the previous one proposed by Latz et al. [58]. The author of the thesis also used this model as the basis for simulation of non-isothermal electrochemical processes in a two dimensional setting in his master thesis [90]. However the previous study was restricted to relatively small problems in 2D. In that sense there was no way to simulate a realistic porous electrode. Although we do not consider degradation phenomena related to temperature increase in our current simulations, it is nevertheless important that we can capture the thermal effects as they can be used as a starting point in future simulations. Therefore the fact that we can simulate the model on 3D geometries is important, because we can observe individual heat sources and assess any possible hotspots. Due to the specifics of our setting, the temperature in this model shows mainly a macroscopic behavior. This allows us to recast it as an ODE, which is also a contribution of this work. That significantly reduces the effort required to solve the heat equation, since we no longer need to solve a system of equations on each time step. After the non-isothermal simulations we shift our focus on mechanical models and specifically the effect of intercalation on mechanical stresses. We consider both small and large deformation models. For the small deformations, we use a model proposed in the context of batteries by Zhang et al.

[105]. We first use it as given to test individual particles and then couple it to the full electrochemical model by Latz et al. [59] to simulate a more realistic scenario. Finally, we study large elastic deformations, using two elastic finite strain mechanical models. The first relates the second Piola-Kirchhoff stress to the Green-Lagrange strain and the second – the Cauchy stress to the logarithmic strain. For both mechanical models, we use concentration dependent Young's modulus and expansion coefficient. The second model is similar to the one proposed by Zhao et al. [106] for elasto-plastic deformations resulting from lithium intercalation in silicon electrodes. For all of these models we run comprehensive numerical studies using different admissible geometries and operating regimes. They are solved using isoparametric finite element method in three dimensional setting. We built the code for the discretization of the PDEs from the ground up.

1.4 Structure of the thesis

In this section we give a short summary for each of the remaining chapters. Since with this thesis we try to approach also physicists, engineers and chemists working in the field, there are some known mathematical results given for self-consistency.

In Chapter 2 the main focus is to give a brief overview of the different mathematical methods that we employ and the way we use them. There are no original results in this chapter. First we describe the method that we use for spatial discretization of the partial differential equations - the finite element method. A general overview of going from strong to weak form is given and then several specific aspects of the FEM itself, like the structure of the trial and test spaces. The advantage of using isoparametric finite elements is also addressed. Following the spatial discretization is the time discretization since we are dealing with time dependent problems. The method that we use and explain is the backward Euler method. It is an implicit method that results in a system of algebraic equations that needs to be solved. In many of the PDEs that we consider these equations are nonlinear. In fact the same holds true also for some of the quasi-static equations that we use. In order to solve them we linearize the system using the Newton method. A brief derivation of the method as well as the resulting algorithm are present in the relevant section. Since some of the models are easier to linearize using directional derivatives, there is also a section on this subject. Rounding up the mathematical preliminaries section is a short overview of tensor algebra, necessary for some of the mechanical models.

In Chapter 3 we present the two electrochemical models for the full bat-

tery cell that we use – the isothermal [59] and the non-isothermal [58] ones. We begin the chapter with a brief state of the art for electrochemical models. We follow this with description of the models, setting, parameters and assumptions we make. The models describe the behavior of lithium concentration and electrical potential in three distinct regions – anode, cathode and electrolyte. The non-isothermal model also has an additional unknown quantity – the temperature. Based on the results we obtain from the numerical simulations of the non-isothermal model, namely that we observe no spatial variations of the temperature, we also present an ODE form of the heat equation. After presenting the PDEs in strong form we then derive the weak form. This weak form is discretized using the methods discussed in Chapter 2. However, since the models describe functions that are discontinuous on the interfaces between the different media, we also present in more detail the necessary considerations stemming from this fact. After the discretization we continue with our numerical results. We run numerical experiments using different realistic working regimes and geometries.

In Chapter 4 the attention is on the mechanical stresses and effects resulting from the intercalation of lithium in the particles. In order to facilitate a clearer explanation of the chemomechanical models, we first describe some preliminaries from continuum mechanics. The initial explanation is presented on a general setting where we do not assume anything about the scale of the deformation. When linear elasticity is later introduced we make the simplification of having only small deformations and a single geometry as well as specific linearizations applicable to this setting. However, since we also use finite strain models with large deformations the general approach is also used without any simplifications. After giving the mechaincs specific information we present the models we use. They are described in separate sections. The first model is a small strain model where the intercalation dependence is included using an additive decomposition of the linearized strains. The other model is a large strain model where we account for the concentration influence using a multiplicative decomposition of the deformation gradient. For both models we also give detailed discretizations and solution specifics. Numerical studies are performed for the two models.

Chapter 5 is dedicated to the computer implementation and the difficulties that we encountered with it. We give a brief explanation of the interfaces that are key in building a new problem. An overview of the tradeoffs that we chose between ease of use and speed are given. We also show a numerical verification of the main building blocks of the program by solving a simple problem with the different finite elements that we use for the simulations in the other chapters.

In Chapter 6 we discuss shortly the results from the previous chapters.

Chapter 2

Mathematical preliminaries

In the current chapter there are no new results, but rather we present for completeness and self-consistency the necessary mathematical apparatus. The presentation is based on the classical textbooks [37, 76, 20, 13, 75, 42, 109, 29, 69, 7].
For a simple demonstration of the process of going from a PDE in strong formulation to a discretized problem, we use a model problem given in Section 2.1. We start with the weak formulation and the solution spaces in Section 2.2. Then we present the numerical methods which we use to solve our physical models. They are explained in the order of generality for our uses. We start with the spatial discretization method which we use for all the models we consider, namely the finite element method (Section 2.3). For time discretization we use the Backward Euler Method, described in Section 2.4. Since many of our models include nonlinearities we use the Newton method for solving the nonlinear algebraic systems obtained after discretization (Section 2.5). In some of the models considered, it is easier to develop the linearized equations in the terms of directional derivatives, so in Section 2.6 we give a brief presentation on them. Finally, in Section 2.7 we show some necessary properties and operations on vectors and tensors.
Note that due to the introductory nature of this chapter, we usually provide only a couple of references per section, where most of the presented material can be found in detail. We give additional references for points, which are possibly either not addressed in the reference material or which we want to emphasize on.

2.1 Model problem

For ease of explanation we use the diffusion equation to illustrate the different methods and formulations. In strong form it is given by

$$u_t - \nabla \cdot (D(u, \mathbf{x})\nabla u) = f(\mathbf{x}, t), \qquad (\mathbf{x}, t) \in \Omega \times [0, T] \tag{2.1}$$
$$u(\mathbf{x}, t) = g(\mathbf{x}, t), \qquad (\mathbf{x}, t) \in \Gamma_D \times [0, T] \tag{2.2}$$
$$-D(u, \mathbf{x})\nabla u(\mathbf{x}, t) \cdot \mathbf{n} = b(u, \mathbf{x}, t), \qquad (\mathbf{x}, t) \in \Gamma_N \times [0, T] \tag{2.3}$$
$$u(\mathbf{x}, 0) = u_0(\mathbf{x}), \qquad (\mathbf{x}, t) \in \Omega \times \{0\} \tag{2.4}$$

where Ω is a given region with sufficiently regular boundary, Γ_D and Γ_N are the parts of the boundary of Ω in which we have Dirichlet and Neumann boundary conditions respectively. The diffusion coefficient D can be a full matrix in cases when the speed of diffusion is dependent on the direction, but here we consider it as a scalar coefficient. It is also assumed to be sufficiently smooth and strictly positive, i.e. $D(\mathbf{x}) > 0$. If D becomes negative, this equation is called anti-diffusion equation and it is notoriously unstable. For a strong solution, obviously if $f(\mathbf{x}, t) \in C(0, T; C(\Omega))$, then $u(\mathbf{x}, t) \in C(0, T; \{C^2(\Omega) \cap C^0(\bar{\Omega})\})$, $u_t \in C(0, T; C(\Omega))$. Note, that this regularity can be relaxed if instead of requiring the function u be $C^2(\Omega)$ in space, we require the flux $D\nabla u$ to be $C^1(\Omega)$.

2.2 Weak formulation

Requiring a classical solution from a PDE can many times be a too strong condition as such solution might not exist even for PDEs describing real physical phenomena. In order to relax the requirements on the regularity of the solution we recast the problem in weak formulation. In order to do so let us multiply (2.1) by a test function $\psi(\mathbf{x})$ and integrate over the domain Ω:

$$\int_\Omega u_t \psi \mathrm{d}v - \int_\Omega \psi \nabla \cdot (D\nabla u)\mathrm{d}v = \int_\Omega f\psi \mathrm{d}v \tag{2.5}$$

and we have for the second term

$$\begin{aligned} -\int_\Omega \nabla \cdot (D\nabla u)\psi \mathrm{d}v &= -\int_\Omega \nabla \cdot (\psi D\nabla u)\mathrm{d}v + \int_\Omega D\nabla u \cdot \nabla\psi \mathrm{d}v \\ &= -\int_{\partial\Omega} \psi D\nabla u \cdot \mathbf{n}\mathrm{d}a + \int_\Omega D\nabla u \cdot \nabla\psi \mathrm{d}v \end{aligned} \tag{2.6}$$

We pick the test function $\psi(\mathbf{x})$ to have zero trace on the Dirichlet part of the boundary and hence the boundary integral in (2.6) is only over the Neumann part of the boundary. We substitute (2.3) in the first term of (2.6) and the result is then used in (2.5) to obtain

$$\int_{\Omega} u_t \psi \mathrm{d}v + \int_{\partial\Omega} \psi b \mathrm{d}a + \int_{\Omega} D\nabla u \cdot \nabla\psi \mathrm{d}v = \int_{\Omega} f\psi \mathrm{d}v \tag{2.7}$$

It is obvious now that in this weak form we greatly reduced the requirements on u since we no longer have second derivatives and all the terms are integrals, meaning that we can have discontinuities on sets with measure zero with respect to the measure of the integral. In that sense we use the functional spaces

$$L_2(\Omega) = \{u(\mathbf{x}) | \int_{\Omega} u^2 \mathrm{d}v < \infty\} \tag{2.8}$$

and

$$H^1(\Omega) = \{u(\mathbf{x}) | u \in L_2(\Omega), \nabla u \in (L_2(\Omega))^{dim}\}. \tag{2.9}$$

Namely L_2's elements are functions which are square integrable and H^1's elements are functions, which together with their first derivatives are in L_2. These derivatives are meant in the weak sense. The specific trial space where we look for $u(\mathbf{x})$ is

$$u(\mathbf{x}, t) \in L_2(0, T; H^1_D(\Omega)), \quad u_t(\mathbf{x}, t) \in L_2(0, T; H^{-1}(\Omega)) \tag{2.10}$$

where

$$H^1_D(\Omega) = \{u(\mathbf{x}) | u \in H^1(\Omega), u(\mathbf{x}) = g(\mathbf{x}), \mathbf{x} \in \Gamma_D\} \tag{2.11}$$

i.e. H^1 functions which satisfy our Dirichlet boundary conditions in the trace sense. For the test space we pick

$$\mathcal{V} = \{u(\mathbf{x}) | u \in H^1(\Omega), u(\mathbf{x}) = 0, \mathbf{x} \in \Gamma_D\} \tag{2.12}$$

i.e. functions with zero trace on the Dirichlet boundary.
Let us simplify a little the notation by introducing the $L_2(\Omega)$ product

$$(u, v)_{L_2(\Omega)} = \int_{\Omega} u\psi \mathrm{d}v \tag{2.13}$$

and the form

$$a(u,v) = \int_{\Omega} D(u,\mathbf{x})\nabla u \cdot \nabla \psi \mathrm{d}v \tag{2.14}$$

Then (2.7) becomes

$$(u_t, v)_{L_2(\Omega)} + a(u,v) + (b,v)_{L_2(\partial\Omega)} = (f,v)_{L_2(\Omega)} \tag{2.15}$$

We do not go here in more detail about weak and strong solutions of PDEs, for more information, see [37], [76].

2.3 Finite element method

For spatial discretization of our PDEs we use the finite element method [20]. We construct a finite dimensional space to use instead of the original infinite dimensional functional space, i.e. $V_h \subset \mathcal{V}$. We are using only conforming finite elements. This means that our discrete space is a subspace of the original functional space. The basic idea is that we divide our given geometry into smaller and simpler shapes (often simpleces) called elements. We define a set of functions (usually polynomials) called shape functions, which we use for the local approximation of the unknown quantities over each element. Finally, we fix a set of functionals to describe the values which we want to obtain (e.g. nodal values of the functions or their derivatives). Let us denote by $\mathcal{T}_h$ the partition of Ω into elements. We define the local interpolant of $u(\mathbf{x})$ in the element $\tau \in \mathcal{T}_h$ to be

$$u_h(\mathbf{x},t)|_\tau = \sum_{i=1}^{k} u_i(t)\varphi_i(\mathbf{x}) \tag{2.16}$$

where k is the number of shape functions in each element, φ_i are the shape functions themselves and u_i are the coefficients which correspond to the values of the functionals. The global interpolant is just the union of all local interpolants

$$u_h(\mathbf{x},t) = u_h(\mathbf{x},t)|_\tau, \quad \mathbf{x} \in \tau, \quad \text{f.e. } \tau \in \mathcal{T}_h \tag{2.17}$$

i.e. for $\mathbf{x} \in \Omega$ we calculate the local interpolant over the element in whose domain $\mathbf{x}$ belongs.
For the shape functions we use polynomials. The elements we consider are Lagrangian, i.e. we are solving for the nodal values. The specific element

types are P1 (triangles or tetrahedra) and Q1 (quadrilaterals and hexahedra). Each global basis function related to a specific node is the union of the local shape functions related to this node. We form a partition of unity basis $\{\varphi_i\}_{i=1}^N$. Namely for the basis function φ_i we have that it has a compact support and

$$\sum_{i=1}^{N} \varphi_i(\mathbf{x}) = 1, \quad \mathbf{x} \in \Omega \tag{2.18}$$

where N is the number of nodes in the mesh. Furthermore, the basis we consider is an interpolating basis, i.e.

$$\varphi_i(\mathbf{x}_j) = \delta_{ij} \tag{2.19}$$

where δ_{ij} is the Kronecker delta. This means that with each node we associate a basis function. In this way we can also define our global interpolant like

$$u_h(x,t) = \sum_{i=1}^{N} u_i(t)\varphi_i(\mathbf{x}) \tag{2.20}$$

These basis functions have local support, restricted only to the elements which contain the node, the specific basis function is related to, i.e.

$$supp(\varphi_i) = \bigcup_{k:\mathbf{x}_i \in \tau_k} \tau_k \tag{2.21}$$

This means that when we substitute the interpolation in (2.15) we can calculate the integrals in an element-wise fashion. We are also using the same spaces for the trial function and the test function. This is known as the Galerkin method. We test with all basis functions from our discrete space to obtain the following system of equations

$$\left(\sum_{j=1}^{N} u_{j,t}\varphi_j, \varphi_i\right) + a\left(\sum_{j=1}^{N} u_j\varphi_j, \nabla\varphi_i\right) + (b, \varphi_i)_{L_2(\Omega)} = (f, \varphi_i)_{L_2(\Omega)} \tag{2.22}$$

For the simplex elements we can build the basis directly on the original mesh by using the interpolation property (2.19). For the Q1 elements however this would not give us a conforming element. Indeed, on a single quadrilateral element we have the following interpolation for our function u

$$u_h = u_i\varphi_i = a_0 + a_1x + a_2y + a_3xy \tag{2.23}$$

Let us now take an element which has as one of its sides the line $y = x$. When we restrict the local interpolant on this line we get a quadratic function in one of the variables

$$u_h = a_0 + (a_1 + a_2)x + a_3x^2 \tag{2.24}$$

If we do the same for the adjoining element who shares this edge we also get a quadratic function. However, we only have two conditions on this edge, namely the values of the function in the nodes. This means that our quadratic functions are not uniquely defined and hence might not coincide on the edge from the two sides. Therefore we use isoparametric finite elements to ensure that we have a conforming method as explained in the next section (2.3.1).
We briefly mention that for linear problems, when using polynomials of order n, i.e. P_n for the shape function, the standard error estimates [13] are

$$||u - u_h||_{L_2} \leq Ch^s|u|_{H^s(\Omega)} \tag{2.25}$$

and

$$||u - u_h||_{H^1} \leq Ch^{s-1}|u|_{H^s(\Omega)} \tag{2.26}$$

where h is a characteristic length of the mesh and we assume that $u \in H^s(\Omega)$ for $2 \leq s \leq n$. We also mention for completeness that

$$||u - u_h|| = 0 \tag{2.27}$$

when u is an element of the finite dimensional space, i.e. $u \in V_h$.

2.3.1 Isoparamteric FEM

In isoparametric FEM [75] we use a reference element in addition to the real elements for most of the calculations. The shape functions are defined in terms of the reference element and we compute the integrals using a transformation from the reference to the real elements. The integrals themselves are computed using quadrature formulas. We use the quadrature points and weights given in [26],[45]. Later we show that using isoparametric finite elements, we obtain a continuous interpolant also for the Q1 elements. Let us now illustrate the process in 2D for simplicity, since it is analogous in 3D.
First we start with the transformation between the reference coordinates

(ξ, η) to real coordinates (x, y)

$$x(\xi,\eta) = \sum_{i=1}^{k} x_i \varphi_i(\xi,\eta)$$
$$y(\xi,\eta) = \sum_{i=1}^{k} y_i \varphi_i(\xi,\eta) \tag{2.28}$$

where $\varphi_i(\xi, \eta)$ are the shape functions over the reference element, and (x_i, y_i) are the coordinates of the nodes of the real elements. We say that these elements are isoparametric, since we have the same order of polynomials for both the transformation and for the interpolation of the solution

$$u_h(\xi,\eta) = \sum_{i=1}^{k} u_i \varphi_i(\xi,\eta) \tag{2.29}$$

If the order of interpolation was higher or lower than the transformation, we would call this elements sub- or superparametric respectively. The integration is performed as

$$\int_{\tau_k} u(x,y)v(x,y)\mathrm{d}v = \int_{E} u(\xi,\eta)v(\xi,\eta)\det(\mathbf{J})dE \tag{2.30}$$

where τ_k is an element from the discretized geometry, E is the domain of the reference element and $\mathbf{J}$ is the Jacobi matrix of the transformation given by

$$\mathbf{J} = \begin{pmatrix} \dfrac{\partial x}{\partial \xi} & \dfrac{\partial x}{\partial \eta} \\ \dfrac{\partial y}{\partial \xi} & \dfrac{\partial y}{\partial \eta} \end{pmatrix} = \begin{pmatrix} \displaystyle\sum_{i=1}^{k} x_i \frac{\partial \varphi_i(\xi,\eta)}{\partial \xi} & \displaystyle\sum_{i=1}^{k} x_i \frac{\partial \varphi_i(\xi,\eta)}{\partial \eta} \\ \displaystyle\sum_{i=1}^{k} y_i \frac{\partial \varphi_i(\xi,\eta)}{\partial \xi} & \displaystyle\sum_{i=1}^{k} y_i \frac{\partial \varphi_i(\xi,\eta)}{\partial \eta} \end{pmatrix} \tag{2.31}$$

and hence the integration of the integrals in front of the time derivatives is simply

$$\int_{\tau_k} \varphi_j(x,y)\varphi_i(x,y)\mathrm{d}v = \int_{E} \varphi_j(\xi,\eta)\varphi_i(\xi,\eta)\det(\mathbf{J})dE \tag{2.32}$$

However for the integration of

$$\int_{\Omega} D\nabla\varphi_i \cdot \nabla\varphi_j \mathrm{d}v \tag{2.33}$$

we also need the derivatives of the basis functions. Explicitly inverting the transformation (2.28) can often times be intractable. In that sense it is better to look at it another way. Let us examine the derivatives of $\varphi(x, y)$ with respect to ξ and η. We have from the chain rule

$$\frac{\partial \varphi}{\partial \xi} = \frac{\partial \varphi}{\partial x}\frac{\partial x}{\partial \xi} + \frac{\partial \varphi}{\partial y}\frac{\partial y}{\partial \xi} \tag{2.34}$$

$$\frac{\partial \varphi}{\partial \eta} = \frac{\partial \varphi}{\partial x}\frac{\partial x}{\partial \eta} + \frac{\partial \varphi}{\partial y}\frac{\partial y}{\partial \eta} \tag{2.35}$$

which is equivalent to

$$\begin{pmatrix} \frac{\partial \varphi}{\partial \xi} \\ \frac{\partial \varphi}{\partial \eta} \end{pmatrix} = \mathbf{J}^T \begin{pmatrix} \frac{\partial \varphi}{\partial x} \\ \frac{\partial \varphi}{\partial y} \end{pmatrix} \tag{2.36}$$

from where we obtain

$$\begin{pmatrix} \frac{\partial \varphi}{\partial x} \\ \frac{\partial \varphi}{\partial y} \end{pmatrix} = \mathbf{J}^{-T} \begin{pmatrix} \frac{\partial \varphi}{\partial \xi} \\ \frac{\partial \varphi}{\partial \eta} \end{pmatrix} \tag{2.37}$$

For the boundary integrals, the transformation is with one dimension lower, i.e. in 3D we have a two-parameter surface and in 2D we have a one parameter curve. We show the transformation in 3D

$$x(\zeta, \chi) = \sum_{i=1}^{l} x_i \psi_i(\zeta, \chi) \tag{2.38}$$

$$y(\zeta, \chi) = \sum_{i=1}^{l} y_i \psi_i(\zeta, \chi) \tag{2.39}$$

$$z(\zeta, \chi) = \sum_{i=1}^{l} z_i \psi_i(\zeta, \chi) \tag{2.40}$$

The boundary integral thus becomes

$$\int_{\gamma_k} b(u_h, x, y, z) v(x, y, z) da = \int_S b(\zeta, \chi) v(\zeta, \chi) ||r_\zeta \times r_\chi|| dS \tag{2.41}$$

where γ_k is part of the discretized boundary of the domain, S is a reference surface element, and r_ζ and r_χ are given by

$$r_\zeta = \left(\frac{\partial x}{\partial \zeta}, \frac{\partial y}{\partial \zeta}, \frac{\partial z}{\partial \zeta}\right) \tag{2.42}$$

$$r_\chi = \left(\frac{\partial x}{\partial \chi}, \frac{\partial y}{\partial \chi}, \frac{\partial z}{\partial \chi}\right) \tag{2.43}$$

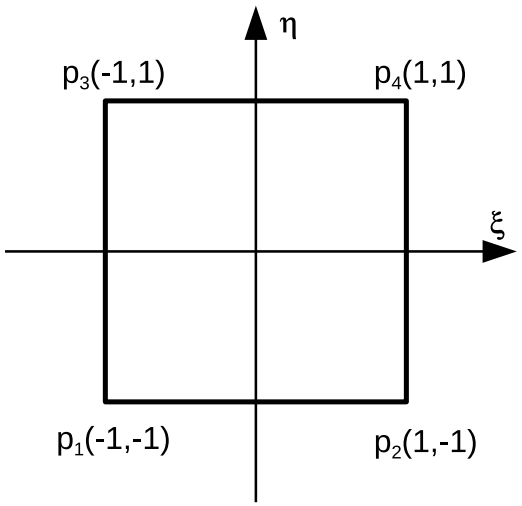

Figure 2.1: Standard quadrilateral element

Let us now verify the assertion from the previous section that the isoparametric Q1 elements provide a continuous approximation between elements. The Q1 quadrilateral 2D element is shown in Figure 2.1. The shape functions associated with nodes $p_1, \ldots, p_4$ are

$$\varphi_1(\xi, \eta) = \frac{1}{4}(1-\xi)(1-\eta) \tag{2.44}$$

$$\varphi_2(\xi, \eta) = \frac{1}{4}(1+\xi)(1-\eta) \tag{2.45}$$

$$\varphi_3(\xi, \eta) = \frac{1}{4}(1-\xi)(1+\eta) \tag{2.46}$$

$$\varphi_4(\xi, \eta) = \frac{1}{4}(1+\xi)(1+\eta) \tag{2.47}$$

In that case the interpolant over a specific element is

$$\begin{aligned} u_h(\xi, \eta) =& u_1 \frac{1}{4}(1-\xi)(1-\eta) + u_2 \frac{1}{4}(1+\xi)(1-\eta) + \\ & u_3 \frac{1}{4}(1-\xi)(1+\eta) + u_4 \frac{1}{4}(1+\xi)(1+\eta) \end{aligned} \tag{2.48}$$

Let us now assume that the side p_3p_4 maps to $x = y$. Considering the side p_3p_4 is equivalent to setting $\eta = 1$. The resulting interpolation for $u(x)$ over this side is then

$$u_h(\xi, \eta)|_{p_3p_4} = u_3\frac{1}{2}(1-\xi) + u_4\frac{1}{2}(1+\xi) \tag{2.49}$$

which is a linear function. Since we have two parameters u_3 and u_4, the interpolant is uniquely defined.
There are some restrictions on the positioning of the vertices of the real element. Since we want to have a strictly positive Jacobian of the transformation, in quadrilateral elements for example, all the angles must be smaller than 180 degrees.
An interesting note can be made about the use of higher order elements. As previously mentioned a higher order polynomial in the function interpolant gives higher order L_2 and H^1 estimates. In the case of isoparametric elements, however, we use these higher order polynomials also for the transformation between the reference and real element. By analogy to the consideration of the previous paragraph to Q1 elements, one can also use elements with curved sides and still obtain continuous interpolant. This allows us to get much better approximations to curved boundaries for example. There are also additional restrictions on where we can place the non-vertex nodes. As previously - we want the Jacobian of the transformation to be strictly positive, but also with improper placement we can influence the interpolant and its derivatives. In some special cases this can be exploited for e.g. simulation of solutions with singular first derivatives [3].

2.4 Backward Euler method

For the time discretization we use the implicit backward Euler method [42]. It is easiest to derive by integrating both sides in an ODE with respect to time in the interval $[t_n, t_{n+1}]$ and then approximating the necessary integrals. Specifically, for the backward Euler we have for the ODE $u_t = f(u, t)$

$$\int_{t_n}^{t_{n+1}} u_t \mathrm{d}t = \int_{t_n}^{t_{n+1}} f(u,t)\mathrm{d}t \tag{2.50}$$

The time differential integrates exactly as $\int_{t_n}^{t_{n+1}} u_t \mathrm{d}t = u(t_{n+1}) - u(t_n)$ whereas we approximate the right hand side integral with the value on the right side

of the integration interval, i.e.

$$\int_{t_n}^{t_{n+1}} f(u,t)\mathrm{d}t = f(u^{n+1}, t_{n+1})\Delta t \tag{2.51}$$

where $\Delta t = t_{n+1} - t_n$ and $u^n = u(t_n)$. This gives an unconditionally stable method with an $O(\Delta t)$ accuracy for linear problems. The downside is that we have to solve a possibly nonlinear equation to obtain the solution on the current time step. We could also take the value on the other side of the interval to obtain the explicit Euler method, but since it is only conditionally stable, it needs to satisfy a certain condition which can be very restrictive for nonlinear PDEs. We could also use the second order trapezoid rule for the integration to obtain the second order accurate Crank-Nicholson method, but it can become unstable for nonlinear problems [20]. Finally, for our model problem the fully discretized equations are

$$\sum_{j=1}^{n} \frac{u_j^{n+1} - u_j^n}{\Delta t}(\varphi_j, \varphi_i) + a(\sum_{j=1}^{N} u_j^{n+1}\varphi_j, \varphi_i) + (b, \varphi_i)_{L_2(\partial\Omega)} = (f, \varphi_i)_{L_2(\Omega)} \tag{2.52}$$

The matrix

$$\mathbf{M}_{ij} = \frac{(\varphi_j, \varphi_i)}{\Delta t}, \quad i,j = 1, \ldots, N \tag{2.53}$$

is called mass matrix. In our calculations we mostly use lumped mass matrices where we sum the coefficients in each row

$$\mathbf{M}^L = \mathrm{diag}(m_{ii}^L) \tag{2.54}$$

$$m_{ii}^L = \frac{1}{\Delta t}\sum_{j=1}^{N}(\varphi_j, \varphi_i) = \frac{1}{\Delta t}\left(\sum_{j=1}^{N}\varphi_j, \varphi_i\right) = \frac{1}{\Delta t}(1, \varphi_i) = \frac{1}{\Delta t}\int_\Omega \varphi_i \mathrm{d}v \tag{2.55}$$

For explicit methods this is useful, in order to remove the necessity of solving a system of equations on each time step. In our case we use it to reduce oscillations in the solution. We address this shortly in subsection 2.4.1. For linear diffusion problems, this does not impact negatively the convergence rate [16]. For convection-dominated transport, the consistent mass matrix (or appropriate corrections to the solution if using lumped matrix) might be more suitable due to unwanted effects accumulating in the solution [109].
However, let us assume now that we have no nonlinearities in both the diffusion coefficient and the boundary conditions to give a better idea of the

structure of the discretized problem. We already introduced the mass matrix $\mathbf{M}$, so let us now introduce the stiffness matrix. It is defined as

$$\mathbf{K}_{ij} = a(\varphi_i, \varphi_j), \quad i, j = 1, \dots, N \tag{2.56}$$

i.e. it contains the elements of the discretization of the diffusion term (the one with the second order derivatives). Our right hand side is the sum of the discretized source term $f(x)$ and the boundary intergrals over the Neumann boundaries

$$\mathbf{F}_i = (f, \varphi_i)_{L_2(\Omega)} - (b, \varphi_i)_{L_2(\partial\Omega)}, \quad i = 1, \dots, N \tag{2.57}$$

This gives us our discretized PDE in matrix notation as

$$(\mathbf{M} + \mathbf{K})\mathbf{u} = \mathbf{F} \tag{2.58}$$

To impose the Dirichlet boundary conditions we do the following

$$\mathbf{A}_{ij} = \delta_{ij}, \quad i : \mathbf{x}_i \in \Gamma_D \tag{2.59}$$

$$\mathbf{F}_i = g(\mathbf{x}_i, t), \quad \mathbf{x}_i \in \Gamma_D \tag{2.60}$$

That is, for all nodes on the Dirichlet boundary, where we know the value of the function, we modify the matrix to have one on the main diagonal and zero at all other positions and set the right hand side to the known value. If the matrix was originally symmetric, we can preserve this property by substituting the known values in the rest of the equations and subtract the result from the right hand side.

2.4.1 Maximum principle

We give a very brief discussion on the discrete maximum principle (DMP), since we have time dependent problems and use 3D tetrahedral geometries. Both of them could lead to violation of the DMP and thus bring oscillations in the numerical solution. For a more thorough explanation consult e.g. [55]. Let us first start by considering the continuous maximum principle for linear elliptic operators. Let us define the full elliptic operator as

$$Lu(x) = -\sum_{i,j=1}^{d} a_{ij}(x)\frac{\partial^2 u}{\partial x_i \partial x_j}(x) + \sum_{i=1}^{d} b_i(x)\frac{\partial u}{\partial x_i}(x) + c(x)u(x), \quad x \in \Omega \tag{2.61}$$

where $\Omega \subset \mathbb{R}^d$ is open and bounded, $u(x) \in C^2(\Omega)$ and the coefficients satisfy the following conditions

- $a_{ij}(x)$ are such that $\sum_{i,j=1}^{d} a_{ij}(x)\xi_i\xi_j \geq \mu \sum_{i=1}^{d} \xi_i^2$ for all d-dimensional vectors $\boldsymbol{\xi} = (\xi_1, \ldots, \xi_d)$, where μ is a positive constant
- $|a_{ii}(x)|, |b_i(x)| \leq C$ for some positive constant C
- $c(x) \geq 0$

Now if for some function $u(x)$ we have

$$Lu(x) \leq 0, \quad x \in \Omega \tag{2.62}$$

then the function is bounded by

$$\max_{x \in \bar{\Omega}} u \leq \max\{0, \max_{x \in \partial\Omega} u(x)\} \tag{2.63}$$

Researchers [95, 23] studied the existence of an analogous principle for the discretized operator $L^h\mathbf{u}$ defined as

$$(L^h\mathbf{u})_i = \sum_{j=1}^{N} a_{ij}u_j, \quad i = 1, \ldots, N \tag{2.64}$$

Namely, when does it follow from

$$L^h\mathbf{u} \leq 0 \tag{2.65}$$

that

$$\max_{u_i \in \bar{\Omega}^h} \mathbf{u} \leq \max\{0, \max_{u_i \in \partial\Omega^h} \mathbf{u}\} \tag{2.66}$$

i.e. that the maximum lies in a boundary node. Ciarlet [23] gives the following sufficient conditions for the existence of the discrete maximum principle

- the diagonal elements are strictly positive $a_{ii} > 0, \quad i = 1, \ldots, N$
- the off-diagonal elements are non-positive, i.e. $a_{ij} \leq 0, \quad i, j = 1, \ldots, N$
- the sum of the row sums are non-negative $\sum_{j=1}^{N} a_{ij} \geq 0, \quad i = 1, \ldots, N$
- the matrix A is irreducibly diagonally dominant

Under these conditions the discrete operator (2.64) is guaranteed to satisfy the maximum principle (2.65,2.66). Note that these are not necessary conditions and indeed Ciarlet himself shows in the same paper a matrix for a discretized operator that satisfy the maximum principle but not the above

conditions. However, we still use them as guidelines, when questioning the quality of the discretization.
Let us now consider, for illustration, an example in 1D where the elements are simply line segments. For constant coefficients, uniform mesh and linear shape functions, the contributions of the three terms for an internal node of the mesh are

$$\int_{x_{i-1}}^{x_{i+1}} a\frac{\partial u_h}{\partial x}\frac{\partial \varphi_i}{\partial x}dx = a\frac{-u_{i-1}+2u_i-u_{i+1}}{h} \tag{2.67}$$

for the diffusion

$$\int_{x_{i-1}}^{x_{i+1}} bu_h\frac{\partial \varphi_i}{\partial x}dx = b\frac{u_{i+1}-u_{i-1}}{2} \tag{2.68}$$

for the advection and

$$\int_{x_{i-1}}^{x_{i+1}} cu_h\varphi_i dx = ch\frac{u_{i-1}+4u_i+u_{i+1}}{6} \tag{2.69}$$

for the reaction terms respectively. We can see now that the discretized diffusion term satisfies the sufficient conditions. The discretized advection term, however, will add a positive off-diagonal value either above or below the main diagonal depending on the sign of b. The discretized reaction term always adds positive off-diagonal values. In order to satisfy the above conditions one can reduce the mesh size h. For the advection term one can also use an upwind scheme, which however gives only first order accurate scheme, instead of the second order provided by the central difference. For second order elements even if we only consider the diffusion term, we already have for the endpoint nodes of each element the discretization $a\frac{u_{i-2}-8u_{i-1}+14u_i-8u_{i+1}+u_{i+2}}{3h}$, i.e. even in 1D we already have positive off-diagonal elements.
In 2D and 3D, the derivatives of the shape functions, and hence the elements of the matrix, depend on the angles of the elements. There are results in 2D, for linear triangular elements, that show that if the triangulation is Delaunay [32], the diffusion term is discretized well. For rectangular elements, the mesh must be of non-narrow type,i.e. for each rectangle the ratio between its sides must be lower than $\sqrt{2}$ [38]. For parallelepiped elements in 3D, only cubes guarantee the DMP [53]. For tetrahedra, there are also criteria on the angles that the elements must satisfy [11]. However, to the best of our knowledge, there is no known automatic mesh generating method, that

consistently produces tetrahedra, that always satisfy the angle restrictions for the mesh. In that sense it is possible for some oscillations to occur in the solution, especially if subgrid scale features are present. Specifically if there are some boundary layers or internal layers, where the solution changes rapidly in neighboring elements. In such cases one can refine the mesh, to resolve the features, or apply algebraic flux corrections for the diffusion fluxes [54], like one can do for the advection for example.
Let us now consider parabolic operators like

$$(\frac{\partial u}{\partial t} + Lu)(x,t), \quad (x,t) \in \Omega \times [0,T) \tag{2.70}$$

where Lu is the elliptic operator defined in (2.61). The continuous maximum principle for this operator is then

$$\frac{\partial u}{\partial t} + Lu \leq 0 \Rightarrow \max_{\bar{\Omega}} u = \max_{\Gamma \times [0,T]} u \text{ or } \max_{\bar{\Omega}} u = \max_{\Omega} u_0 \tag{2.71}$$

where $u_0 = u(x,0)$. Similarly, the same conditions as before have to be true for the discretized operator. However, when we use linear elements and the backward Euler method, from the mass matrix the off-diagonal elements are modified with positive values. To alleviate this problem we can either reduce the mesh size until the discretized diffusion is dominating the sum (if the mesh is good in the sense that the discretized diffusion is positivity preserving), or lump the mass matrix [17]. As we already mentioned in Section 2.4 we do the latter. One has to be careful with this approach for higher order elements in two and three dimensions as the row sum of the mass matrix can become non-positive.

2.5 Newton method

Since we obtain a nonlinear system of equations we need some way to linearize it. For that we use the Newton method [29][69]. Consider the system of nonlinear algebraic equations $\mathbf{R}(\mathbf{u}) = 0$. For the vector function $\mathbf{R}(\mathbf{u})$ the Taylor series expansion around a point $\mathbf{u}_k$ is

$$\mathbf{R}(\mathbf{u}) = \mathbf{R}(\mathbf{u}_k) + \mathbf{J}(\mathbf{u}_k)(\mathbf{u} - \mathbf{u}_k) + O((\mathbf{u} - \mathbf{u}_k) \otimes (\mathbf{u} - \mathbf{u}_k))$$

where $\mathbf{J}$ is the Jacobi matrix, i.e.

$$\mathbf{J}(\mathbf{u}_k) = \frac{\partial \mathbf{R}}{\partial \mathbf{u}}(\mathbf{u}_k) \tag{2.72}$$

We drop all higher order terms (i.e. the nonlinear part) and substitute the truncated expansion in the equation $\mathbf{R}(\mathbf{u}) = 0$ to obtain

$$\mathbf{R}(\mathbf{u}_k) + \mathbf{J}(\mathbf{u}_k)(\mathbf{u} - \mathbf{u}_k) = 0$$

and solve for $\mathbf{u}$. This is summarized in the following algorithm.
Algorithm.*Newton method*

- Pick an initial iterate $\mathbf{u}_0$
- *DO*
  - Compute $\mathbf{R}(\mathbf{u}_k)$
  - Compute the Jacobi matrix of $\mathbf{R}$
  - Compute the direction $\mathbf{d}_k = -\mathbf{J}^{-1}(\mathbf{u}_k)\mathbf{R}(\mathbf{u}_k)$
  - $\mathbf{u}_{k+1} = \mathbf{u}_k + \mathbf{d}_k$

  WHILE $||\mathbf{d}_k|| > \varepsilon||\mathbf{d}_0||$

Applied to our model problem we have

$$R_i(\mathbf{u}_k) = \sum_{j=1}^{n} \frac{u_j^{n+1} - u_j^n}{\Delta t}(\varphi_j, \varphi_i) + \sum_{j=1}^{k} u_j^{n+1} a(\varphi_j, \varphi_i) + (b(\mathbf{u}_k), \varphi_i) - (f, \varphi_i) \tag{2.73}$$

$$\frac{\partial R_i}{\partial u_j^{n+1}} = \frac{(\varphi_j, \varphi_i)}{\Delta t} + a(\varphi_j, \varphi_i) + (\frac{\partial b}{\partial u}\varphi_j, \varphi_i) \tag{2.74}$$

It has quadratic convergence speed when certain conditions are met. In that sense, we make note of some important restrictions and considerations. The most obvious one is that since we need the first derivative (in this case the Jacobi matrix) it must exist and be invertible, i.e. non-singular in all the iterates $\mathbf{u}_0, \mathbf{u}_1, \ldots$. This can be problematic if for example the derivative $\mathbf{J}(\mathbf{u})$ is singular at the root of the equation $\mathbf{R}(\mathbf{u}) = 0$. Since we are solving everything numerically, even if it is analytically invertible, poor conditioning may still lead to problems in the solution. Another thing is that the quadratic convergence is guaranteed only in a ball near the solution. In general there is no guaranteed global convergence of the method. If the initial iterate is not in the necessary ball, it is possible for the method to diverge. Again as before this could also happen due to poor conditioning of the problem, since we are using computers with finite precision. The final thing that we mention here is that even in the linearized problem we still need to solve

a system of linear equations. We solve it using iterative methods. Since the problems we consider in general lead to non-symmetric matrices, the popular conjugate gradient, CG, method would not work. One can either symmetrize the matrix and then apply the CG method (which however leads to squaring of the condition number of the matrix and thus more iterations) or use a method applicable to non-symmetric systems. We use either the self implemented BiCGSTAB [94] method with ILUT [79] preconditioning or the external library SAMG [81], which is based on algebraic multigrid methods.

2.6 Directional derivatives

In some cases it is easier to derive linearized equations using the directional derivative [7]. It is defined as

$$DF[u] = \left.\frac{dF(v+\varepsilon u)}{d\varepsilon}\right|_{\varepsilon=0} \tag{2.75}$$

It can also be generalized to the Gateuax derivative over Banach spaces. It is also worth to point out that sometimes the classical Frechet derivative might not exist, while a function is still Gateuax differentiable. The reason, the directional derivative is a convenient way to develop some of the linearized equations, is that when both the Frechet and Gateuax derivatives exist, they coincide. In the case of our model problem (after discretizing in time) we have

$$R(u^{n+1}) = \frac{1}{\Delta t}(u^{n+1}-u^n, v) + a(u^{n+1}, v) + (b(u^{n+1}), v)_{\partial\Omega} - (f, v) \tag{2.76}$$

$$\begin{aligned} DR(u^{n+1})[d] &= \frac{\mathrm{d}R(u+\varepsilon d)}{\mathrm{d}\varepsilon} \\ &= \frac{\mathrm{d}}{\mathrm{d}\varepsilon}\left(\frac{1}{\Delta t}(u^{n+1}+\varepsilon d-u^n, v) + a(u^{n+1}+\varepsilon d, v) + (b(u^{n+1}+\varepsilon d), v) - (f, v)\right) \\ &= \frac{1}{\Delta t}(d, v) + a(d, v) + \left(\frac{\partial b}{\partial u}(u^{n+1})d, v\right) \end{aligned} \tag{2.77}$$

If we now do the usual finite element approximations for both u and d

$$u_h = \sum_{i=1}^{N} u_i \varphi_i \tag{2.78}$$

$$d_h = \sum_{i=1}^{N} d_i \varphi_i \tag{2.79}$$

we get

$$DR(u)[d] = \mathbf{J}(u_h)\mathbf{d} \tag{2.80}$$

and for the Newton method

$$\mathbf{Jd} = -\mathbf{R} \tag{2.81}$$

i.e. we arrived at the same formulation that we already obtained in the previous section.

2.7 Tensor algebra

We assume that the reader is already familiar with matrices and vectors and most of their properties. For completeness, however, we show certain aspects of the tensor algebra that we need for some of the considered models [7]. Of main interest to us are vectors, matrices and 4th order tensors (actually the only 4th order tensor that we use is the elasticity tensor in Chapter 4). We make use of repeated index summation (i.e. if there is a repeated index in a term, we have a sum over it) in some places for convenience, although in the chapters where it is used, it is explicitly noted. Unless otherwise specified (e.g. if they are transposed), the vectors we use are column vectors. If the dimension of the space is n, we assume that a vector $\mathbf{v}$ has n components $\{v_i\}$, $\quad i = 1, \ldots, n$, a matrix $\mathbf{A}$ has $n \times m$ components $\{a_{ij}\}$, $\quad i = 1, \ldots, n, \quad j = 1, \ldots, m$ and a fourth order tensor $\mathcal{C}$ has $n \times m \times p \times q$ components $\{C_{ijkl}\}$. We start now in no particular order to express the concepts we need.
The trace of a matrix is defined as the sum of the elements of its main diagonal, i.e.

$$\mathrm{tr}\mathbf{A} = a_{kk} \tag{2.82}$$

The product of two matrices is expressed as

$$\mathbf{C} = \mathbf{AB} \Leftrightarrow C_{ij} = A_{ik}B_{kj} \tag{2.83}$$

We define the contraction between two matrices $\mathbf{A}$ and $\mathbf{B}$ as

$$\mathbf{A} : \mathbf{B} = A_{ij}B_{ij} \tag{2.84}$$

We also have the following relation between the trace and the contraction of matrices

$$\mathbf{A} : \mathbf{B} = \mathrm{tr}(\mathbf{B}^T\mathbf{A}) = \mathrm{tr}(\mathbf{B}\mathbf{A}^T) = \mathrm{tr}(\mathbf{A}^T\mathbf{B}) = \mathrm{tr}(\mathbf{A}\mathbf{B}^T) \tag{2.85}$$

The contractions between a fourth order tensor and a second order tensor are given as

$$\mathbf{B} = \mathcal{C} : \mathbf{A} = C_{ijkl} a_{kl} \mathbf{e}_i \mathbf{e}_j^T \tag{2.86}$$

$$\mathbf{B} = \mathbf{A} : \mathcal{C} = a_{ij} C_{ijkl} \mathbf{e}_k \mathbf{e}_l^T \tag{2.87}$$

The cofactor matrix $\mathrm{Cof}(\mathbf{A})$ of a square matrix $\mathbf{A}$ is defined as

$$\mathrm{Cof}(\mathbf{A})_{ij} = (-1)^{i+j} M_{ij} \tag{2.88}$$

where M_{ij} are the minors of $\mathbf{A}$, defined as the determinant of the matrix resulting from removing the i-th row and j-th column of $\mathbf{A}$. With respect to these cofactors, the determinant can be expresses, using Laplace's formula as

$$\det(\mathbf{A}) = \sum_{j=1}^{n} (-1)^{i+j} a_{ij} M_{ij} \tag{2.89}$$

where in this case the summation is only over j and i can be any index from 1 to n. The inverse matrix $\mathbf{A}^{-1}$ is

$$\mathbf{A}^{-1} = \frac{1}{\det(\mathbf{A})} \mathrm{Cof}(\mathbf{A}) \tag{2.90}$$

We also need the invariants of $\mathbf{A}$ defined as the coefficients of the characteristic polynomial of $\mathbf{A}$

$$P(\lambda) = \det(\mathbf{A} - \lambda \mathbf{I}) \tag{2.91}$$

Specifically, the first invariant is the coefficient in front of λ^{n-1}, the second - in front of λ^{n-2} and so on until the last, which is just the free coefficient. We restrict the discussion here to a 3×3 symmetric matrices, since we are only using the invariants of such matrices. If $\mathbf{A}$ is such a matrix, its three invariants are given by

$$I_A = \mathrm{tr}(\mathbf{A}) \tag{2.92}$$

$$II_A = \mathbf{A} : \mathbf{A} \tag{2.93}$$

$$III_A = \det(\mathbf{A}) \tag{2.94}$$

Note that the second invariant should be $\frac{1}{2}(\mathrm{tr}(\mathbf{A})^2 - \mathbf{A} : \mathbf{A})$. However II_A in (2.93) is obviously also invariant and following Bonet and Wood [7] this is

the expression we use. The derivatives of the invariants with respect to the matrix $\mathbf{A}$ are

$$\left(\frac{\partial I_A}{\partial \mathbf{A}}\right)_{ij} = \frac{\partial I_A}{\partial a_{ij}} = \frac{\partial a_{kk}}{\partial a_{ij}} = \delta_{ij} \tag{2.95}$$

$$\left(\frac{\partial II_A}{\partial \mathbf{A}}\right)_{ij} = \frac{\partial a_{kl}a_{kl}}{\partial a_{ij}} = 2a_{ij} \tag{2.96}$$

$$\left(\frac{\partial III_A}{\partial \mathbf{A}}\right)_{ij} = \frac{\partial}{\partial a_{ij}}\left(\sum_{j=1}^{n}(-1)^{i+j}a_{ik}M_{ik}\right) = (-1)^{i+j}M_{ij} \tag{2.97}$$

or in matrix form

$$\frac{\partial I_A}{\partial \mathbf{A}} = \mathbf{I} \tag{2.98}$$

$$\frac{\partial II_A}{\partial \mathbf{A}} = 2\mathbf{A} \tag{2.99}$$

$$\frac{\partial III_A}{\partial \mathbf{A}} = \mathrm{Cof}(\mathbf{A}) = \det(\mathbf{A})\mathbf{A}^{-1} \tag{2.100}$$

Every symmetric real matrix can be expressed as

$$\mathbf{A} = \mathbf{P}\mathbf{\Lambda}\mathbf{P}^T \tag{2.101}$$

where $\mathbf{P}$ is an orthogonal matrix which contains the eigenvectors of $\mathbf{A}$ as columns and $\mathbf{\Lambda}$ is a diagonal matrix with the eigenvalues of $\mathbf{A}$ on its main diagonal. It is easy to see that the invariants of $\mathbf{A}$ can also be expressed as functions of the three eigenvalues as

$$I_A = \lambda_1 + \lambda_2 + \lambda_3 \tag{2.102}$$

$$II_A = \lambda_1^2 + \lambda_2^2 + \lambda_3^2 \tag{2.103}$$

$$III_A = \lambda_1\lambda_2\lambda_3 \tag{2.104}$$

Also for the powers of $\mathbf{A}$ we have

$$\mathbf{A}^n = \mathbf{P}\mathbf{\Lambda}^n\mathbf{P}^T \tag{2.105}$$

Chapter 3

Electrochemical models

The main processes that we consider are the transport of lithium-ions and electrical charge inside the battery cell. As previously mentioned in the introduction, this transport can vary depending on the type of underlying material used for the specific anode or cathode. Originally the modeling of lithium transport was initiated by Newman and his coworkers. An account of the development of these models along with more recent results is given by Newman and Alyea [67]. The type of diffusion models they considered are still widely used today and actually the two models that we use [59, 58] for the electrochemistry are also based on diffusive transport. One of the most popular models of this kind is the volume averaged 1D+1D model for spherical particles by Doyle et al. [31]. There are also other models on this semi-upscaled battery cell level based on the asymptotic homogenization theory [56],[35]. The models we consider however are on the real porous structure. Other models on this scale include [97, 57]. Numerical experiments on the model [59] are also given in [61, 72], where the researchers use the voxel based finite volume method. We compare in the results section the FEM and the voxel based FVM for the same model [59] to study the dependence on the discretization.
There are also models which deal with more complicated phenomena for the lithium transport in the solids. As we already mentioned in Chapter 1 some materials exhibit unusual loading patterns where particles charge depending on their size, or where sharp phase transitions form between lithiated and non-lithiated parts. Such phenomena are modeled by researchers with e.g. Fokker-Planck [33] or Cahn-Hilliard [86] types of equations. The Cahn-Hilliard equation is a fourth order PDE, originally used for describing separation of binary fluids. It is also extensively studied theoretically and numerically. In that sense, even though we do not use it here, our software can be easily extended to solve the Cahn-Hilliard equation, based on for-

mulations where the equations are written as a system of two second order PDEs [36].
There are many models [70, 44, 92, 74] that couple a heat transport equation to the volume averaged model by Doyle et al. [31]. There are also models which consider the temperature directly on the stack level [18, 19]. We make note here that in our simulations, the temperature increases macroscopically even though we use a cell-resolved model. This allows us to reformulate the thermal balance equation of the model [58] as an ODE for the temperature. However, we still account for the volumetric heat sources and we show that, indeed, there can be big differences in the values of the sources resulting from the geometry.
Software tools used by researchers for simulating such electrochemical models include Battery design studio [15], COMSOL [48], BEST [50], etc.
The remainder of this chapter is organized as follows. In Section 3.1 we show an isothermal electrochemical diffusion-type model [59] for transport in both the electrolyte and the electrodes. In the next section, 3.2, we also present a non-isothermal electrochemical model [58]. The heat equation from Section 3.2 is then recast in ODE form in Section 3.3. After that, we give the discretizations of the two spatially resolved models in Section 3.4. Finally, we present the results obtained by solving the two microscale models as well as the contribution of the various heat sources as obtained in the ODE from Section 3.3.

3.1 Isothermal model

The isothermal model which we use [59] is based on diffusive transport in both the electrodes and the electrolyte. It is posed on the microscale level (μm to nm scale) where we can resolve the porous structure of the electrodes, but where we do not consider kinetic models for individual atoms. In this model the unknown quantities are the lithium-ion concentration c and the electrical potential Φ. The two phases, solid active materials and liquid electrolyte, are coupled through the highly non-linear Butler-Volmer equation on the interface between them. The values of the concentration and the potential are discontinuous across the interface. The PDEs in the active material and the electrolyte are of the same form with respect to the electrical current $\mathbf{j}$ and the flux of lithium-ions $\mathbf{N}$, however the fluxes themselves are different in

the two phases. The common form of the system of PDEs is the following

$$\frac{\partial c}{\partial t} + \nabla \cdot \mathbf{N} = 0, \quad \mathbf{x} \in \Omega \tag{3.1}$$

$$\nabla \cdot \mathbf{j} = 0, \quad \mathbf{x} \in \Omega \tag{3.2}$$

where Ω is the whole computational domain. The fluxes in the electrodes are given as

$$\mathbf{N}_s = -D_s \nabla c_s, \quad \mathbf{x} \in \Omega_s \tag{3.3}$$

$$\mathbf{j}_s = -\kappa_s \nabla \Phi_s, \quad \mathbf{x} \in \Omega_s \tag{3.4}$$

and in the electrolyte they are given as

$$\mathbf{j}_e = -\kappa_e \nabla \Phi_e + \kappa_e \frac{1 - t_+}{F} \frac{RT}{c_e} \nabla c_e, \quad \mathbf{x} \in \Omega_e \tag{3.5}$$

$$\mathbf{N}_e = -D_e \nabla c_e + \frac{t_+}{F} \mathbf{j}_e, \quad \mathbf{x} \in \Omega_e \tag{3.6}$$

The subscripts s and e are used to distinguish between solid and electrolyte, respectively. In the above D is the diffusion coefficient, F is Faraday's number, R is the gas constant, t_+ is the transference number and κ is the electrical conductivity. The domains Ω_s and Ω_e refer to solid and electrolyte respectively, and we further distinguish two subdomains for Ω_s, Ω_a for anode and Ω_c for cathode. A two dimensional sketch of the domain is given in Figure 3.1

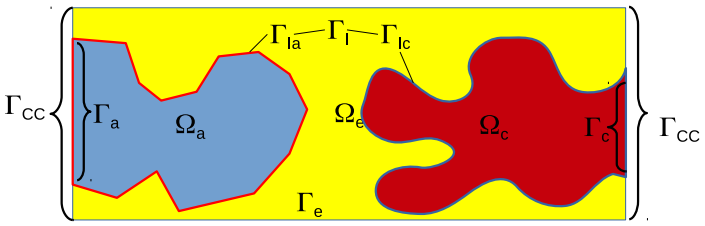

Figure 3.1: Schematic of the computational domain: Ω is the whole domain; Ω_e, Ω_a, Ω_c are the subdomains of the electrolyte, anode and cathode, respectively; Γ_e, Γ_a and Γ_c are the external boundaries of the electrolyte, the anode and the cathode; Γ_{Ia} and Γ_{Ic} are the interface boundaries of the anode the cathode and $\Gamma_I = \Gamma_{Ia} \cup \Gamma_{Ic}$ is the whole interface; Γ_{CC} is the boundary next to the current collectors, c.f. Figure 1.2

Since lithium-ions cannot leave the battery cell, we set the lithium ion flux to zero in the normal direction on the external boundaries in both phases. For the electrical current we assume that no current flows out through the external boundary of the electrolyte, i.e. we set the electrical current to zero

in the normal direction. In the electrodes we fix the potential on the boundary of the anode and prescribe a non-zero value for the electrical current in the cathode. In summary

$$\mathbf{N} \cdot \mathbf{n} = 0, \quad \mathbf{x} \in \Gamma \tag{3.7}$$
$$\mathbf{j} \cdot \mathbf{n} = 0, \quad \mathbf{x} \in \Gamma_e \tag{3.8}$$
$$\mathbf{j} \cdot \mathbf{n} = i_{appl}, \quad \mathbf{x} \in \Gamma_c \tag{3.9}$$
$$\Phi_s = a, \quad \mathbf{x} \in \Gamma_a \tag{3.10}$$

where $\Gamma = \partial\Omega$ is the external boundary of the whole geometry, $\Gamma_e = \partial\Omega \cap \partial\Omega_e$ is only the external boundary of the electrolyte (i.e. without the interface), $\Gamma_c = \partial\Omega \cap \partial\Omega_c$ and $\Gamma_a = \partial\Omega \cap \partial\Omega_a$ are the external boundaries of the cathode and the anode respectively.
On the interface between active material and electrolyte Γ_I we have

$$\mathbf{j_s} \cdot \mathbf{n_s} = \mathbf{j_e} \cdot \mathbf{n_s} = i_{se}, \quad \mathbf{x} \in \Gamma_I \tag{3.11}$$
$$\mathbf{N_s} \cdot \mathbf{n_s} = \mathbf{N_e} \cdot \mathbf{n_s} = \frac{i_{se}}{F}, \quad \mathbf{x} \in \Gamma_I \tag{3.12}$$

where $\mathbf{n}_s$ is the normal vector pointing from the active material to the electrolyte and $\Gamma_I = \Gamma_{Ia} \cup \Gamma_{Ic}$. $\Gamma_{Ia} = \partial\Omega_a \backslash \Gamma_a$ and $\Gamma_{Ic} = \partial\Omega_c \backslash \Gamma_c$ are the interfaces between the active materials and electrolyte at the anode and the cathode, respectively. The interface current density i_{se} is given by

$$i_{se} = i_0 \left(\exp(\frac{\alpha_a F}{RT}\eta_s) - \exp(-\frac{\alpha_c F}{RT}\eta_s) \right) \tag{3.13}$$

We have for the prefactor i_0

$$i_0 = k c_e^{\alpha_a} c_s^{\alpha_a} (c_{s,max} - c_s)^{\alpha_c} \tag{3.14}$$

and for the overpotential η_s

$$\eta_s = \Phi_s - \Phi_e - U_0(c_s) \tag{3.15}$$

In the above U_0 is the material specific open-circuit potential.

3.2 Non-isothermal model

The non-isothermal model [58] can be seen as an extension of the isothermal model [59]. We have a new quantity – the temperature T. The lithium and

charge transport equations are modified by the addition of a thermal gradient to the fluxes, namely

$$\mathbf{N}_s = -D_s(\nabla c_s + \frac{c_s k_{T,s}}{T}\nabla T), \quad \mathbf{x} \in \Omega_s \tag{3.16}$$

$$\mathbf{j}_s = -\kappa_s(\nabla \Phi_s + \beta_s \nabla T), \quad \mathbf{x} \in \Omega_s \tag{3.17}$$

$$\mathbf{j}_e = -\kappa_e \nabla \Phi_e + \kappa_e \frac{1-t_+}{F}\frac{RT}{c_e}\nabla c_e - \kappa_e(\beta_e - \frac{1}{F}\frac{RT}{c_e})\nabla T, \quad \mathbf{x} \in \Omega_e \tag{3.18}$$

$$\mathbf{N}_e = -D_e \nabla c_e + \frac{t_+}{F}\mathbf{j}_e - \frac{D_e c_e k_T}{T}\nabla T, \quad \mathbf{x} \in \Omega_e \tag{3.19}$$

We also have an additional PDE in each of the subdomains governing the heat transport. In the electrolyte we have

$$\begin{aligned} c_{p,e}\rho_e \frac{\partial T}{\partial t} =& \nabla(\lambda_e \nabla T) + \frac{\mathbf{j}_e^2}{\kappa_e} - T\nabla(\beta_e \mathbf{j}_e) + \\ & \frac{RT}{c_e}\frac{(\mathbf{N}_e - \frac{t_+}{F}\mathbf{j}_e)^2}{D_e} - T\nabla\left(Rk_{T,e}(\mathbf{N}_e - \frac{t_+}{F}\mathbf{j}_e)\right), \quad \mathbf{x} \in \Omega_e \end{aligned} \tag{3.20}$$

and in the solid

$$\begin{aligned} c_{p,s}\rho_s \frac{\partial T}{\partial t} =& \nabla(\lambda_s \nabla T) + \frac{\mathbf{j}_s^2}{\kappa_s} - T\nabla(\beta_s \mathbf{j}_s) - F\frac{\partial U_0}{\partial c}\frac{\mathbf{N}_s^2}{D_s} + \\ & TF\nabla\left(c_s \frac{\partial U_0}{\partial c}\frac{k_{T,s}}{T}\mathbf{N}_s\right), \quad \mathbf{x} \in \Omega_s \end{aligned} \tag{3.21}$$

The new parameters in these equations are the thermal conductivity λ, the specific heat capacity c_p, the density ρ, the Seebeck coefficient β and the Soret coefficient k_T. The model is given here in its complete form, but due to the small values of the Seeback coefficient, we neglect this term in our simulations.
On the external boundary we have a Robin type boundary condition

$$-\lambda \nabla T \cdot \mathbf{n} = \alpha(T - T_{external}), \quad \mathbf{x} \in \Gamma_{CC} \tag{3.22}$$

where Γ_{CC} is the part of the boundary, that is connected to the current collectors (the brown domains on the sides of the battery cell in Figure 1.2) and α is the heat transfer coefficient. Unlike the concentration and the potential, the temperature is continuous across the interface, i.e.

$$T_e = T_s, \quad \mathbf{x} \in \Gamma_I \tag{3.23}$$

Instead we have an interface condition on the heat fluxes

$$\begin{aligned} &-\lambda_s \nabla T \cdot \mathbf{n}_s + \lambda_e \nabla T \cdot \mathbf{n}_s = \\ &-i_{se}\eta_s - i_{se}\Pi + i_{se}\left(c_s \frac{\partial U_0}{\partial c} k_{T,s} + \frac{RTk_{T,e}(1-t_+)}{F}\right), \quad \mathbf{x} \in \Gamma_I \end{aligned} \tag{3.24}$$

leading to further sources of heat on the interface. In the above Π is the Peltier coefficient. In Table 3.1 we give a list of the heat sources. Note that we do not give all the sources present in the model, as after discretization some of them cancel out.

Table 3.1: Heat sources

Source	Electrolyte	Solid	Type
Joule heat	$\frac{\mathbf{j}_e^2}{\kappa_e}$	$\frac{\mathbf{j}_s^2}{\kappa_s}$	Irreversible
Mixing heat	$\frac{RT}{c_e}\frac{(\mathbf{N}_e - \frac{t_+}{F}\mathbf{j}_e)^2}{D_e}$	$-F\frac{\partial U_0}{\partial c}\frac{\mathbf{N}_s^2}{D_s}$	Irreversible
Soret heat	$-T\nabla\left(Rk_{T,e}(\mathbf{N}_e - \frac{t_+}{F}\mathbf{j}_e)\right)$	$TF\nabla\left(c_s\frac{\partial U_0}{\partial c}\frac{k_{T,s}}{T}\mathbf{N}_s\right)$	Reversible
Interface Joule term		$i_{se}\eta_s$	Irreversible
Interface Peltier term		$i_{se}\Pi$	Reversible

3.3 ODE form of the heat equation

In our experiments, we obtain that the temperature has very small spatial variance and practically behaves macroscopically on this scale. As such it seems unnecessary to solve a full PDE to obtain it. In this section we derive an ODE form of the heat equation from the previous section. It is a lot more efficient to solve as an ODE since we no longer have to solve a linear system on each time step. The derivation itself is similar to the one we show later in Section 3.4 for the discretized PDE, but we do not have a test function. Recall now the PDEs for the heat production in the electrolyte (3.20) and the solid (3.21). Let us integrate them over their respective domains and

sum them to obtain

$$\int_{\Omega_e} c_{p,e}\rho_e \frac{\partial T}{\partial t}\mathrm{d}v + \int_{\Omega_s} c_{p,s}\rho_s \frac{\partial T}{\partial t}\mathrm{d}v =$$
$$\int_{\Omega_e} \nabla\cdot\lambda_e\nabla T\mathrm{d}v + \int_{\Omega_s} \nabla\cdot\lambda_s\nabla T\mathrm{d}v +$$
$$\int_{\Omega_e} \frac{\mathbf{j}^2}{\kappa_e}\mathrm{d}v + \int_{\Omega_s} \frac{\mathbf{j}^2}{\kappa_s}\mathrm{d}v + \int_{\Omega_e} \frac{RT}{c_e}\frac{(\mathbf{N}-\frac{t}{F}\mathbf{j})^2}{D_e}\mathrm{d}v - \int_{\Omega_s} F\frac{\partial U_0}{\partial c}\frac{\mathbf{N}^2}{D_s}\mathrm{d}v -$$
$$\int_{\Omega_e} T\nabla\cdot(Rk_T(\mathbf{N}-\frac{t_+}{F}\mathbf{j}))\mathrm{d}v + \int_{\Omega_s} TF\nabla\cdot(c_s\frac{\partial U_0}{\partial c}\frac{k_T}{T}\mathbf{N})\mathrm{d}v \tag{3.25}$$

We use now the divergence theorem and the assumption that the temperature and its time derivative are constant in space to obtain

$$\frac{\partial T}{\partial t}\int_{\Omega} c_p\rho\mathrm{d}v =$$
$$\int_{\partial\Omega_e\cap\Gamma_{CC}} \lambda_e\nabla T\cdot\mathbf{n}\mathrm{d}s + \int_{\partial\Omega_s\cap\Gamma_{CC}} \lambda_s\nabla T\cdot\mathbf{n}\mathrm{d}s - \int_{\Gamma} \lambda_e\nabla T\cdot\mathbf{n}_s\mathrm{d}s + \int_{\Gamma} \lambda_s\nabla T\cdot\mathbf{n}_s\mathrm{d}s +$$
$$\int_{\Omega_e} \frac{\mathbf{j}^2}{\kappa_e}\mathrm{d}v + \int_{\Omega_s} \frac{\mathbf{j}^2}{\kappa_s}\mathrm{d}v + \int_{\Omega_e} \frac{RT}{c_e}\frac{(\mathbf{N}-\frac{t}{F}\mathbf{j})^2}{D_e}\mathrm{d}v - \int_{\Omega_s} F\frac{\partial U_0}{\partial c}\frac{\mathbf{N}^2}{D_s}\mathrm{d}v +$$
$$\int_{\Omega_e} T(Rk_T(\mathbf{N}-\frac{t_+}{F}\mathbf{j}))\cdot\mathbf{n}_s\mathrm{d}s + \int_{\Omega_s} F(c_s\frac{\partial U_0}{\partial c}k_T\mathbf{N})\cdot\mathbf{n}_s\mathrm{d}s \tag{3.26}$$

We apply the interface conditions (3.11),(3.12),(3.24) and the boundary condition(3.22)

$$\frac{\partial T}{\partial t}\int_{\Omega} c_p\rho\mathrm{d}v =$$
$$-\int_{\Gamma_{CC}} \alpha(T-T_{external})\mathrm{d}s + \int_{\Gamma} i_{se}\eta_s + i_{se}\Pi - i_{se}\left(c_s\frac{\partial U_0}{\partial c}k_{T,s} + RT\frac{k_{T,e}(1-t_+)}{F}\right)\mathrm{d}s +$$
$$\int_{\Omega_e} \frac{\mathbf{j}^2}{\kappa_e}\mathrm{d}v + \int_{\Omega_s} \frac{\mathbf{j}^2}{\kappa_s}\mathrm{d}v + \int_{\Omega_e} \frac{RT}{c_e}\frac{(\mathbf{N}-\frac{t}{F}\mathbf{j})^2}{D_e}\mathrm{d}v - \int_{\Omega_s} F\frac{\partial U_0}{\partial c}\frac{\mathbf{N}^2}{D_s}\mathrm{d}v +$$
$$\int_{\Gamma} \frac{RTk_T i_{se}(1-t_+)}{F}\mathrm{d}s + \int_{\Gamma} c\frac{\partial U_0}{\partial c_s}k_T i_{se}\mathrm{d}s \tag{3.27}$$

After canceling the repeating terms we get

$$\frac{\partial T}{\partial t}\int_{\Omega} c_p\rho \mathrm{d}v =$$
$$-\int_{\Gamma_{CC}} \alpha(T-T_{external})\mathrm{d}s + \int_{\Gamma} i_{se}\eta_s + i_{se}\Pi \mathrm{d}s +$$
$$\int_{\Omega_e}\frac{\mathbf{j}^2}{\kappa_e}\mathrm{d}v + \int_{\Omega_s}\frac{\mathbf{j}^2}{\kappa_s}\mathrm{d}v + \int_{\Omega_e}\frac{RT}{c_e}\frac{(\mathbf{N}-\frac{t}{F}\mathbf{j})^2}{D_e}\mathrm{d}v - \int_{\Omega_s} F\frac{\partial U_0}{\partial c}\frac{\mathbf{N}^2}{D_s}\mathrm{d}v \tag{3.28}$$

3.4 Discretization

Following the same procedure as in section 2.2 the weak form of (3.1),(3.2) is

$$\int_{\Omega}\frac{\partial c}{\partial t}\psi \mathrm{d}v - \int_{\Omega}\mathbf{N}\cdot\nabla\psi\mathrm{d}v + \int_{\Gamma_I}\mathbf{N}\cdot\mathbf{n}_s\psi\mathrm{d}s = 0 \tag{3.29}$$
$$-\int_{\Omega}\mathbf{j}\cdot\nabla\psi\mathrm{d}v + \int_{\Gamma_I}\mathbf{j}\cdot\mathbf{n}_s\psi\mathrm{d}s + \int_{\Gamma}\mathbf{j}\cdot\mathbf{n}\psi\mathrm{d}s = 0 \tag{3.30}$$

and specifically we have in the electrolyte

$$\int_{\Omega_e}\frac{\partial c}{\partial t}\psi\mathrm{d}v + \int_{\Omega_e}(D_e\nabla c_e - \frac{t_+}{F}\mathbf{j})\cdot\nabla\psi\mathrm{d}v - \int_{\Gamma_I}\frac{i_{se}}{F}\psi\mathrm{d}s = 0 \tag{3.31}$$
$$\int_{\Omega_e}(\kappa_e\nabla\Phi_e - \kappa_e\frac{1-t_+}{F}\frac{RT}{c_e}\nabla c_e)\cdot\nabla\psi\mathrm{d}v - \int_{\Gamma_I} i_{se}\psi\mathrm{d}s = 0 \tag{3.32}$$

in the anode

$$\int_{\Omega_a}\frac{\partial c}{\partial t}\psi\mathrm{d}v + \int_{\Omega_a} D_a\nabla c_s\cdot\nabla\psi\mathrm{d}v + \int_{\Gamma_{Ia}}\frac{i_{se}}{F}\psi\mathrm{d}s = 0 \tag{3.33}$$
$$\int_{\Omega_a}\kappa_a\nabla\Phi_s\cdot\nabla\psi\mathrm{d}v + \int_{\Gamma_{Ia}} i_{se}\psi\mathrm{d}s = 0 \tag{3.34}$$

and in the cathode

$$\int_{\Omega_c}\frac{\partial c}{\partial t}\psi\mathrm{d}v + \int_{\Omega_c} D_c\nabla c_s\cdot\nabla\psi\mathrm{d}v + \int_{\Gamma_{Ic}}\frac{i_{se}}{F}\psi\mathrm{d}s = 0 \tag{3.35}$$
$$\int_{\Omega_c}\kappa_c\nabla\Phi_s\cdot\nabla\psi\mathrm{d}v + \int_{\Gamma_{Ic}} i_{se}\psi\mathrm{d}v + \int_{\Gamma_c} i_{appl}\psi\mathrm{d}s = 0 \tag{3.36}$$

where we assume that $c, \Phi, \psi \in H^1(\Omega_k), k = e, a, c$. For the discretization itself we must also keep in mind that the two functions are discontinuous on the interfaces between the liquid and solid phases. Thus the basis functions have to allow for such discontinuities. One way to look at this is that the basis functions themselves are discontinuous there. This means that on the interface nodes they are unity in one phase and drop to zero in the other phase, c.f. Figure 3.2.

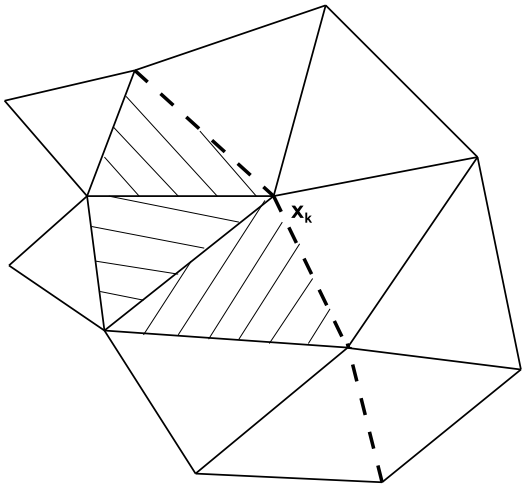

Figure 3.2: Support of interface basis function φ_k. The support of the function is restricted to the striped region. The interface is given as bold dashed line.

Their support is thus limited to a single phase. This allows us to think of the discretized quantities as being defined in the whole region as is the physical setting. On the other hand we can also consider the different phases as separate regions, with some quantities defined in the respective regions and connected to some other quantities on the interface. In both cases the discretized equations would be the same. Either way we employ node splitting on the interface, i.e. we mesh the whole geometry and then we consider each node on the interface as two distinct nodes. We do this in order to keep the two nodes geometrically in the same place. One could also define the nodes on the two sides of the interface in a way that they do not coincide geometrically and interpolate as necessary for the quadratures. This, however, introduces both increased complexity in the computations as well as potential numerical instabilities coming from the interpolation of the values. Let the discretized mesh have N nodes. Let N_I of these nodes lie on the interface. Then the total number of the nodes we consider is $N_T = N + N_I$, when we also take into account the number of nodes on the interface coming

from the node splitting. The discretized functions over the whole domain are as follows

$$C_h = \sum_{i=1}^{N_T} C_i \varphi_i(x), \quad \mathbf{x} \in \Omega \tag{3.37}$$

$$\Phi_h = \sum_{i=1}^{N_T} P_i \varphi_i(x), \quad \mathbf{x} \in \Omega \tag{3.38}$$

where C_h, Φ_h are the discretized lithium concentration and discretized potential, respectively, over Ω, $\mathbf{C} = (C_1, \ldots, C_{N_T})$ and $\mathbf{\Phi} = (P_1, \ldots, P_{N_T})$ are their nodal values and $\{\varphi_i\}_{i=1}^{N_T}$ are the basis functions of the discrete space $V_h \subset H^1(\Omega_a) \cup H^1(\Omega_c) \cup H^1(\Omega_e)$. We also further distinguish the partial sums

$$C_{h,e} = \sum_{i=1}^{N_e} C_{i,e} \varphi_i(\mathbf{x}), \quad \mathbf{x} \in \Omega_e \tag{3.39}$$

$$C_{h,s} = \sum_{i=1}^{N_s} C_{i,s} \varphi_i(\mathbf{x}), \quad \mathbf{x} \in \Omega_s \tag{3.40}$$

$$\Phi_{h,e} = \sum_{i=1}^{N_e} P_{i,e} \varphi_i(\mathbf{x}), \quad \mathbf{x} \in \Omega_e \tag{3.41}$$

$$\Phi_{h,s} = \sum_{i=1}^{N_s} P_{i,s} \varphi_i(\mathbf{x}), \quad \mathbf{x} \in \Omega_s \tag{3.42}$$

as the interpolants of the two functions in the subregion of the electrolyte Ω_e and the subregion of the solid particles Ω_s. In the same manner we also denote the vectors $\mathbf{C}_e, \mathbf{C}_s, \mathbf{\Phi}_e, \mathbf{\Phi}_s$ as containing the nodal values of the functions in the respective subregions. The number of nodes in Ω_e is N_e and in Ω_s – it is N_s. We do not show here the residual $\mathbf{R}(C_{h,e}, \Phi_{h,e}, C_{h,s}, \Phi_{h,s})$, since it is very similar in form to the weak formulation (3.29),(3.30). Namely, in order to derive $\mathbf{R}$, we substitute the discretized functions (3.37),(3.38) in the weak formulation and test the two equations with each function of the basis. This residual thus has $2N_T$ elements since we have two PDEs, discretized over N_T nodes. To apply the Newton method, we need the derivatives of this vector residual in order to assemble the Jacobi matrix. We are going to show the derivatives of the two main equations in the electrolyte and the solid with respect to the elements of $\mathbf{C}_e, \mathbf{C}_s, \mathbf{\Phi}_e, \mathbf{\Phi}_s$. Because the solutions in the regions are coupled only through the interface integrals, the derivatives of equations of one region with respect to values in the other region will

come only through these integrals. Since the weak formulations in the anode (3.33,3.34) and cathode (3.35,3.36) differ only by a linear boundary integral, that does not contribute to the derivatives, we again use the subscript s to denote either solid. We list the derivatives with respect to the nodal values of the functions. These derivatives are the elements of the Jacobi matrix. We start with the discrete lithium transport in the electrolyte

$$\begin{aligned}\frac{\partial R_i}{\partial C_{e,j}} = \frac{(\varphi_i,\varphi_j)}{\Delta t} + \left(\left(D_e - \kappa\frac{t_+(1-t_+)}{F^2}\frac{RT}{C_{h,e}}\right)\nabla\varphi_j + \right.\\ \left.\varphi_j\kappa\frac{t_+(1-t_+)}{F^2}\frac{RT}{C_{h,e}^2}\nabla C_{h,e},\nabla\varphi_i\right) - \\ \frac{1}{F}\left(k\sqrt{\frac{C_{h,s}(1-C_{h,s})}{C_{h,e}}}\sinh\left(\frac{F\eta}{2RT}\right),\varphi_i\right)\end{aligned} \tag{3.43}$$

$$\begin{aligned}\frac{\partial R_i}{\partial P_{e,j}} = \left(\frac{t_+\kappa}{F}\nabla\varphi_j,\nabla\varphi_i\right) + \\ \frac{1}{F}\left(k\sqrt{C_{h,e}C_{h,s}(1-C_{h,s})}\cosh\left(\frac{F\eta}{2RT}\right)\frac{F}{RT}\varphi_j,\varphi_i\right)\end{aligned} \tag{3.44}$$

$$\begin{aligned}\frac{\partial R_i}{\partial C_{s,j}} = -\frac{k}{F}\left(\varphi_j\sqrt{C_{h,e}}\frac{1-2C_{h,s}}{\sqrt{C_{h,s}(1-C_{h,s})}}\sinh\left(\frac{F\eta}{2RT}\right) - \right.\\ \left.\sqrt{C_{h,e}C_{h,s}(1-C_{h,s})}\cosh\left(\frac{F\eta}{2RT}\right)\frac{F}{RT}\frac{\partial U_0}{\partial c_s}\varphi_j,\varphi_i\right)\end{aligned} \tag{3.45}$$

$$\frac{\partial R_i}{\partial P_{s,j}} = -\frac{1}{F}\left(k\sqrt{C_{h,e}C_{h,s}(1-C_{h,s})}\cosh\left(\frac{F\eta}{2RT}\right)\frac{F}{RT}\varphi_j,\varphi_i\right) \tag{3.46}$$

and the charge transport also in the electrolyte

$$\frac{\partial R_i}{\partial C_{e,j}} = \left(-\kappa \frac{1-t_+}{F} \frac{RT}{C_{h,e}} \nabla \varphi_j + \varphi_j \kappa \frac{1-t_+}{F} \frac{RT}{C_{h,e}^2} \nabla C_{h,e}, \nabla \varphi_i \right) - \left(k \sqrt{\frac{C_{h,s}(1-C_{h,s})}{C_{h,e}}} \sinh \left(\frac{F\eta}{2RT} \right), \varphi_i \right) \tag{3.47}$$

$$\frac{\partial R_i}{\partial P_{e,j}} = (\kappa \nabla \varphi_j, \nabla \varphi_i) + \left(k \sqrt{C_{h,e} C_{h,s}(1-C_{h,s})} \cosh \left(\frac{F\eta}{2RT} \right) \frac{F}{RT} \varphi_j, \varphi_i \right) \tag{3.48}$$

$$\frac{\partial R_i}{\partial C_{s,j}} = - \left(\varphi_j \sqrt{C_{h,e}} \frac{1-2C_{h,s}}{\sqrt{C_{h,s}(1-C_{h,s})}} \sinh \left(\frac{F\eta}{2RT} \right) - \sqrt{C_{h,e} C_{h,s}(1-C_{h,s})} \cosh \left(\frac{F\eta}{2RT} \right) \frac{F}{RT} \frac{\partial U_0}{\partial c_s} \varphi_j, \varphi_i \right) \tag{3.49}$$

$$\frac{\partial R_i}{\partial P_{s,j}} = - \left(k \sqrt{C_{h,e} C_{h,s}(1-C_{h,s})} \cosh \left(\frac{F\eta}{2RT} \right) \frac{F}{RT} \varphi_j, \varphi_i \right) \tag{3.50}$$

In the solids we have

$$\frac{\partial R_i}{\partial C_{e,j}} = \frac{1}{F} \left(k \sqrt{\frac{C_{h,s}(1-C_{h,s})}{C_{h,e}}} \sinh \left(\frac{F\eta}{2RT} \right), \varphi_i \right) \tag{3.51}$$

$$\frac{\partial R_i}{\partial P_{e,j}} = -\frac{1}{F} \left(k \sqrt{C_{h,e} C_{h,s}(1-C_{h,s})} \cosh \left(\frac{F\eta}{2RT} \right) \frac{F}{RT} \varphi_j, \varphi_i \right) \tag{3.52}$$

$$\frac{\partial R_i}{\partial C_{s,j}} = \frac{(\varphi_i, \varphi_j)}{\Delta t} + (D_s \nabla \varphi_j, \nabla \varphi_i) + \frac{k}{F} \left(\varphi_j \sqrt{C_{h,e}} \frac{1-2C_{h,s}}{\sqrt{C_{h,s}(1-C_{h,s})}} \sinh \left(\frac{F\eta}{2RT} \right) - \sqrt{C_{h,e} C_{h,s}(1-C_{h,s})} \cosh \left(\frac{F\eta}{2RT} \right) \frac{F}{RT} \frac{\partial U_0}{\partial c_s} \varphi_j, \varphi_i \right) \tag{3.53}$$

$$\frac{\partial R_i}{\partial P_{s,j}} = \frac{1}{F} \left(k \sqrt{C_{h,e} C_{h,s}(1-C_{h,s})} \cosh \left(\frac{F\eta}{2RT} \right) \frac{F}{RT} \varphi_j, \varphi_i \right) \tag{3.54}$$

for the derivatives of the discretized lithium transport and

$$\frac{\partial R_i}{\partial C_{e,j}} = \left(k\sqrt{\frac{C_{h,s}(1-C_{h,s})}{C_{h,e}}}\sinh\left(\frac{F\eta}{2RT}\right), \varphi_i \right) \tag{3.55}$$

$$\frac{\partial R_i}{\partial P_{e,j}} = \left(k\sqrt{C_{h,e}C_{h,s}(1-C_{h,s})}\cosh\left(\frac{F\eta}{2RT}\right)\frac{F}{RT}\varphi_j, \varphi_i \right) \tag{3.56}$$

$$\begin{aligned}\frac{\partial R_i}{\partial C_{s,j}} = -k \Bigg(& \varphi_j\sqrt{C_{h,e}}\frac{1-2C_{h,s}}{\sqrt{C_{h,s}(1-C_{h,s})}}\sinh\left(\frac{F\eta}{2RT}\right) - \\ & \sqrt{C_{h,e}C_{h,s}(1-C_{h,s})}\cosh\left(\frac{F\eta}{2RT}\right)\frac{F}{RT}\frac{\partial U_0}{\partial c_s}\varphi_j, \varphi_i \Bigg)\end{aligned} \tag{3.57}$$

$$\begin{aligned}\frac{\partial R_i}{\partial P_{s,j}} = & (\kappa\nabla\varphi_j, \nabla\varphi_i) + \\ & \left(k\sqrt{C_{h,e}C_{h,s}(1-C_{h,s})}\cosh\left(\frac{F\eta}{2RT}\right)\frac{F}{RT}\varphi_j, \varphi_i \right)\end{aligned} \tag{3.58}$$

for the discretized charge transport.
On each time step we solve the coupled system of equations (3.1, 3.2) simultaneously for both the isothermal and the non-isothermal models. When we are also solving the heat transport equation, however, we use a sequential approach. We solve the electrochemical PDE system using the temperature from the previous time step and then use the electrochemical solution as input for the last PDE. Our previous work [91] showed us that in two dimensions there are practically no spatial variations in the temperature on our scale, since the heat diffusion is much faster than the heat generation. With our current experiments we found the same to be true in 3D, and thus one can neglect the temperature gradients in the first two equations and we do so here in the discretization for clarity. Also the relatively small variations of the temperature between two time steps seem to cause no discernible effect on the converged solution for the electrochemical system. Hence, we do not iterate between the electrochemical system and the temperature equation, but solve them only once per time step. The only terms in the heat equation, that we keep on the current time step are the diffusion term, so as not to impose a very strict time step restriction, and the Robin boundary condition. For the spatial discretization of the temperature we do not use the double nodes, since it is continuous even on the interfaces. The interpolant is

$$T_h = \sum_{i=1}^{N} T_i\varphi_i(\mathbf{x}), \quad x \in \Omega \tag{3.59}$$

where T_i are the nodal values of the temperature and $\{\varphi_i\}_{i=1}^N$ are defined as regular basis functions over Ω, i.e. they are not discontinuous on the interface and thus $\varphi_i \in V_h \subset H^1(\Omega)$. Due to the small values of β, we neglect the terms with the Seeback coefficient in the discretization and the solution of the heat equation. The weak formulations for the heat equation (3.20,3.21) in the two phases are

$$\begin{aligned}
&\int_{\Omega_e} c_{p,e}\rho_e \frac{\partial T}{\partial t}\psi \mathrm{d}v + \int_{\Omega_e} \lambda_e \nabla T \cdot \nabla \psi \mathrm{d}v - \int_{\partial\Omega_e} \lambda_e \nabla T \cdot \mathbf{n}_e \psi \mathrm{d}s - \\
&\int_{\Omega_e} \frac{\mathbf{j}_e^2}{\kappa_e}\psi \mathrm{d}v - \int_{\Omega_e} \frac{RT}{c_e}\frac{(\mathbf{N} - \frac{t_+}{F}\mathbf{j})^2}{D_e}\psi \mathrm{d}v - \\
&\int_{\Omega_e} \nabla(\psi T) \cdot \left(Rk_{T,e}(\mathbf{N} - \frac{t_+}{F}\mathbf{j}) \right) \mathrm{d}v + \\
&\int_{\partial\Omega_e} T \left(Rk_{T,e}(\mathbf{N} - \frac{t_+}{F}\mathbf{j}) \right) \cdot \mathbf{n}_e \psi \mathrm{d}s = 0
\end{aligned} \tag{3.60}$$

in the electrolyte and

$$\begin{aligned}
&\int_{\Omega_s} c_{p,s}\rho_s \frac{\partial T}{\partial t}\psi \mathrm{d}v + \int_{\Omega_s} \lambda_s \nabla T \cdot \nabla \psi \mathrm{d}v - \int_{\partial\Omega_s} \lambda_s \nabla T \cdot \mathbf{n}_s \psi \mathrm{d}s - \\
&\int_{\Omega_s} \frac{\mathbf{j}_s^2}{\kappa_s}\psi \mathrm{d}v + \int_{\Omega_s} F\frac{\partial U_0}{\partial c}\frac{\mathbf{N}^2}{D_s}\psi \mathrm{d}v + \\
&\int_{\Omega_s} F\nabla(\psi T) \cdot \left(c_s \frac{\partial U_0}{\partial c}\frac{k_{T,s}}{T}\mathbf{N} \right) \mathrm{d}v - \\
&\int_{\partial\Omega_s} FT \left(c_s \frac{\partial U_0}{\partial c}\frac{k_{T,s}}{T}\mathbf{N} \right) \cdot \mathbf{n}_s \psi \mathrm{d}s = 0
\end{aligned} \tag{3.61}$$

in the electrodes. To obtain the weak form over the whole domain, as well as to include the interface condition (3.24) for the heat flux over the whole

domain, we sum the two equations. The result is, after simplification

$$\int_{\Omega} c_p \rho \frac{\partial T}{\partial t} \psi \mathrm{d}v + \int_{\Omega} \lambda \nabla T \cdot \nabla \psi \mathrm{d}v -$$
$$\int_{\Omega_e} \frac{\mathbf{j}_e^2}{\kappa} \psi \mathrm{d}v - \int_{\Omega_e} \frac{RT}{c} \frac{(\mathbf{N}_e - \frac{t_+}{F}\mathbf{j}_e)^2}{D_e} \psi \mathrm{d}v -$$
$$\int_{\Omega_e} \nabla(\psi T) \cdot \left(Rk_{T,e}(\mathbf{N}_e - \frac{t_+}{F}\mathbf{j}_e) \right) \mathrm{d}v -$$
$$\int_{\Omega_s} \frac{\mathbf{j}_s^2}{\sigma} \psi \mathrm{d}v + \int_{\Omega_s} F \frac{\partial U_0}{\partial c} \frac{\mathbf{N}_s^2}{D_s} \psi \mathrm{d}v +$$
$$\int_{\Omega_s} F \nabla(\psi T) \cdot \left(c_s \frac{\partial U_0}{\partial c} \frac{k_{T,s}}{T} \mathbf{N}_s \right) \mathrm{d}v +$$
$$\int_{\Gamma_I} i_{se}(\eta_s + \Pi) \psi \mathrm{d}s + \int_{\Gamma_{CC}} \alpha(T - T_{external}) \psi \mathrm{d}s = 0 \tag{3.62}$$

After discretization in space and time we get

$$\int_{\Omega} c_p \rho \frac{T_h^{n+1} - T_h^n}{\Delta t} \varphi_i \mathrm{d}v + \int_{\Omega} \lambda \nabla T_h^{n+1} \cdot \nabla \varphi_i \mathrm{d}v -$$
$$\int_{\Omega_e} \frac{(\mathbf{j}_e^n)^2}{\kappa} \varphi_i \mathrm{d}v - \int_{\Omega_e} \frac{RT^n}{c^n} \frac{(\mathbf{N}_e^n - \frac{t_+}{F}\mathbf{j}_e^n)^2}{D_e} \varphi_i \mathrm{d}v -$$
$$\int_{\Omega_e} \nabla(\varphi_i T_h^n) \cdot \left(Rk_{T,e}(\mathbf{N}_e^n - \frac{t_+}{F}\mathbf{j}_e^n) \right) \mathrm{d}v -$$
$$\int_{\Omega_s} \frac{(\mathbf{j}_s^n)^2}{\sigma} \varphi_i \mathrm{d}v + \int_{\Omega_s} F \frac{\partial U_0}{\partial c} \frac{(\mathbf{N}_s^n)^2}{D_s} \varphi_i \mathrm{d}v +$$
$$\int_{\Omega_s} F \nabla(\varphi_i T_h^n) \cdot \left(c_s^n \frac{\partial U_0}{\partial c} \frac{k_{T,s}}{T_h^n} \mathbf{N}_s^n \right) \mathrm{d}v +$$
$$\int_{\Gamma_I} i_{se}^n(\eta_s + \Pi) \varphi_i \mathrm{d}s + \int_{\Gamma_{CC}} \alpha(T_h^{n+1} - T_{external}) \varphi_i \mathrm{d}s = 0 \tag{3.63}$$

i.e. we calculate all the heat sources with the values from the previous time step, where we denote with superscript n, the values from the previous time step and with $n+1$ – at the current time step.

Initial Newton iterate. For the Newton method we also need a good initial iterate, which is close to the solution. Otherwise the interative process might not converge. For the time dependent equations we simply use the already converged solution from the previous time step. We can also do the same for the quasi-static potential equation after the first time step. However, on the first time step for specific situations, e.g. if we apply high charge or discharge currents, it is possible for the solution to diverge. For that reason we do the following procedure to determine a good initial iterate for the potential. First, we assume that the potentials are uniform in all the media (with different values in the different phases). From our experiments this assumption seems reasonable for the electrodes. For the electrolyte, we do have spatial variations, but with the assumption for spatial uniformity we still obtain a good initial iterate. With these assumptions in mind, we have from the equations in the cathode

$$\begin{aligned} 0 &= -\nabla \cdot \sigma(\nabla \Phi_s) \\ &= -\int_{\Omega_c} \nabla \cdot (\sigma(\nabla \Phi_s)) \mathrm{d}v \\ &= -\int_{\partial\Omega_c} \sigma \nabla \Phi_s \cdot \mathbf{n} \mathrm{d}v \\ &= \int_{\Gamma_{Ic}} i_{se} \mathrm{d}s + \int_{\Gamma_c} i_{appl} \mathrm{d}s \end{aligned} \tag{3.64}$$

and hence

$$\int_{\Gamma_{Ic}} i_{se} \mathrm{d}s = -\int_{\Gamma_c} i_{appl} \mathrm{d}s \tag{3.65}$$

Using similar transformations we also obtain that in the electrolyte we have

$$\int_{\Gamma_{Ia}} i_{se} \mathrm{d}s = -\int_{\Gamma_{Ic}} i_{se} \mathrm{d}s \tag{3.66}$$

However, since we impose a Dirichlet boundary condition in the anode, and we also assumed that the potential is constant in space, we already know the value for the potential in the whole anode. Namely, it is the value of the boundary condition. Since this procedure concerns obtaining a good initial iterate for the potential before the first time step, it is not unreasonable to also consider the values of the concentration to be constant in each of the

different phases. Finally, what we obtain is

$$\int_{\Gamma_{Ia}} i_{se} \mathrm{d}s = \int_{\Gamma_c} i_{appl} \mathrm{d}s \tag{3.67}$$

We can now use the expression for i_{se} to compute the value for φ_e and then for Φ_c. Due to the assumption that all the quantities are constant

$$\int_{\Gamma_{Ia}} i_{se} \mathrm{d}s = i_{se} \int_{\Gamma_{Ia}} \mathrm{d}s \tag{3.68}$$

and therefore

$$i_{se}|_{\Gamma_{Ia}} = \frac{\int_{\Gamma_c} i_{appl} \mathrm{d}s}{\int_{\Gamma_{Ia}} \mathrm{d}s} \tag{3.69}$$

If we take (3.13) and use $\alpha_a = \alpha_c = 0.5$ we obtain

$$i_0 \sinh\left(\frac{F}{2RT}\eta_s\right) = i_{se}|_{\Gamma_{Ia}} \tag{3.70}$$

$$\eta_s = \operatorname{asinh}\left(\frac{i_{se}|_{\Gamma_{Ia}}}{i_0}\right)\frac{2RT}{F} \tag{3.71}$$

$$\Phi_a - \varphi_e - U_0 = \operatorname{asinh}\left(\frac{i_{se}|_{\Gamma_{Ia}}}{i_0}\right)\frac{2RT}{F} \tag{3.72}$$

$$\varphi_e = \Phi_a - U_0 - \operatorname{asinh}\left(\frac{i_{se}|_{\Gamma_{Ia}}}{i_0}\right)\frac{2RT}{F} \tag{3.73}$$

We can now do the same for the integrals in the other electrode to obtain Φ_c as

$$\Phi_c = \varphi_e + U_0 + \operatorname{asinh}\left(\frac{i_{se}|_{\Gamma_{Ia}}}{i_0}\right)\frac{2RT}{F} \tag{3.74}$$

3.5 Results

We are running a series of experiments using the isothermal and non-isothermal models. We test several scenarios with varying the geometry and the input parameters. Namely, we study the sensitivity of key engineering quantities on the geometry, the strength of the current applied, and the level of thermal insulation of the battery cell. We also compare the finite element solution against a voxel based finite volume method solution on the same geometry. This is done to demonstrate the advantages and disadvantages of the two approaches for the models we consider.

3.5.1 Common setup

We list the common volumetric parameters we use in Table 3.2 and the common interface ones in Table 3.3. The specific parameters and regimes for the two models are given in the respective subsections. Note that these parameters are taken to be in the realistic range of values and not necessarily measured values for a specific material. However, they are similar to the ones used in [40, 31, 61]

Table 3.2: Common parameters used for the simulations

Symbol	Name	Electrolyte	Anode	Cathode
D	Diffusion coefficient	$1.622 \times 10^{-6} \frac{\text{cm}^2}{\text{s}}$	$10^{-10} \frac{\text{cm}^2}{\text{s}}$	$10^{-10} \frac{\text{cm}^2}{\text{s}}$
t_+	Transference number	0.399	0	0
κ	Electroconductivity	$0.02 \frac{\text{S}}{\text{cm}}$	$10 \frac{\text{S}}{\text{cm}}$	$0.38 \frac{\text{S}}{\text{cm}}$
c_{max}	Maximum concentration	–	$0.023671 \frac{\text{mol}}{\text{cm}^3}$	$0.024681 \frac{\text{mol}}{\text{cm}^3}$

Table 3.3: Values of the parameters for the interface conditions

Symbol	Name	Anode	Cathode
α_a	Transfer coefficient	0.5	0.5
α_c	Transfer coefficient	0.5	0.5
k	Reaction rate constant	$0.002 \frac{\text{Acm}^{2.5}}{\text{mol}^{1.5}}$	$0.2 \frac{\text{Acm}^{2.5}}{\text{mol}^{1.5}}$

For the open-circuit potential we use the specific expressions given by Fuller et al. [40]

$$
\begin{aligned}
U_0 =& -0.132 + 1.41e^{-3.52\text{soc}}, \mathbf{x} \in \Omega_a \\
U_0 =& 4.06279 + 0.0677504 \tanh(-21.8502\text{soc} + 12.8268) - 0.045e^{-71.69\text{soc}^8} - \\
& 0.105734 \left(\frac{1}{(1.00167 - \text{soc})^{0.379571}} - 1.576 \right) + 0.01e^{-200(\text{soc}-0.19)}, \mathbf{x} \in \Omega_c
\end{aligned}
$$

where

$$soc = \frac{c}{c_{max}} \tag{3.75}$$

is the so-called state of charge. For the concentration we use the following initial conditions

$$c(\mathbf{x}, 0) = 0.1 c_{max}, \quad \mathbf{x} \in \Omega_a \tag{3.76}$$

$$c(\mathbf{x}, 0) = 0.9 c_{max}, \quad \mathbf{x} \in \Omega_c \tag{3.77}$$

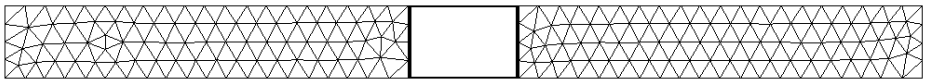

Figure 3.3: Mesh for the simple electrodes

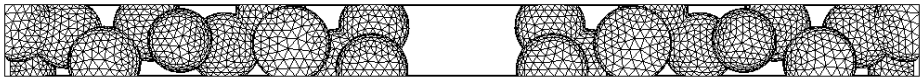

Figure 3.4: Mesh for the spherical particles

For the temperature we use

$$T(\mathbf{x}, 0) = 298K \tag{3.78}$$

where for the isothermal model, we just use this value throughout the whole simulation.

3.5.2 Isothermal model

Here we run the simulations on three different geometries:

- simple electrode geometry consisting of a single block of non-porous material for each of the electrodes, c.f. Figure 3.3; 4009 tetrahedral elements, 1198 nodes
- porous electrode geometry consisting of multiple connected spheres. Each sphere is about 10 micrometers in diameter, c.f. Figure 3.4; 56727 tetrahedral elements, 14557 nodes
- the electrodes comprise of long cylinders. The diameter of the cylinders is about 9 micrometers, c.f. Figure 3.5; 101078 tetrahedral elements, 24631 nodes

The volume of the solid of the first geometry is larger compared to the other two geometries, while the solid volumes of the second and third geometries are about the same. In all cases the electrodes are $55\mu m$ thick and the solid volumes of the spherical and cylindrical geometries are about 66% of the

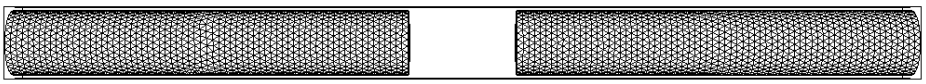

Figure 3.5: Mesh for the cylindrical particles

volume of the non-porous electrode, giving porosity of 34%. The interface surface area of the non-porous geometry is $100\mu m^2$, for the spherical geometry it is $1250\mu m^2$ and for the cylindrical geometry it is $1616\mu m^2$.The charging and discharging processes are performed on a 1C and 2C currents. Specifically 1C is the current we need to apply to charge or discharge the battery in one hour (where depending on the sign of the current we charge or discharge). This value is calculated under the assumption that the lithium diffusion is so fast in the particles, that we can consider the lithium concentration to be constant in the electrodes. The formula is thus obtained from

$$\int_{\Omega_c} \frac{\partial c}{\partial t} \mathrm{d}v = -\int_{\Omega_c} \nabla \cdot \mathbf{N} \mathrm{d}v = -\int_{\Gamma_{Ic}} \frac{i_{se}}{F} \mathrm{d}s = \frac{1}{F} \int_{\Gamma_c} i_{appl} \mathrm{d}s = \frac{i_{appl}|\Gamma_c|}{F} \tag{3.79}$$

and using the assumption that $\frac{\partial c}{\partial t}$ is constant in space, we can take it out of the volumetric integral and obtain

$$\frac{\partial c}{\partial t} = \frac{i_{appl}|\Gamma_c|}{F|\Omega_c|} \tag{3.80}$$

Integrate in t from 0 to t_{final}

$$c(t_{final}) = \frac{i_{appl}|\Gamma_c|}{F|\Omega_c|} t_{final} + c(0) \tag{3.81}$$

Substitue $c(0) = c_{max}$, $t_{final} = 3600s$, $c(3600s) = 0$ and solve for i_{appl}

$$i_{appl} = i_{1C} = -\frac{c_{max} F|\Omega_c|}{|\Gamma_c|3600s} \tag{3.82}$$

where we denoted with i_{1C} the applied current density we need for 1C rate. Note however that the assumption on the concentration being constant in space is in general false. In fact the diffusion in the particles is relatively slow, and we can obtain very uneven distributions in the concentration profile with steep gradients. Two times the C-rate or 2C is then the current which we would theoretically need to empty an electrode in half an hour. Also we calculate these values for the geometry with the spherical particles and adjust them for the other two geometries as to drive the same total current in all cases, i.e.

$$i_{spherical}|\Gamma_c|_{spherical} = i_{cylinder}|\Gamma_c|_{cylinder} = i_{brick}|\Gamma_c|_{brick} \tag{3.83}$$

We demonstrate that despite the much higher theoretical capacity of the simple electrodes, for any reasonable usage scenario the other two geometries

give a lot more usable capacity.
On Figure 3.6 we show the cell voltage U_{cell} versus transferred charge Q for a charging process. The transferred charge Q is the amount of charge we already moved from one electrode to the other. It is useful in the sense that we can compare directly different charging/discharging situations with respect to the actual capacity used. Otherwise we cannot really compare 1C to 2C for example, because it would only be natural when we apply a two times higher current, for the battery to be empty a lot quicker. The formula we use to obtain the transferred charge Q (in ampere-hours (Ah)) is

$$Q = \frac{i_{appl} \times |\Gamma_c| \times t}{3600 \frac{s}{h}} \tag{3.84}$$

where t is the time (in seconds). The cell voltage U_{cell} is the difference between the electrical potentials in the two electrodes as measured at their external boundaries, i.e.

$$U_{cell} = \Phi|_{\Gamma_c} - \Phi|_{\Gamma_a} \tag{3.85}$$

It is important because in real batteries, the manufacturers usually use the cell voltage as measure to determine when to stop charging or discharging to avoid damage to the battery. As one can see when we apply a higher current, we obtain a higher cell voltage for the same transferred charge. If the cutoff voltage (that is the voltage used internally to determine when to stop charging or discharging a battery) is for example 4.4V in the above comparison (the dotted line in the figure) we can observe that with the higher currents we would be able to use about half of the capacity compared to the lower currents. For the specific geometries we consider, we also note that for the cylindrical one we obtain slightly lower voltages for both 1C and 2C than for the spherical one. With the brick geometry even for 1C the usable capacity is negligible compared to the other two geometries. This also shows why in practice brick-like non-porous electrodes are very seldom used. In Figures 3.7 - 3.10 we can also observe the spatial profile of the lithium concentration for the spherical and cylindrical particles for both 1C and 2C cases. As can readily be observed for both geometries the higher current we apply, the steeper the gradients of the concentration of lithium ions in the electrodes. If we use smaller particles we can utilize more of the lithium ions. With smaller particles we can also obtain much higher surface areas. The higher surface area we have, the lower would be the cell voltage when we charge the battery, since we drive the same current through a bigger surface, and hence the pointwise values in i_{se} would decrease meaning a smaller potential jump. Finally in Figures 3.11 - 3.14 we show the electrical

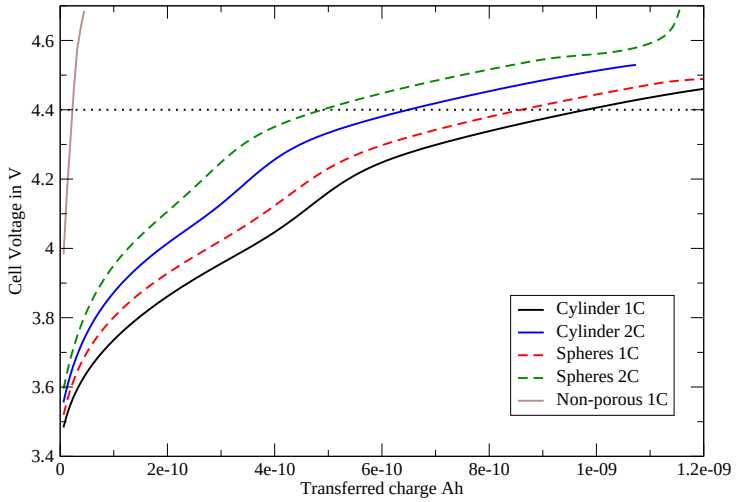

Figure 3.6: Cell voltages

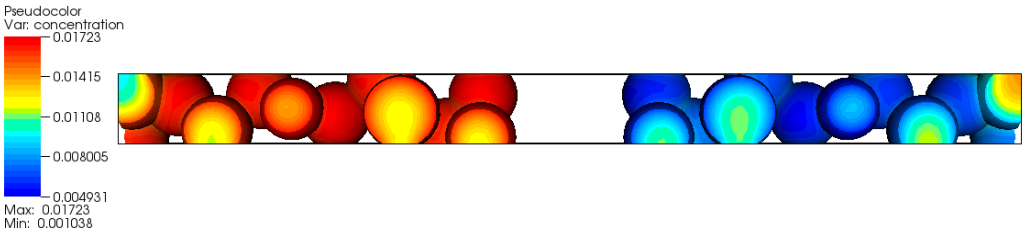

Figure 3.7: Final concentration $\left(\frac{mol}{cm^3}\right)$ profile after 1740s (Q = 1.116×10^{-9}Ah) in the charge process for 1C for spherical particles

current for the cylindrical and spherical electrodes. In 3.11 we see that where the channels in the porous spherical geometry are thin we have high electrical current. A closer view of the electrolyte near the anode is given in Figure 3.12 where this is easier to observe. Similarly in Figures 3.13 and 3.14 we give the electrical current for the geometry with the cylindrical electrodes, first for the whole electrolyte and then for the electrolyte near the anode. For this geometry there are no such localized high currents. This is important because the electrical current and the lithium flux are main ingredients in the volumetric heat sources in the non-isothermal model. We do not show the lithium flux here since its behavior is the same as the electrical current, only the values are different.

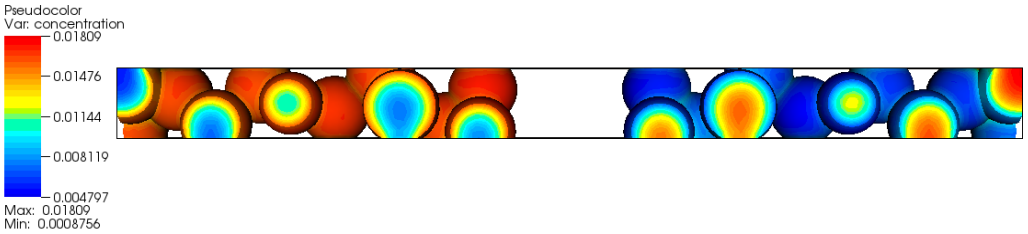

Figure 3.8: Final concentration $\left(\frac{mol}{cm^3}\right)$ profile after 690s (Q = 8.855×10^{-10}Ah) in the charge process for 2C for spherical particles

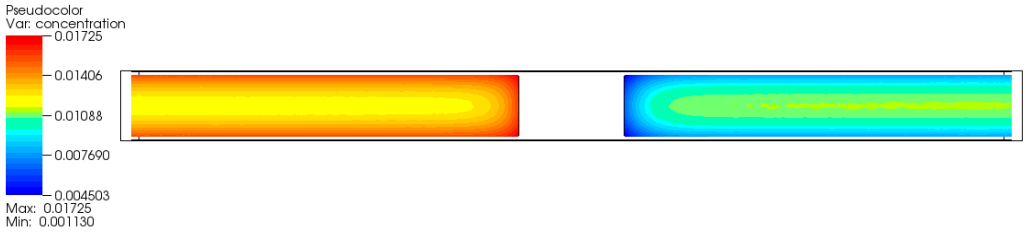

Figure 3.9: Final concentration $\left(\frac{mol}{cm^3}\right)$ profile after 1720s (Q = 1.055×10^{-9}Ah) in the charge process for 1C for cylindrical particles

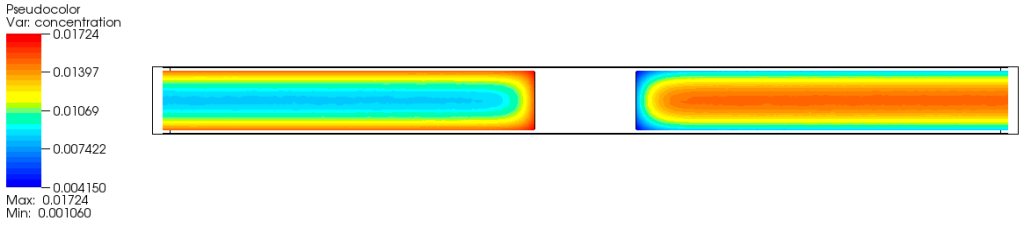

Figure 3.10: Final concentration $\left(\frac{mol}{cm^3}\right)$ profile after 700s (Q = 8.588×10^{-10}Ah) in the charge process for 2C for cylindrical particles

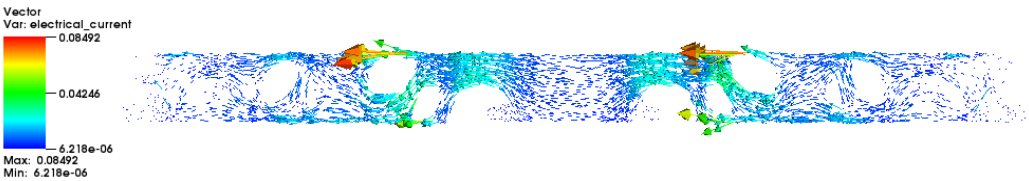

Figure 3.11: Electical current $\left(\frac{A}{cm^2}\right)$ vector field in the full electrolyte for spherical particles and 2C charging rate at 675s (Q=8.6625×10^{-10}Ah)

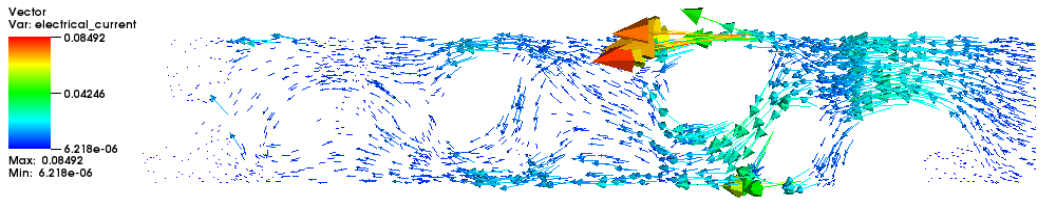

Figure 3.12: Electical current $\left(\frac{A}{cm^2}\right)$ vector field in the electrolyte near the anode for spherical particles and 2C charging rate at 675s (Q=8.6625×10^{-10}Ah)

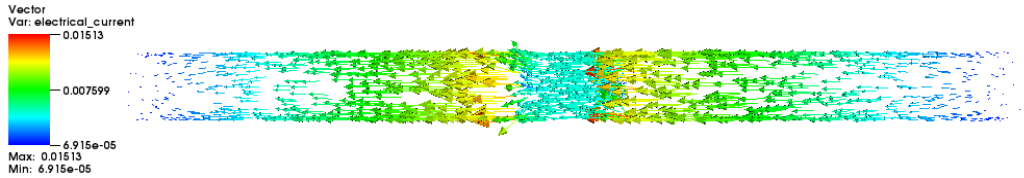

Figure 3.13: Electical current $\left(\frac{A}{cm^2}\right)$ vector field in the full electrolyte for cylindrical particles and 2C charging rate at 675s (Q=8.2815×10^{-10}Ah)

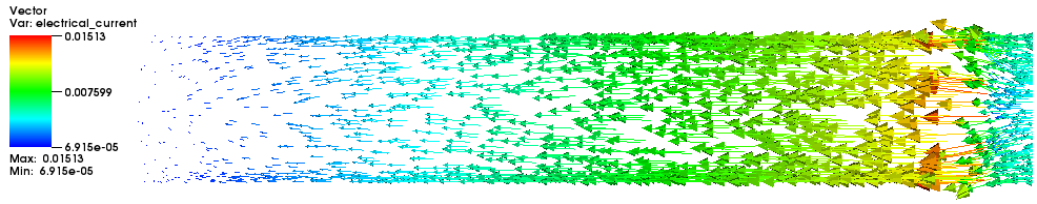

Figure 3.14: Electical current $\left(\frac{A}{cm^2}\right)$ vector field in the electrolyte near the anode for cylindrical particles and 2C charging rate at 675s (Q=8.2815×10^{-10}Ah)

3.5.3 Comparison with the finite volume method

We also perform a comparison for the isothermal electrochemical model when solved with the finite element and the voxel based cell-centered finite volume methods. For the finite volumes we use a voxel discretization coming from the software tool GeoDict [43]. For the finite element we use a tetrahedral mesh generated in Netgen [82] as well as the voxel mesh used for the FVM with hexahedral elements. The FVM simulation itself is run using the software tool BEST [50]. The FEM simulations are run, using software developed within this thesis. In the test cases we consider here, we use only one geometry consisting of four spheres for each electrode and a charging process with 1C and 10C charging rates. Note that the voxel discretization of the spheres gives a slightly larger volume for the active material than in the original geometry, which would result in a higher current being applied. This is why we computed the total applied current for the tetrahedral geometry and used it to calculate the applied current density for the voxel geometry, i.e.

$$i_{voxel} = \frac{i_{tetrahedral}|\Gamma_c|_{tetrahedral}}{|\Gamma_c|_{voxel}} \tag{3.86}$$

Also the number of elements in the tetrahedal mesh is chosen to be approximately the same as the number of volumes for the voxel mesh. The differences in the solutions are given for the cell voltages in Figure 3.15. The difference in cell voltage between FEM with tetrahedral elements and the FVM with voxel volumes for 1C is about 35-40mV. For 10C we observe a difference of about 100mV. If the operating regime of the battery is about 1V between the two cutoff voltages this is about 4% error for the 1C case and about 10% error for the 10C case. The cell voltage is a macroscopic quantity, where one would generally expect the two methods to give very close results. The differences can be explained mainly with two things - bigger interface surface area for the voxel mesh and the presence of nodes on the interfaces for the FEM. The bigger interface surface area, leads to lower resistance and hence lower values for the potential in the cathode. However, the difference between FEM with hexahedral elements and FEM with tetrahedral elements for the cell voltage is about two times smaller than the difference with FVM for both the 1C and 10C cases. This seems to imply that due to the steep gradients of the concentration close to the interface, the presence of interface nodes in the FEM also contributes to the difference in the cell voltages between the two methods. Indeed, augmenting the FVM with values on the interfaces leads to improved results in 1D cases as shown by Zhang et al. [103].
The spatial distributions of the concentration in the anode are given in Figures 3.16–3.18. When looking at the values for the concentration, we see

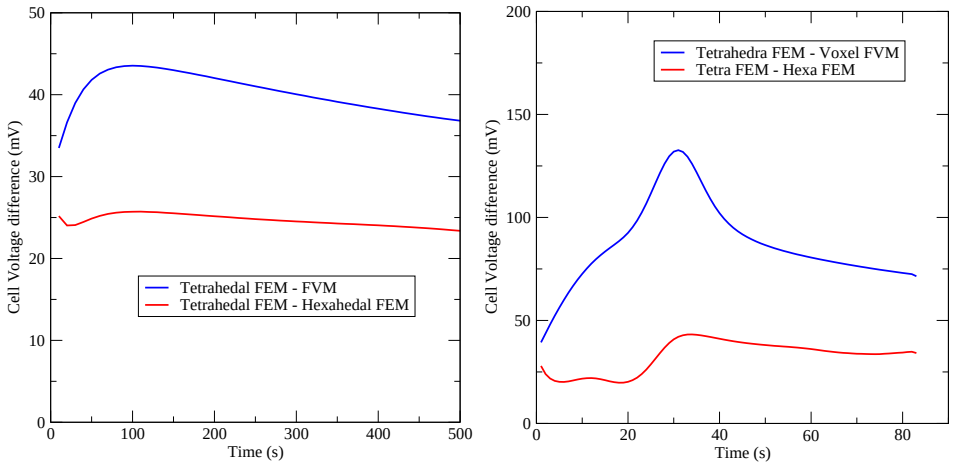

(a) 1C charging rate (b) 10C charging rate

Figure 3.15: Cell voltage differences for charging process. The red line is difference between the solutions of the FEM with tetrahedral elements and FEM with hexahedral elements, and the blue line is the difference between the solutions of the FEM with tetrahedal elements and the FVM

that the hexahedral FEM vastly overestimates the values on the interfaces where there are corners. This is true for both 1C and 10C cases. While the FVM does not seem to suffer from such overestimation, we should note that even in the 1C case (and especially in the 10C case) the distribution of the concentration on the interface is not uniform as is the case for the tetrahedral FEM. This could be important if one needs the values of the concentration as an input for computing another quantity. If one wants to simulate for example intercalation-induced stress, both the distribution of the concentration and the artificially created corners from the voxelization can be important. Similar observations about hexahedral FEM on voxel mesh versus tetrahedral FEM in the context of battery simulations coupled to linear elasticity are also reported by Hun et al. [47]. On the other hand the FVM is locally conservative, and on a Cartesian grid it is easier to build a scheme that satisfies the discrete maximum principle (Section 2.4.1), thus guaranteeing a non-oscillatory solution.

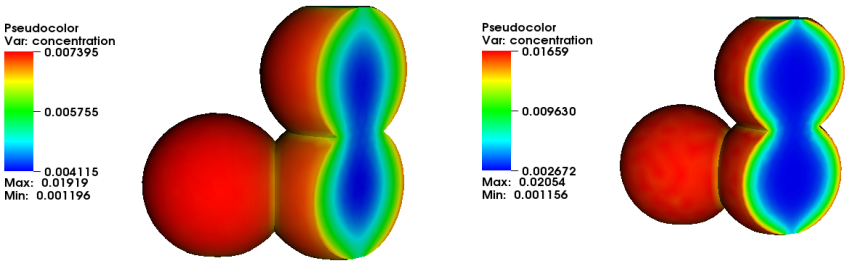

(a) 1C after 500s (b) 10C after 75s

Figure 3.16: Concentration $\left(\frac{mol}{cm^3}\right)$ profile in the anode at the end of the charging process for FEM with tetrahedal elements

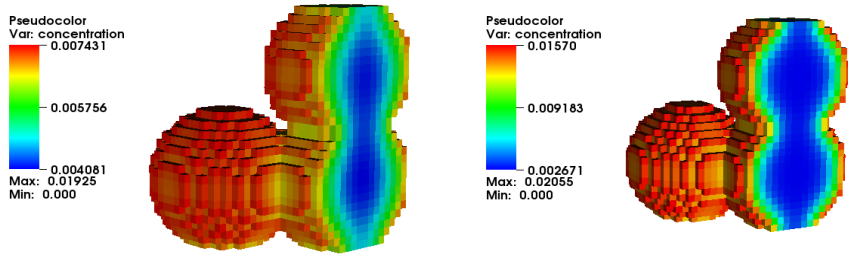

(a) 1C after 500s (b) 10C after 75s

Figure 3.17: Concentration $\left(\frac{mol}{cm^3}\right)$ profile in the anode at the end of the charging process for FVM with voxel volumes

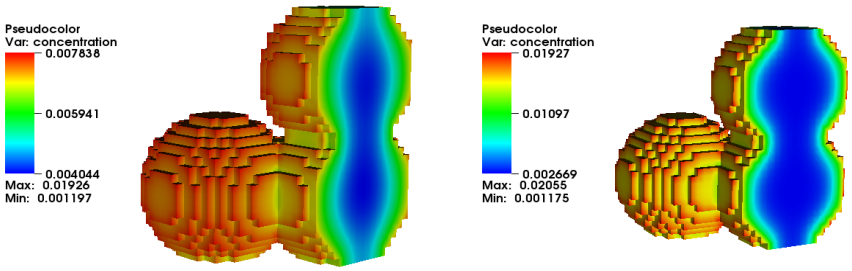

(a) 1C after 500s (b) 10C after 75s

Figure 3.18: Concentration $\left(\frac{mol}{cm^3}\right)$ profile in the anode at the end of the charging process for FEM with hexahedral elements

3.5.4 Non-isothermal model

For this model we need several parameters in addition to the ones already given in Tables 3.2 and 3.3, that we give in Table 3.4.

Table 3.4: Parameters for the thermal simulations

Symbol	Name	Electrolyte	Anode	Cathode
k_T	Soret coefficient	1	1	1
λ	Thermal conductivity	$0.01\frac{\mathrm{W}}{\mathrm{cm\cdot K}}$	$0.01\frac{\mathrm{W}}{\mathrm{cm\cdot K}}$	$0.01\frac{\mathrm{W}}{\mathrm{cm\cdot K}}$
ρ	Density	$0.001\frac{\mathrm{kg}}{\mathrm{cm}^3}$	$0.0029\frac{\mathrm{kg}}{\mathrm{cm}^3}$	$0.0036\frac{\mathrm{kg}}{\mathrm{cm}^3}$
c_p	Specific heat capacity	$2000\frac{\mathrm{J}}{\mathrm{kg\cdot K}}$	$7000\frac{\mathrm{J}}{\mathrm{kg\cdot K}}$	$7000\frac{\mathrm{J}}{\mathrm{kg\cdot K}}$
Π	Peltier coefficient	–	-0.28V	-0.38V

For the non-isothermal model we test only with the cylindrical and spherical electrodes from Section 3.5.2 and show the temperature increase for 1C and 2C and various levels of thermal insulation of the battery. Note that in our experiments the temperature behaves like a macroscopic quantity which changes on the scale of the whole cell. Therefore, we only report it as macroscopic, i.e. only a single value for the whole cell. We also show the contributions of the various heat sources in the model both on the level of the whole cell and for selected time steps also spatially to appreciate where these sources are strongest.

We first show in Figures 3.19a and 3.19b the averaged temperature under different conditions. Namely, we show for both geometries considered and for both 1C and 2C charging regimes, the temperature with respect to different levels of thermal insulation of the battery. One can observe that with increasing the C-rate the temperature increases faster for the same transferred charge for both geometries. We also observe that when we set the heat transfer coefficient α to be nonzero the temperature can almost reach a steady state by the end of the charge cycle for the 1C case, whereas this is not the case for the 2C case. Finally, we make note of the final temperatures reached in all cases, presented in Table 3.5. We observe that the temperatures for an equal transferred charge are higher in the spherical geometry for the same charge rate and insulation conditions. For the 2C case this difference is about half a degree. As we already pointed out in Section 3.5.2 the larger surface of the cylindrical electrodes leads to lower electrical potential in the cathode and to smaller absolute values of i_{se}. Since i_{se} is also the boundary condition for the concentration equation this also leads to not so sharp gradients for the concentration. For these reasons the temperature is lower in the cylindrical particles. Similar argumentation is also applicable to 1C versus 2C results where one also has a two times difference in the electrical current due to the boundary conditions and also two times higher values for i_{se}. We show in the next subsection the contributions of each heat source, but make note here why the temperature increase between 1C and 2C is not even two times, let alone more. While the heat source contributions per second increase quadratically in the case of the Joule and mixing heats

and linearly in the case of the interface contributions, the charging process ends much sooner for 2C charging rate than for 1C charging rate.

Table 3.5: Temperature reached for 10^{-9}Ah transferred charge

	Cylindrical	Spherical
1C, $\alpha = 0 \frac{W}{cm^2 K}$	304.8K	305.13K
2C, $\alpha = 0 \frac{W}{cm^2 K}$	306.34K	306.83K
1C, $\alpha = 10^{-4} \frac{W}{cm^2 K}$	300.97K	301.34K
2C, $\alpha = 10^{-4} \frac{W}{cm^2 K}$	303.32K	303.85K

Let us now focus on the individual heat sources. As one can see in Table 3.1, we have both irreversible and reversible heat sources. As we already showed in Section 3.3, under the assumption of constant in space temperature, the Soret effects in the bulk and on the interface cancel out. In that sense we only show here the spatial distributions of the Joule and mixing heats. The Joule heat and the mixing heat are functions of the squares of the fluxes and the coefficients in front of the fluxes are always positive and hence the terms are irreversible heat sources. On the interface we have two remaining terms after the discretization, namely $i_{se}\eta$ and $i_{se}\Pi$ (see Equations (3.63)). One can easily observe from the definitions of i_{se} and η that they always have the same sign and thus the first term is also always irreversible and positive. The second term, however, can change sign depending on whether we are charging or discharging, since i_{se} changes sign and it is not necessary for the Peltier coefficient Π to do so (and since we take it as a constant in our simulations it, indeed, does not). It is thus a reversible heat source, i.e. it can act as either a source or a sink depending on the process. In Figures 3.20 to 3.27 we show the pointwise values of the volumetric heat sources - Joule heat and mixing heat (given in Table 3.1). From Figures 3.20 and 3.21 we observe that for the cylindrical electrodes the values for Joule heat are higher in the electrolyte than in the electrodes. From Figures 3.24 and 3.25 we see that the same holds true also for the spherical particles. However, it is important to note that while the Joule heat does not exhibit any localization and sharp changes in the cylindrical electrodes geometry, for the spherical geometry there are some local effects where the maximum value for the Joule heat is more than an order of magnitude higher than the maximum in the cylindrical geometry. For the mixing heat in the cylinder we see from Figures 3.22 and 3.23 that the situation is reversed and the values are higher in the electrodes. Again the distributions themselves are without steep gradients. In Figures 3.26 and 3.27 we have the values of the mixing heat for the spherical geometry. While most of the values are higher in the electrodes, we see

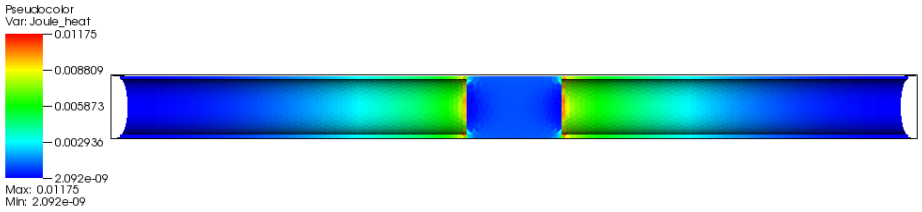

Figure 3.20: Joule heat $\left(\frac{J}{cm^3 s}\right)$ in the electrolyte in the last time step for 2C charging rate for the electrodes with cylindrical particles

that in the electrolyte there are again local effects, in the same places as before, where the maximum mixing heat values are not only higher than the values for the cylindrical geometry, but are also higher than the values in the electrodes. Finally, we present in Figure 3.28 the pointwise values of the interface term $i_{se}\Pi$ which contains the Peltier coefficient to illustrate that, indeed, it has negative values.

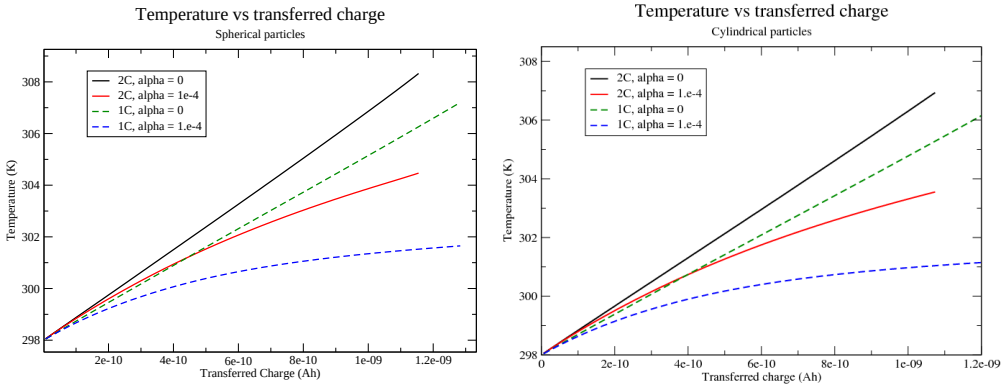

(a) Spherical particles

(b) Cylindrical particles

Figure 3.19: Temperature (K) versus transferred charge (Ah) for different values values of the heat transfer coefficient $(\frac{W}{cm^2 K})$

Heat production as an ODE

Using the ODE form of the heat equation (3.27) we obtain tempeatures which coincide up to six significant digits with the results obtained with the original

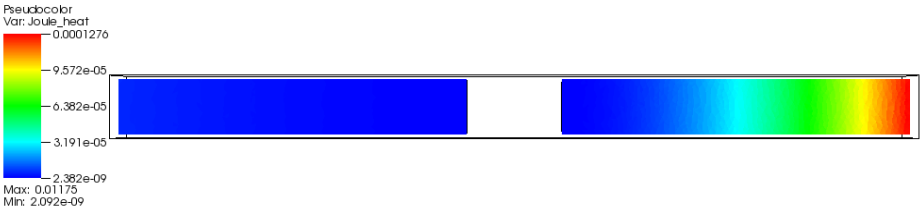

Figure 3.21: Joule heat $\left(\frac{J}{cm^3 s}\right)$ in the electrodes in the last time step for 2C charging rate for the electrodes with cylindrical particles

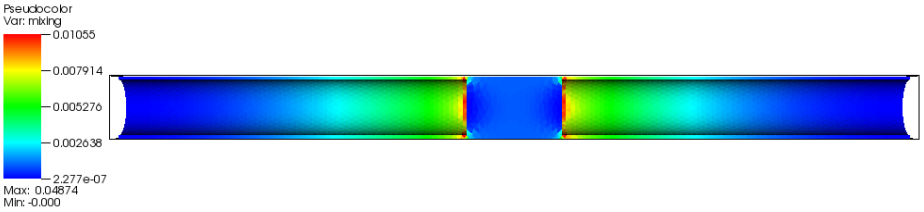

Figure 3.22: Mixing heat $\left(\frac{J}{cm^3 s}\right)$ in the electrolyte in the last time step for 2C charging rate for the electrodes with cylindrical particles

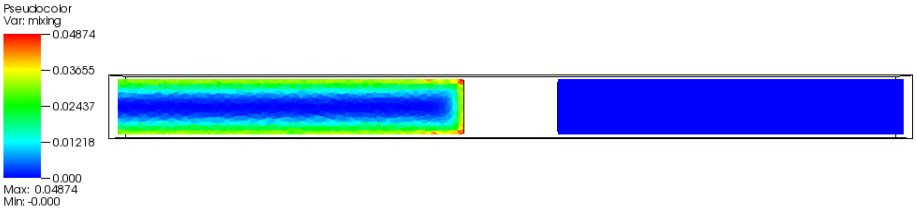

Figure 3.23: Mixing heat $\left(\frac{J}{cm^3 s}\right)$ in the electrodes in the last time step for 2C charging rate for the electrodes with cylindrical particles

Figure 3.24: Joule heat $\left(\frac{J}{cm^3 s}\right)$ in the electrolyte in the last time step for 2C charging rate for the electrodes with spherical particles

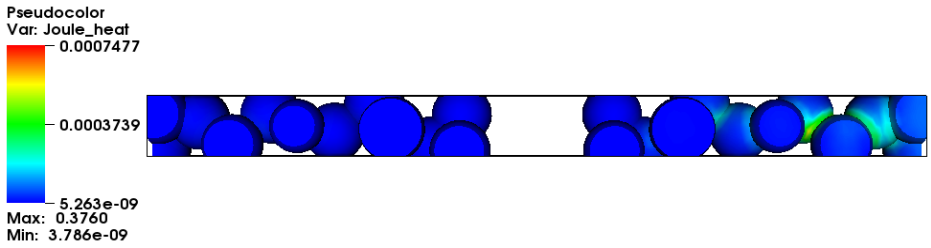

Figure 3.25: Joule heat $\left(\frac{J}{cm^3 s}\right)$ in the electrodes in the last time step for 2C charging rate for the electrodes with spherical particles

Figure 3.26: Mixing heat $\left(\frac{J}{cm^3 s}\right)$ in the electrolyte in the last time step for 2C charging rate for the electrodes with spherical particles

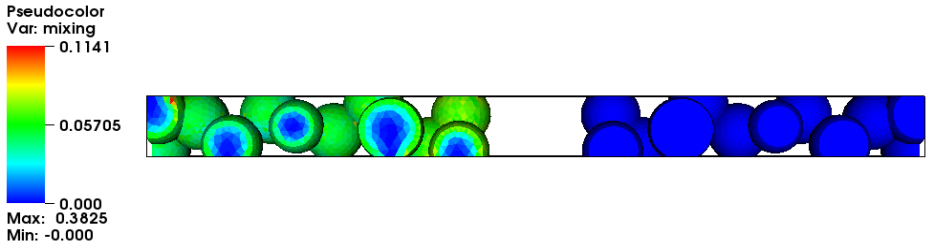

Figure 3.27: Mixing heat $\left(\frac{J}{cm^3 s}\right)$ in the electrodes in the last time step for 2C charging rate for the electrodes with spherical particles

Figure 3.28: The Peltier coefficient term $\left(\frac{J}{cm^2 s}\right)$ at the cathode interface for the cylindrical particles

PDEs (3.20),(3.21). We distinguish the heat source terms

$$P_{joule} = \int_{\Omega_e} \frac{\mathbf{j}^2}{\kappa_e} \mathrm{d}v + \int_{\Omega_s} \frac{\mathbf{j}^2}{\kappa_s} \mathrm{d}v \tag{3.87}$$

$$P_{mixing} = \int_{\Omega_e} \frac{RT}{c_e} \frac{(\mathbf{N} - \frac{t}{F}\mathbf{j})^2}{D_e} \mathrm{d}v - \int_{\Omega_s} F \frac{\partial U_0}{\partial c} \frac{\mathbf{N}^2}{D_s} \mathrm{d}v \tag{3.88}$$

$$P_{interface} = \int_{\Gamma} (i_{se}\eta_s + i_{se}\Pi) \mathrm{d}s \tag{3.89}$$

where P_{joule} is the Joule heat, P_{mixing} is the mixing heat and $P_{interface}$ is the interface heat. In time we discretize it similar to the full PDE in a sequential fashion to the other two PDEs and use the temperature from the current time step only for the outer boundary terms.

$$T^{n+1} \left(\int_{\Omega} c_p \rho \mathrm{d}v + \Delta t \int_{\partial\Omega_{out}} \alpha \mathrm{d}s \right) =$$

$$T^n \int_{\Omega} c_p \rho \mathrm{d}v + \Delta t \left(P_{joule} + P_{mixing} + P_{interface} + \int_{\partial\Omega_{out}} \alpha T_{external} \mathrm{d}s \right) \tag{3.90}$$

Let us denote the coefficient in front of T^{n+1} with

$$T_{coef} = \int_{\Omega} c_p \rho \mathrm{d}v + \Delta t \int_{\partial\Omega_{out}} \alpha \mathrm{d}s \tag{3.91}$$

We show now in several graphs and tables the contributions of the various heat sources as $\frac{P_{joule}}{T_{coef}}, \frac{P_{mixing}}{T_{coef}}, \frac{P_{interface}}{T_{coef}}$ for the Joule heating, the mixing heat and the interface heat sources respectively. As can be readily observed in Tables 3.6 to 3.9 the predominant heat generation is coming from the interface reactions. The sources on the interface are two and three orders of magnitude bigger than the mixing heat sources and the Joule heat sources, respectively. Another important observation is that when we increase the applied current density from 1C to 2C, the Joule and mixing contributions increased quadratically, i.e. four times while the interface contribution increased linearly, i.e. two times. It still is, however, the dominant heat source. Comparing Table 3.6 to Table 3.8 and Table 3.7 to 3.9 we see that, indeed, for the chosen geometries, the heat sources are more intense for the spherical geometry than for the cylindrical. In Table 3.10 we show the total contribution of each heat source at the end of the simulations.

Table 3.6: Contributions of Joule heat, mixing heat, interface heating at different times for 1C charge process on cylindrical electrodes

Time	$\frac{P_{joule}}{T_{coef}} \times 10^5$	$\frac{P_{mixing}}{T_{coef}} \times 10^5$	$\frac{P_{interface}}{T_{coef}} \times 10^3$
5s	$1.58\frac{K}{s}$	$0.826\frac{K}{s}$	$4.3\frac{K}{s}$
200s	$1.62\frac{K}{s}$	$8.79\frac{K}{s}$	$4.1\frac{K}{s}$
400s	$1.65\frac{K}{s}$	$10.7\frac{K}{s}$	$4\frac{K}{s}$
600s	$1.68\frac{K}{s}$	$11.3\frac{K}{s}$	$3.9\frac{K}{s}$
800s	$1.68\frac{K}{s}$	$11.4\frac{K}{s}$	$3.9\frac{K}{s}$

Table 3.7: Contributions of Joule heat, mixing heat, interface heating at different times for 2C charge process on cylindrical electrodes

Time	$\frac{P_{joule}}{T_{coef}} \times 10^5$	$\frac{P_{mixing}}{T_{coef}} \times 10^5$	$\frac{P_{interface}}{T_{coef}} \times 10^3$
5s	$6.35\frac{K}{s}$	$1.44\frac{K}{s}$	$10.4\frac{K}{s}$
200s	$6.63\frac{K}{s}$	$35.5\frac{K}{s}$	$9.6\frac{K}{s}$
400s	$6.55\frac{K}{s}$	$42.8\frac{K}{s}$	$9.5\frac{K}{s}$
600s	$6.60\frac{K}{s}$	$44.7\frac{K}{s}$	$9.6\frac{K}{s}$
800s	$6.64\frac{K}{s}$	$45\frac{K}{s}$	$9.8\frac{K}{s}$

Table 3.8: Contributions of Joule heat, mixing heat, interface heating at different times for 1C charge process on spherical electrodes

Time	$\frac{P_{joule}}{T_{coef}} \times 10^5$	$\frac{P_{mixing}}{T_{coef}} \times 10^5$	$\frac{P_{interface}}{T_{coef}} \times 10^3$
5s	$3.44\frac{K}{s}$	$0.906\frac{K}{s}$	$4.7\frac{K}{s}$
200s	$3.51\frac{K}{s}$	$12.7\frac{K}{s}$	$4.4\frac{K}{s}$
400s	$3.54\frac{K}{s}$	$15.6\frac{K}{s}$	$4.4\frac{K}{s}$
600s	$3.58\frac{K}{s}$	$16.6\frac{K}{s}$	$4.3\frac{K}{s}$
800s	$3.55\frac{K}{s}$	$17\frac{K}{s}$	$4.3\frac{K}{s}$

Table 3.9: Contributions of Joule heat, mixing heat, interface heating at different times for 2C charge process on spherical electrodes

Time	$\frac{P_{joule}}{T_{coef}} \times 10^5$	$\frac{P_{mixing}}{T_{coef}} \times 10^5$	$\frac{P_{interface}}{T_{coef}} \times 10^3$
5s	$13.7\frac{K}{s}$	$1.4\frac{K}{s}$	$11.2\frac{K}{s}$
200s	$14.3\frac{K}{s}$	$51.6\frac{K}{s}$	$10.5\frac{K}{s}$
400s	$14\frac{K}{s}$	$62.2\frac{K}{s}$	$10.4\frac{K}{s}$
600s	$14.1\frac{K}{s}$	$66.1\frac{K}{s}$	$10.6\frac{K}{s}$
800s	$13.9\frac{K}{s}$	$67.5\frac{K}{s}$	$10.9\frac{K}{s}$

Table 3.10: Total contributions of Joule heat, mixing heat, interface heating at the final time step

Geometry	C-rate	$\int_0^{t_{final}} \frac{P_{joule}}{T_{coef}} \mathrm{d}t$	$\int_0^{t_{final}} \frac{P_{mixing}}{T_{coef}} \mathrm{d}t$	$\int_0^{t_{final}} \frac{P_{interface}}{T_{coef}} \mathrm{d}t$
Cylindrical	1C	0.033K	0.21K	7.90K
Cylindrical	2C	0.06K	0.34K	8.40K
Spherical	1C	0.07K	0.32K	8.70K
Spherical	2C	0.13K	0.52K	9.52K

Chapter 4

Chemoelasticity

Since our primary objective is the simulation of degradation of the materials, in this chapter we consider models that take into account the generation of internal stresses in the electrodes as a result of the intercalation of lithium ions. There are two main directions that we explore. Namely, we use small strain models and large strain models. For the former we consider both a single phase model, used by Zhang et al.[105] and we also couple the mechanical model from [105] to the full isothermal electrochemical model [59], described in Chapter 3. Let us note here that solving the coupled model is implementationally challenging. Some of the equations are defined only in parts of the domain and are also solved separately. We need a convenient way to express the relation between the nodes and the degrees of freedom of the solution. To this end we developed a special class that can be used to automatically assign degrees of freedom to the nodes of the mesh. We give details in Chapter 5.
For the finite strain, our simulations are mainly in two directions. First, we want to show that a finite strain elastic model can recover some general behavior known from experimental results. Second, we do a comparison between two elastic material models to study their applicability in finite strain battery simulations. The two models are popular elastic models from the literature. To the best of our knowledge, however, there is no previous comprehensive study on the elastic model for large deformations in batteries and several different elastic models are used by different researchers [22, 106, 10].
The chapter itself is subdivided in several sections. First we start with general information about solid mechanics and mechanical stresses in Section 4.1. We give some of the measures and formulations that we need for the mechanical part of the chemoelastic simulations. We then consider the simplification to small strains and specific models on that setting in Section 4.2. The final section (4.3) is about finite strain models and simulations.

4.1 General solid mechanics

In this section we look at solid mechanics in a general setting. By that, we mean that we consider the motion of a solid body between two physically distinguishable states, that we call reference and current configurations. Here we give only a short introduction to the topic. For more detailed account see [7, 24]. Let us denote by Ω_0 the reference configuration, and by Ω the current configuration. The transformation between these configurations is given by the equation of motion

$$\mathbf{x} = \boldsymbol{\varphi}(\mathbf{X}, t), \quad \mathbf{X} \in \Omega_0 \tag{4.1}$$

Here $\mathbf{X}$ are the coordinates of the points in the original configuration, whereas $\mathbf{x}$ are the coordinates in the current configuration Ω. Alternatively we can also express (4.1) as

$$\mathbf{x} = \mathbf{X} + \mathbf{u}(\mathbf{X}, t), \quad \mathbf{X} \in \Omega_0 \tag{4.2}$$

where the vector $\mathbf{u}(\mathbf{X})$ gives us the displacement between the two states. Let us also denote by

$$\nabla_0 = \left(\frac{\partial}{\partial X_1}, \frac{\partial}{\partial X_2}, \frac{\partial}{\partial X_3} \right)^T \tag{4.3}$$

the gradient with respect to the reference coordinates and by

$$\nabla = \left(\frac{\partial}{\partial x_1}, \frac{\partial}{\partial x_2}, \frac{\partial}{\partial x_3} \right)^T \tag{4.4}$$

the gradient with respect to the current coordinates. Since in this chapter we make a frequent use of vector functions, in order to distinguish between vector indeces and derivatives we use the following notation – a subscript letter or number, without comma in front of it is an index, and if there is a comma it is a derivative. Small English letters mean differentiation with respect to the current coordinates and capital letters mean differentiation with respect to the reference configuration. Namely $u_{i,j}$ means that we differentiate the i-th component of the vector $\mathbf{u}$ with respect to x_j and $u_{i,J}$ means that we differentiate it with respect to X_J. Also if there are two repeated indeces in a term, unless otherwise specified, we sum on the repeated index, i.e. $A_{ik}B_{kj}$ means that we have a sum over the index k.

An important quantity we need is the deformation gradient

$$\mathbf{F} = \frac{\partial \mathbf{x}}{\partial \mathbf{X}} = \begin{pmatrix} \frac{\partial x_1}{\partial X_1} & \frac{\partial x_1}{\partial X_2} & \frac{\partial x_1}{\partial X_3} \\ \frac{\partial x_2}{\partial X_1} & \frac{\partial x_2}{\partial X_2} & \frac{\partial x_2}{\partial X_3} \\ \frac{\partial x_3}{\partial X_1} & \frac{\partial x_3}{\partial X_2} & \frac{\partial x_3}{\partial X_3} \end{pmatrix} = \nabla_0(\mathbf{X} + \mathbf{u}) = \mathbf{I} + \nabla_0 \mathbf{u} \tag{4.5}$$

which is the Jacobi matrix of the transformation. Observe that we have

$$d\mathbf{x} = \mathbf{F} d\mathbf{X} \tag{4.6}$$

The Jacobian of the transformation

$$J = \det(\mathbf{F}) \tag{4.7}$$

must be always positive for the transformations we consider. Also note the relation between the infinitesimal volume elements in the reference and current configurations

$$dv = JdV \tag{4.8}$$

From this relation we can also express the conservation of mass as

$$\rho_0 dV = \rho dv = \rho J dV \tag{4.9}$$

or

$$\rho_0 = \rho J \tag{4.10}$$

Important tensors derived from the deformation gradient are the right and left Cauchy-Green deformation tensors

$$\mathbf{C} = \mathbf{F}^T \mathbf{F}, \quad \mathbf{b} = \mathbf{F}\mathbf{F}^T \tag{4.11}$$

The right Cauchy-Green tensor arises naturally when we consider the length of a vector $d\mathbf{X}$ in the reference and current configurations

$$d\mathbf{x} \cdot d\mathbf{x} = (\mathbf{F} d\mathbf{X})^T (\mathbf{F} d\mathbf{X}) = d\mathbf{X}^T \mathbf{F}^T \mathbf{F} d\mathbf{X} = d\mathbf{X}^T \mathbf{C} d\mathbf{X} \tag{4.12}$$

We can use the deformation tensor $\mathbf{C}$ to define the Green strain tensor

$$\mathbf{E} = \frac{1}{2}(\mathbf{C} - \mathbf{I}) = \frac{1}{2}(\mathbf{F}^T \mathbf{F} - \mathbf{I}) \tag{4.13}$$

$$= \frac{1}{2}((\mathbf{I} + \nabla_0 \mathbf{u})^T (\mathbf{I} + \nabla_0 \mathbf{u}) - \mathbf{I}) \tag{4.14}$$

$$= \frac{1}{2}(\mathbf{I} + (\nabla_0 \mathbf{u})^T + \nabla_0 \mathbf{u} + \nabla_0 \mathbf{u}^T \nabla_0 \mathbf{u} - \mathbf{I}) \tag{4.15}$$

Compare this to (4.51) where the quadratic term is missing (and also the differentiation here is with respect to the initial configuration). From the polar factorization theorem [24] we have that we can decompose $\mathbf{F}$ into a stretch component $\mathbf{U}$ or $\mathbf{V}$ and a rotation $\mathbf{R}$

$$\mathbf{F} = \mathbf{RU} = \mathbf{VR} \tag{4.16}$$

In order to find $\mathbf{U}$ we write the eigen decomposition of $\mathbf{C}$

$$\mathbf{C} = \mathbf{Q}\boldsymbol{\Lambda}^2\mathbf{Q}^T \tag{4.17}$$
$$\boldsymbol{\Lambda}^2 = \mathrm{diag}(\lambda_i^2) \tag{4.18}$$

where the eigenvalues of $\mathbf{C}$ are the squared values of the so called principal stretches λ_i. From (4.16) it follows that

$$\mathbf{C} = \mathbf{U}^T\mathbf{R}^T\mathbf{RU} \tag{4.19}$$

However since $\mathbf{R}$ is a rotation we have that $\mathbf{R}^T\mathbf{R} = \mathbf{I}$ and hence

$$\mathbf{C} = \mathbf{U}^T\mathbf{U} \tag{4.20}$$

We pick $\mathbf{U}$ to be the square root of $\mathbf{C}$,i.e. $\mathbf{U} = \mathbf{C}^{\frac{1}{2}}$ or

$$\mathbf{U} = \mathbf{Q}\boldsymbol{\Lambda}\mathbf{Q}^T \tag{4.21}$$

We can now find $\mathbf{R}$ to be

$$\mathbf{R} = \mathbf{FU}^{-1} \tag{4.22}$$

Note that we can now also express the aforementioned Green strain as

$$\mathbf{E} = \frac{1}{2}(\mathbf{U}^2 - \mathbf{I}) = \mathbf{Q}\boldsymbol{\Lambda}_E\mathbf{Q}^T \tag{4.23}$$
$$\boldsymbol{\Lambda}_E = \frac{1}{2}\mathrm{diag}(\lambda_i^2 - 1) \tag{4.24}$$

Analogously we can decompose $\mathbf{b}$ into

$$\mathbf{b} = \mathbf{q}\boldsymbol{\Lambda}^2\mathbf{q}^T \tag{4.25}$$

and find $\mathbf{V} = \mathbf{b}^{\frac{1}{2}}$ to be

$$\mathbf{V} = \mathbf{q}\boldsymbol{\Lambda}\mathbf{q}^T \tag{4.26}$$

We define the logarithmic strain as

$$\mathbf{e}^0 = \ln \mathbf{V} = \mathbf{q}(\ln \boldsymbol{\Lambda})\mathbf{q}^T \tag{4.27}$$

Note that from Equations (4.16), (4.21) and (4.26) it follows that

$$\mathbf{RQ}\boldsymbol{\Lambda}\mathbf{Q}^T = \mathbf{q}\boldsymbol{\Lambda}\mathbf{q}^T\mathbf{R} \tag{4.28}$$

or after a multiplication from the right with $\mathbf{R}^T$

$$\mathbf{RQ}\boldsymbol{\Lambda}\mathbf{Q}^T\mathbf{R}^T = \mathbf{q}\boldsymbol{\Lambda}\mathbf{q}^T \tag{4.29}$$

Hence we have that

$$\mathbf{RQ} = \mathbf{q} \tag{4.30}$$

and consequently

$$\mathbf{F} = \mathbf{RQ}\boldsymbol{\Lambda}\mathbf{Q}^T = \mathbf{q}\boldsymbol{\Lambda}\mathbf{Q}^T \tag{4.31}$$

Now we also need an appropriate stress measure. The main one, we are interested in, is the Cauchy stress tensor $\boldsymbol{\sigma}$. Using this stress field we can uniquely determine the forces acting on a surface of the current configuration [24, 7], although this analogy is not shown here. It satisfies the following equilibrium equations

$$-\mathrm{div}\boldsymbol{\sigma}(\mathbf{x}) = \mathbf{f}(\mathbf{x}), \quad \mathbf{x} \in \Omega \tag{4.32}$$

$$\boldsymbol{\sigma}(\mathbf{x})\mathbf{n} = \mathbf{t}(\mathbf{x}), \quad \mathbf{x} \in \Gamma_t \tag{4.33}$$

In the above $\mathbf{f}(\mathbf{x})$ are the applied body forces densities, $\mathbf{t}$ are the densities of the applied surface forces on the part of the boundary of Ω, denoted by Γ_t. The Cauchy stress tensor is also symmetric

$$\boldsymbol{\sigma} = \boldsymbol{\sigma}^T \tag{4.34}$$

For the solution we also need the above equations in weak formulation where as usual we multiply by a test function $\boldsymbol{\psi}$ and integrate over the current domain Ω

$$\int_\Omega \mathrm{div}\boldsymbol{\sigma} \cdot \boldsymbol{\psi} dv = \int_\Omega \mathbf{f} \cdot \boldsymbol{\psi} dv \tag{4.35}$$

Now using the divergence theorem we obtain

$$\int_\Omega \boldsymbol{\sigma} : \nabla\boldsymbol{\psi} dv = \int_\Omega \mathbf{f} \cdot \boldsymbol{\psi} dv + \int_{\Gamma_t} \mathbf{t} \cdot \boldsymbol{\psi} da \tag{4.36}$$

We also derive several other stress measures with respect to the reference configuration. First, we have

$$\int_{\Omega} \boldsymbol{\sigma} : \nabla \boldsymbol{\psi} dv = \int_{\Omega_0} J\boldsymbol{\sigma} : \nabla \boldsymbol{\psi} dV = \int_{\Omega_0} \boldsymbol{\tau} : \nabla \boldsymbol{\psi} dV \tag{4.37}$$

where we denoted with $\boldsymbol{\tau} = J\boldsymbol{\sigma}$ the Kirchoff stress. However, the derivatives in the test function are still with respect to $\mathbf{x}$. To change them to derivatives in the reference configuration we apply the same logic that we used previously for the isoparametric finite elements. Specifically

$$\frac{\partial \psi_i}{\partial X_j} = \frac{\partial \psi_i}{\partial x_k} \frac{\partial x_k}{\partial X_j} \tag{4.38}$$

or

$$\nabla_0 \boldsymbol{\psi} = \nabla \boldsymbol{\psi} \mathbf{F} \tag{4.39}$$

and from that we obtain

$$\nabla \boldsymbol{\psi} = \nabla_0 \boldsymbol{\psi} \mathbf{F}^{-1} \tag{4.40}$$

Let us now use (4.40) in (4.37)

$$\begin{aligned} &\int_{\Omega_0} \boldsymbol{\tau} : \nabla \boldsymbol{\psi} dV = \int_{\Omega_0} \boldsymbol{\tau} : \nabla_0 \boldsymbol{\psi} \mathbf{F}^{-1} dV = \\ &\int_{\Omega_0} \mathrm{tr}(\boldsymbol{\tau} \mathbf{F}^{-T} \nabla_0 \boldsymbol{\psi}^T) dV = \int_{\Omega_0} \boldsymbol{\tau} \mathbf{F}^{-T} : \nabla_0 \boldsymbol{\psi} dV = \\ &\int_{\Omega_0} \mathbf{P} : \nabla_0 \boldsymbol{\psi} dV \end{aligned} \tag{4.41}$$

where $\mathbf{P} = J\boldsymbol{\sigma}\mathbf{F}^{-T}$ is the first Piola-Kirchoff stress tensor. Note that it is not symmetric. For this reason we use the second Piola-Kirchoff stress tensor given as

$$\mathbf{S} = J\mathbf{F}^{-1}\boldsymbol{\sigma}\mathbf{F}^{-T} = \mathbf{F}^{-1}\mathbf{P} \tag{4.42}$$

From (4.41) we have

$$\begin{aligned}\int_{\Omega_0} \mathbf{P} : \nabla_0 \boldsymbol{\psi} dV &= \int_{\Omega_0} \mathbf{F}\mathbf{F}^{-1}\mathbf{P} : \nabla_0 \boldsymbol{\psi} dV \\ &= \int_{\Omega_0} \mathbf{F}\mathbf{S} : \nabla_0 \boldsymbol{\psi} dV \\ &= \int_{\Omega_0} \mathrm{tr}(\mathbf{S}^T\mathbf{F}^T\nabla_0 \boldsymbol{\psi}) dV \\ &= \int_{\Omega_0} \mathbf{S} : \mathbf{F}^T\nabla_0 \boldsymbol{\psi} dV \end{aligned} \tag{4.43}$$

In order to pose the problem entirely in the reference domain we also need to pull back the integrals containing the body and surface forces. We already have the connection between the infinitesimal volume elements and for the surface elements we have [7]

$$\frac{\mathrm{d}a}{\mathrm{d}A} = J\sqrt{\mathbf{N}^T\mathbf{C}^{-1}\mathbf{N}} \tag{4.44}$$

Then for the body forces we have

$$\int_{\Omega} \mathbf{f} \cdot \boldsymbol{\psi} dv = \int_{\Omega_0} J\mathbf{f} \cdot \boldsymbol{\psi} dV = \int_{\Omega_0} \mathbf{f}_0 \cdot \boldsymbol{\psi} dV \tag{4.45}$$

and for the surface forces

$$\int_{\partial\Omega} \mathbf{t} \cdot \boldsymbol{\psi} da = \int_{\partial\Omega_0} \mathbf{t}\frac{da}{dA} \cdot \boldsymbol{\psi} dA = \int_{\partial\Omega_0} \mathbf{t}_0 \cdot \boldsymbol{\psi} dA \tag{4.46}$$

Finally the weak formulation in the reference configuration is

$$\int_{\Omega_0} \mathbf{S} : \mathbf{F}^T\nabla_0 \boldsymbol{\psi} dV = \int_{\Omega_0} \mathbf{f}_0 \cdot \boldsymbol{\psi} dV + \int_{\partial\Omega_0} \mathbf{t}_0 \cdot \boldsymbol{\psi} dA \tag{4.47}$$

The last thing we want to define here are the so called Von Mises stress and Von Mises strain given as

$$\sigma_{VM} = \sqrt{\frac{3}{2}\sigma_{ij}\sigma_{ij} - \frac{1}{2}(\sigma_{kk})^2} \tag{4.48}$$

$$\epsilon_{VM} = \sqrt{\frac{2}{3}\epsilon^d_{ij}\epsilon^d_{ij}}, \quad \epsilon^d_{ij} = \epsilon_{ij} - \frac{1}{3}\delta_{ij}\epsilon_{kk} \tag{4.49}$$

where σ is the Cauchy stress and ϵ is the strain tensor. These quantities are useful scalar measures on the stresses and strains, often used to determine the onset of inelastic deformations.

4.2 Small strain

The small strain study of diffusion induced stress was originally proposed by Prussin for thin plates [73], based on an analogy with thermoelasticity. Later this model was also put in the terms of three-dimensional formulation, see e.g. Yang [101]. The three-dimensional model was introduced in the context of lithium-ion batteries, for electrodes that undergo relatively small deformation during lithiation, by Zhang et al. [105], although a similar model was also used earlier by García et al. [41]. Furthermore Zhang et al. [104] also couple this model to heat generation.
DeLuca et al. [28] study stress generation in Si using a small strain model with concentration dependent elastic moduli, surface stresses and Butler-Volmer condition for the boundary of the diffusion equation, but assume fixed values for the lithium concentration and the electrical potential in the electrolyte. Ryu et al. [78] use the small strain model for Silicon particles, and they couple it to fracture to study the dependence of fracture on particle size. They derive a concentration dependent volume expansion coefficient that we also adopt in our simulations. Kalnaus et al. [52] couple the model [105] to damage and fracture models to study Si particles. Other researchers also couple it to plasticity and fracture [108, 107, 65].
In the current work, we use the model [105] to predict the small strain mechanical behavior. It is described in Section 4.2.1. In the same section we also describe how we couple this model to the full electrochemical model [59]. In Section 4.2.2 we show the discretized equations. Finally, in Section 4.2.3 we show the numerical experiments that we perform. We first test the model [105] for two different scenarios for a cylindrical particle, to study the influence of the advective term on the concentration. We then compare the results obtained when using the model [105] as is and when we couple it to [59] as described in Section 4.2.1.

4.2.1 Model

Let us now briefly describe the model [105]. In small strain theory we assume that the deformation is sufficiently small that we can consider the initial and the final configurations to coincide. This means it is only necessary to consider the Cauchy stress measure and we can also neglect the nonlinear term $\nabla \mathbf{u} \nabla \mathbf{u}^T$ from the Cauchy-Green strain tensor to arrive at the so called engineering strain measure. The engineering strain is given by

$$\varepsilon_{ij} = \frac{1}{2} \left(u_{i,j} + u_{j,i} \right) \tag{4.50}$$

or in vector form

$$\boldsymbol{\varepsilon} = \frac{1}{2}\left(\nabla \mathbf{u} + \nabla \mathbf{u}^T\right) \tag{4.51}$$

The assumption is then that we can decompose additively this strain in an elastic strain and chemical strain

$$\boldsymbol{\varepsilon} = \boldsymbol{\varepsilon}_e + \boldsymbol{\varepsilon}_c \tag{4.52}$$

We also assume that the volumetric expansion due to the intercalating lithium is linear with a coefficient Ω called partial molar volume [1]. Let us further assume that the chemical expansion is isotropic along the main axes. We can then obtain a linear coefficient of expansion along a single axis, the same way as in thermoelasticity, i.e.

$$\alpha \approx \frac{\Omega}{3} \tag{4.53}$$

and hence

$$\varepsilon_{c,ij} = \alpha c \delta_{ij} \tag{4.54}$$

where c is the lithium concentration. From Hooke's law we have then

$$\begin{aligned}
\boldsymbol{\sigma} =& 2\mu\boldsymbol{\varepsilon}_e + \lambda \mathrm{tr}(\boldsymbol{\varepsilon}_e)\mathbf{I} = && (4.55)\\
& 2\mu(\boldsymbol{\varepsilon} - \boldsymbol{\varepsilon}_c) + \lambda \mathrm{tr}(\boldsymbol{\varepsilon} - \boldsymbol{\varepsilon}_c)\mathbf{I} = && (4.56)\\
& 2\mu(0.5(\nabla \mathbf{u} + \nabla \mathbf{u}^T) - \alpha c\mathbf{I}) + \lambda \mathrm{tr}(0.5(\nabla \mathbf{u} + \nabla \mathbf{u}^T) - \alpha c\mathbf{I})\mathbf{I} = && (4.57)\\
& 2\mu(0.5(\nabla \mathbf{u} + \nabla \mathbf{u}^T)) + \lambda \mathrm{tr}(0.5(\nabla \mathbf{u} + \nabla \mathbf{u}^T))\mathbf{I} - \Omega c \frac{2\mu + 3\lambda}{3}\mathbf{I} = && (4.58)\\
& 2\mu\boldsymbol{\varepsilon} + \lambda \mathrm{tr}(\boldsymbol{\varepsilon})\mathbf{I} - \beta c\mathbf{I} && (4.59)
\end{aligned}$$

where we have denoted with $\beta = \kappa\Omega$ and $\kappa = \frac{2\mu+3\lambda}{3}$ is the so called bulk modulus. Also $\boldsymbol{\sigma}$ is the Cauchy stress tensor and λ and μ are the Lame parameters. Usually in experiments we have data for Young's modulus E and the Poisson ratio ν. The Lame parameters can be determined from E and μ using the relations

$$\mu = \frac{E}{2(1+\nu)} \tag{4.60}$$

$$\lambda = \frac{E\nu}{(1+\nu)(1-2\nu)} \tag{4.61}$$

Finally for the ionic flux Zhang et al.[105] give the following expression

$$\mathbf{J} = -D\left(\nabla c - \frac{\Omega c}{RT}\nabla\sigma_h\right) \tag{4.62}$$

The resulting model is given by

$$c_{,t} - \nabla \cdot D\left(\nabla c - \frac{\Omega c}{RT}\nabla\sigma_h\right) = 0 \tag{4.63}$$

$$-D\left(\nabla c - \frac{\Omega c}{RT}\nabla\sigma_h\right)\cdot\mathbf{n} = g \tag{4.64}$$

for the diffusion of lithium ions and

$$\varepsilon_{ij} = \frac{1}{2}\left(u_{i,j} + u_{j,i}\right) \tag{4.65}$$

$$\sigma_{ij} = 2\mu\varepsilon_{ij} + (\lambda\varepsilon_{kk} - \beta c)\delta_{ij} \tag{4.66}$$

$$\sigma_{ij,i} = 0 \tag{4.67}$$

$$\sigma\cdot\mathbf{n} = \mathbf{t} \tag{4.68}$$

$$\sigma_h = (\sigma_{11} + \sigma_{22} + \sigma_{33})/3 \tag{4.69}$$

for the mechanical stress. The latter equations can also be given in vector notation, rather than index notation as

$$\boldsymbol{\varepsilon} = \frac{1}{2}(\nabla\mathbf{u} + \nabla\mathbf{u}^T) \tag{4.70}$$

$$\boldsymbol{\sigma} = 2\mu\boldsymbol{\varepsilon} + (\lambda tr(\boldsymbol{\varepsilon}) - \beta c)\mathbf{I} \tag{4.71}$$

$$\nabla\cdot\boldsymbol{\sigma} = 0 \tag{4.72}$$

$$\boldsymbol{\sigma}\cdot\mathbf{n} = \mathbf{t} \tag{4.73}$$

$$\sigma_h = \frac{1}{3}tr(\boldsymbol{\sigma}) \tag{4.74}$$

Note that this model considers only the lithium diffusion in the relevant electrode and the Butler-Volmer interface condition is replaced by a fixed Neumann boundary condition. Later we extend the model from [105] by coupling the equilibrium equation (4.67) (along with its boundary conditions) to the full isothermal electrochemical model [59] from Section 3.1. We do this by using (4.62) in Equation (3.1) as the expression for the lithium flux in the electrodes. We can observe in (4.63) that the diffusion transport is modified by an additional pressure term. Ryu et al. [78] also consider the use of the Butler-Volmer equation on the boundary of the electrode and a potential equation in the electrode, but use fixed values for the concentration and potential for the electrolyte. Bower et al. [10], also propose a full

electrochemical model for a battery half-cell (i.e. they use Li-metal for the cathode) coupled to a finite strain model for the deformation and relate the electric charge and the stress. In our case, we do not include such relations.

4.2.2 Discretization

For the weak form of the momentum equation let us recall (4.36)

$$\int_\Omega \boldsymbol{\sigma} : \nabla \boldsymbol{\psi} dv - \int_{\partial\Omega} \mathbf{t} \cdot \boldsymbol{\psi} da = 0 \tag{4.75}$$

where we note that the volumetric body force integral is omitted since in this model we do not have explicit body forces. Let us also present the above equation in displacement formulation. We have for the first term

$$\begin{aligned} \int_\Omega \boldsymbol{\sigma} : \nabla \boldsymbol{\psi} dv &= \int_\Omega \sigma_{ij} \psi_{i,j} dv \\ &= \int_\Omega [2\mu\varepsilon_{ij} + (\lambda\varepsilon_{kk} - \beta c)\delta_{ij}]\psi_{i,j} dv \\ &= \int_\Omega [\mu(u_{i,j} + u_{j,i}) + (\lambda u_{k,k} - \beta c)\delta_{ij}]\psi_{i,j} dv \end{aligned} \tag{4.76}$$

When we plug (4.76) back into (4.75) we get

$$\int_\Omega [\mu(u_{i,j} + u_{j,i}) + (\lambda u_{k,k} - \beta c)\delta_{ij}]\psi_{i,j} dv - \int_{\partial\Omega} t_i \psi_i da = 0 \tag{4.77}$$

For the concentration equation (4.63) we have

$$\int_\Omega c_{,t}\psi + D\left(\nabla c - \frac{\Omega c}{RT}\nabla\sigma_h\right) \cdot \nabla\psi dv + \int_{\partial\Omega} g\psi da = 0 \tag{4.78}$$

Similar to how we solve the thermal electrochemical model, we solve the diffusion equation and the equilibrium equation sequentially and not simultaneously. We use the following discretizations of the main quantities

$$\mathbf{u}_h = \sum_{b=1}^{N} \varphi_b \mathbf{u}_b = \sum_{b=1}^{N} \varphi_b \begin{pmatrix} u_{b1} \\ u_{b2} \\ u_{b3} \end{pmatrix} \tag{4.79}$$

for the displacement field, where u_{bi} is the i-th coordinate of the b-th unknown nodal displacement value. We also have

$$c_h = \sum_{b=1}^{N} \varphi_b c_b \tag{4.80}$$

for the concentration. The three components of the displacement and the concentration are discretized using the same basis functions. We use this basis for both the trial and for the test functions. The vector test function $\boldsymbol{\psi}$ is picked as

$$\boldsymbol{\psi} = \varphi_b \mathbf{e}_i, \quad i = 1, 2, 3 \tag{4.81}$$

i.e. at any given time only one of its components is non-zero and the non-zero component is one of the basis functions. Note that this is equivalent to testing each of the three scalar equations of the momentum equation separately.
Let us now discuss the discretized form of the equilibrium equation. We substitute c_h and $\mathbf{u}_h$ in (4.77) to obtain

$$\int_\Omega [\mu(u_{bi}\varphi_{b,j} + u_{bj}\varphi_{b,i}) + (\lambda u_{bk}\varphi_{b,k} - \beta c_h)\delta_{ij}]\varphi_{a,j} dv - \int_{\partial\Omega} p n_i \varphi_a da = 0, \quad a = 1, \ldots, N \quad i = 1, 2, 3 \tag{4.82}$$

We solve the diffusion and equilibrium equations consequently, and so we take the concentration part of the stress in Equation (4.82) as a right hand side

$$\int_\Omega [\mu(u_{bi}\varphi_{b,j} + u_{bj}\varphi_{b,i}) + \lambda u_{bk}\varphi_{b,k}\delta_{ij}]\varphi_{a,j} dv = \int_\Omega \beta c_h \varphi_{a,i} dv + \int_{\partial\Omega} p n_i \varphi_a da, \quad a = 1, \ldots, N \quad i = 1, 2, 3 \tag{4.83}$$

Let us now determine the elements of the stiffness matrix. Since we are discretizing a system of three PDEs, for the three components of the displacement, for each interaction between the basis functions φ_a and φ_b, correspond a 3×3 matrix. Let us denote by

$$\mathbf{U} = \begin{pmatrix} \mathbf{u}_1 \\ \vdots \\ \mathbf{u}_N \end{pmatrix} = \begin{pmatrix} u_{11} \\ u_{12} \\ u_{13} \\ \vdots \end{pmatrix} \tag{4.84}$$

the vector of the unknown nodal displacements, with

$$\mathbf{F} = \begin{pmatrix} \mathbf{f}_1 \\ \vdots \\ \mathbf{f}_N \end{pmatrix}, \quad \mathbf{f}_a = \begin{pmatrix} \int_\Omega \beta c_h \varphi_{a,1} dv + \int_{\partial\Omega} p n_1 \varphi_a da \\ \int_\Omega \beta c_h \varphi_{a,2} dv + \int_{\partial\Omega} p n_2 \varphi_a da \\ \int_\Omega \beta c_h \varphi_{a,3} dv + \int_{\partial\Omega} p n_3 \varphi_a da \end{pmatrix} \tag{4.85}$$

the discretized right hand side and with

$$\mathbf{K} = \begin{pmatrix} \mathbf{K}_{11} & \dots & \mathbf{K}_{1N} \\ \vdots & \ddots & \vdots \\ \mathbf{K}_{N1} & \dots & \mathbf{K}_{NN} \end{pmatrix} \tag{4.86}$$

the stiffness matrix, where $\mathbf{K}_{ab}$ are 3×3 matrices as previously noted. We can thus write the discretized system as

$$\mathbf{KU} = \mathbf{F} \tag{4.87}$$

The final thing we need are the elements of the stiffness matrix, i.e. $K_{ab,ij}$, where in this case the comma stands to distinguish the indeces of the $\mathbf{K}_{ab}$ matrices and not for differentiation. Let us consider the term on the left hand side in (4.83)

$$\int_\Omega [\mu(u_{bi}\varphi_{b,j} + u_{bj}\varphi_{b,i}) + \lambda u_{bk}\varphi_{b,k}\delta_{ij}]\varphi_{a,j} dv =$$

$$\int_\Omega [\mu(u_{bi}\varphi_{b,j}\varphi_{a,j} + u_{bj}\varphi_{b,i}\varphi_{a,j}) + \lambda u_{bj}\varphi_{b,j}\varphi_{a,i}] dv = \tag{4.88}$$

$$\int_\Omega [u_{bj}(\mu\varphi_{b,i}\varphi_{a,j} + \lambda\varphi_{b,j}\varphi_{a,i} + \mu\delta_{ij}\varphi_{b,k}\varphi_{a,k})] dv \tag{4.89}$$

and hence we obtain that

$$K_{ab,ij} = \int_\Omega (\mu\varphi_{b,i}\varphi_{a,j} + \lambda\varphi_{b,j}\varphi_{a,i} + \mu\delta_{ij}\varphi_{b,k}\varphi_{a,k}) dv \tag{4.90}$$

It is also easy to check that $\mathbf{K}$ is symmetric, i.e. $\mathbf{K}_{ab} = \mathbf{K}_{ba}^T$.
The diffusion equation is discretized similarly to the model problem we considered in Chapter 2. However, we now have a nonlinearity in the diffusion coefficient and an additional advection term due to the pressure term.

Namely, we consider the concentration equation in the following form

$$\int_\Omega c_{,t}\psi + D\left(\nabla c - \frac{\Omega c}{RT}\nabla\sigma_h\right)\cdot\nabla\psi dv + \int_{\partial\Omega} g\psi da =$$
$$\int_\Omega c_{,t}\psi + D\left((1+\gamma c)\nabla c - \frac{\Omega c}{RT}\nabla\sigma_{eh}\right)\cdot\nabla\psi dv + \int_{\partial\Omega} g\psi da =$$
$$\int_\Omega c_{,t}\psi + D\left((1+\gamma c)\nabla c - c\mathbf{v}_{eh}\right)\cdot\nabla\psi dv + \int_{\partial\Omega} g\psi da = 0 \tag{4.91}$$

where σ_{eh} is the part of the hydrostatic stress (4.69), without the concentration term and we have denoted $\gamma = \frac{\Omega\beta}{RT}$ and $\mathbf{v}_{eh} = \frac{\Omega}{RT}\nabla\sigma_{eh}$. This is an advection-diffusion type of equation for the concentration, with a non-linear diffusion coefficient. Since the discrete stress is discontinuous across element boundaries, in order to obtain nodal values for σ_h, we take the average of its values from all elements that meet in the respective node. The discretized concentration equation is

$$\int_\Omega \frac{c_h^{n+1}-c_h^n}{\Delta t}\varphi_i + D\left((1+\gamma c_h^{n+1})\nabla c_h^{n+1} - c_h^{n+1}\mathbf{v}_{eh}\right)\cdot\nabla\varphi_i dv + \int_{\partial\Omega} g\varphi_i da = 0 \tag{4.92}$$

The elements of the Jacobi matrix are

$$\frac{\partial R_i}{\partial c_j} = \int_\Omega \frac{\varphi_i\varphi_j}{\Delta t} + D\left((1+\gamma\varphi_j)\nabla c_h^{n+1} + (1+\gamma c_h^{n+1})\nabla\varphi_j - \varphi_j\mathbf{v}_{eh}\right)\cdot\nabla\varphi_i dv \tag{4.93}$$

4.2.3 Results

We first test our program against a known solution obtained in the paper [105]. It is for a spherical particle, where we apply a constant current density of $2A/m^2$ on the surface of the sphere. In Figure 4.1 we show the distribution of the concentration after 1000s of simulation. These values are in good agreement with the ones from the paper. As one can see from Figure 4.1 when we apply this model to a spherical particle, we have a uniform increase in the diffusion speed.

We also test with the same model but on a perforated cylindrical particle, where the perforation is also a cylinder with the same height, but smaller radius (Figure 4.2). On this geometry we study several scenarios. We test

with different boundary conditions for the stresses, i.e. with zero traction boundary (no stress) and a constant pressure value. We also test these two cases, when bases of the cylinder are free or when they are fixed in the z direction, essentially leading to radial solutions. The outer radii of the bases are $5\mu m$, the inner radii of the bases are $1\mu m$ and the height of the cylinders is $25\mu m$, i.e.

$$\Omega = \{(x_1, x_2, x_3) | 10^{-6} \leq \sqrt{x_1^2 + x_2^2} \leq 5 \times 10^{-6}, \quad x_3 \in [0, 25 \times 10^{-6}]\}$$

It is discretized by 2700 hexahedral elements and 3200 vertices. Let us denote the inner wall by

$$\Gamma_I = \{(x_1, x_2, x_3) | \sqrt{x_1^2 + x_2^2} = 10^{-6}, \quad x_3 \in [0, 25 \times 10^{-6}]\}$$

the top and bottom bases by

$$\Gamma_B = \{(x_1, x_2, x_3) | 10^{-6} \leq \sqrt{x_1^2 + x_2^2} \leq 5 \times 10^{-6}, \quad x_3 \in \{0\} \cup \{25 \times 10^{-6}\}\}$$

and the external wall by

$$\Gamma_O = \{(x_1, x_2, x_3) | \sqrt{x_1^2 + x_2^2} = 5 \times 10^{-6}, \quad x_3 \in [0, 25 \times 10^{-6}]\}$$

We use the following boundary conditions

$$\mathbf{u}(\mathbf{x}) = 0, \quad \mathbf{x} \in \Gamma_I \tag{4.94}$$

$$\boldsymbol{\sigma} \cdot \mathbf{n}(\mathbf{x}) = 0, \quad \mathbf{x} \in \Gamma_O \tag{4.95}$$

$$\boldsymbol{\sigma} \cdot \mathbf{n}(\mathbf{x}) = -p\mathbf{n}, \quad \mathbf{x} \in \Gamma_O \tag{4.96}$$

$$-D\left(\nabla c - \frac{\Omega c}{RT}\nabla\sigma_h\right) \cdot \mathbf{n}(\mathbf{x}) = 2A/m^2, \quad \mathbf{x} \in \Gamma_O \tag{4.97}$$

$$-D\left(\nabla c - \frac{\Omega c}{RT}\nabla\sigma_h\right) \cdot \mathbf{n}(\mathbf{x}) = 0, \quad \mathbf{x} \in \Gamma_I \cup \Gamma_B \tag{4.98}$$

$$c(\mathbf{x}, 0) = 0, \quad \mathbf{x} \in \Omega \tag{4.99}$$

where for p we use either zero or a constant value of 200MPa. This is motivated by Dreyer et al. [34] where researchers show that the pressure on the boundary is not zero and can indeed reach such levels. For the other parameters we use the same values as Zhang et al. [105] given in Table 4.1.

Table 4.1: Parameters for Mn_2O_4

Symbol	Name	Value
D	Diffusion constant	$10^{-14}\text{m}^2/\text{s}$
E	Young's modulus	10 GPa
ν	Poisson's ratio	0.3
Ω	Partial molar volume	$3.497 \times 10^{-6}\text{m}^3/\text{mol}$
c_{max}	Maximum concentration	2.29×10^4 mol/m^3

In Figure 4.3 we show the lithium distribution in the cylindrical particle after 1000 seconds. One can observe that since we do not restrict the cylinder at the bases in the z direction, we have spatial variation in the hydrostatic stress along the height of the cylinder and consequently variations in the concentration. Notice that such variations are not present in Figure 4.3a, but rather only in the ones where we take into account the stress effects. Such variation is present for both the zero traction and the 200MPa pressure boundary condition cases. This point is further illustrated in Figures 4.4, 4.5 and 4.6 where we take lineouts of the concentration along the radial direction at the middle and at the base of the cylinder, and along the height of the cylinder at the internal boundary, respectively. Notice that in order for the concentration to have a more uniform distribution, the values near the inner wall have to be higher than the reference concentration (i.e. the one without stress) and the values near the outer wall have to be lower. We can see from Figure 4.4 that this is true in the middle of the cylinder for both stress test cases. Also, the case where we apply pressure leads to better uniformity than both other cases. However, near the bases we observe from Figure 4.5 that this is no longer universally true. For both cases, in which we account for the stress, near the inner wall we have lower values than the reference concentration. For the rest of the values, for the zero traction case, we have values that are very near the reference, and slightly lower at the outer wall. For the applied pressure case, we have a noticeable acceleration of the lithium transport from the outer to the inner wall, when looking at values that are away from the inner wall. In Figure 4.6, which is a lineout of the concentration values on the inner wall, we can also observe that away from the bases, the behavior is consistent with a more uniform distribution of the concentration, i.e. the values are higher when we account for the stress effects.

When we fix the displacement at the bases in the z direction i.e. $u_3(\mathbf{x}) = 0, \mathbf{x} \in \Gamma_B$, the stress field assumes a variation only in the radial direction. This leads to an uniform distribution along the height for the concentration and in fact, the values of the concentration are virtually the same for the

two cases as shown in the lineout in Figure 4.7. Since the hydrostatic stress is included in the diffusion equation only with its gradient, this points to the hydrostatic stresses in the two cases being different with only a constant value. The hydrostatic stresses for the two cases are shown in Figure 4.8a and their difference in Figure 4.8b. We observe that, indeed, the maximum and minimum values in Figure 4.8b differ by only about 0.5MPa. In Figure 4.9 we can see that the values for the Von Mises stress (4.48) are also about two times higher for the case with constant pressure on the boundary.
Next we move on to the comparison between solving equation (4.63) with constant Neumann boundary conditions and solving it coupled to the full electrochemical model. This is important because even though the total flux across the interface is the same, the boundary condition for the full electrochemical model would have spatial variations. This would of course lead to spatial variations in the value for the lithium ion concentration. The electrochemical parameters for the simulation are taken from Table 3.2 and the mechanical parameters are taken from Table 4.1. For this simulation we only couple the mechanics to the diffusion in the anode and use the usual diffusion equation for the cathode. Note that the electrochemical parameters (especially the material specific open-circuit potential U_0) are for graphite while the mechanical parameters are for Mn_2O_4. However, the mechanical parameters are also in the admissible range for graphite and hence it is justified to use them. We solve for the cylindrical particles geometry from Chapter 3. For boundary conditions we use fixed displacement on the external boundary of the anode, i.e. $\mathbf{u}(\mathbf{x}) = 0, \mathbf{x} \in \Gamma_a$ and zero traction on Γ_I where we use the notations from Chapter 3.
In Figure 4.10 we show the values for i_{se}, i.e. the one from the interface conditions, after 1000 seconds. It is obvious that there is, indeed, a spatial variation. In Figures 4.11 and 4.12 we show the concentration for the simple model and for the full electrochemical model. We can easily see that the values on the interface are distributed differently. Likewise, from Figures 4.13 and 4.14 we can observe that the same is also true for the hydrostatic stress. However, in Figures 4.15 and 4.16 we see that the same does not hold true for the Von Mises stress where both the values and the distributions are close to each other. It seems that the fact, that we fix the displacement in all directions on the external boundary of the anode, affects the Von Mises stress more than the difference in the spatial distribution of the concentration between the two models.

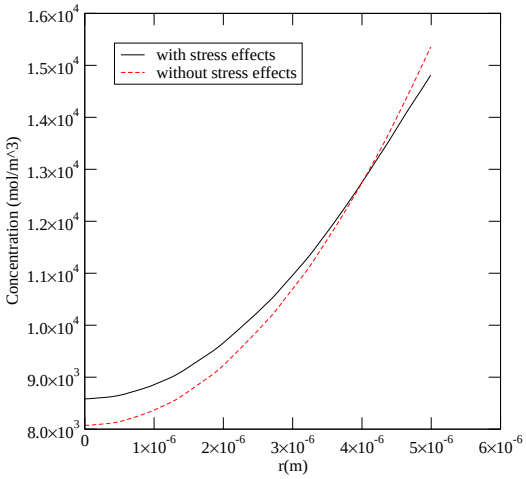

Figure 4.1: Lithium concentration ($\frac{mol}{m^3}$) distribution along the radial direction of a spherical particle with and without stress effects

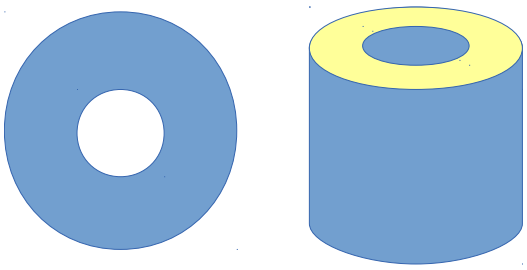

Figure 4.2: Geometry for a cylindrical particle

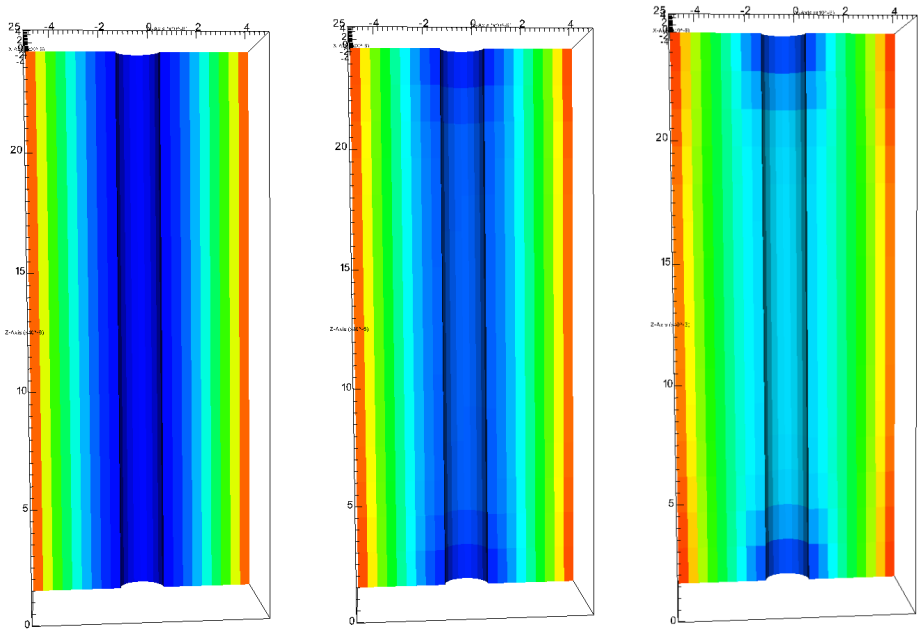

(a) without stress effects (b) stress effects and zero traction boundary conditions (c) with stress effects and 200MPa constant pressure boundary conditions

Figure 4.3: Lithium concentration ($\frac{mol}{m^3}$) after 1000s

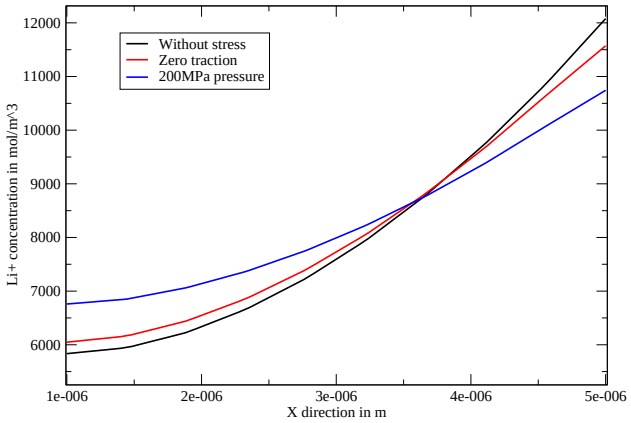

Figure 4.4: Lithium concentration ($\frac{mol}{m^3}$) distribution along the radial direction of a cylindrical particle for z = 12.5e-6 with and without stress effects

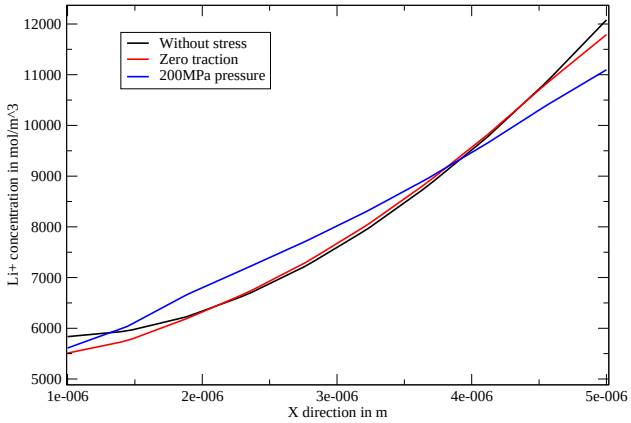

Figure 4.5: Lithium concentration ($\frac{mol}{m^3}$) distribution along the radial direction of a cylindrical particle for z = 0 with and without stress effects

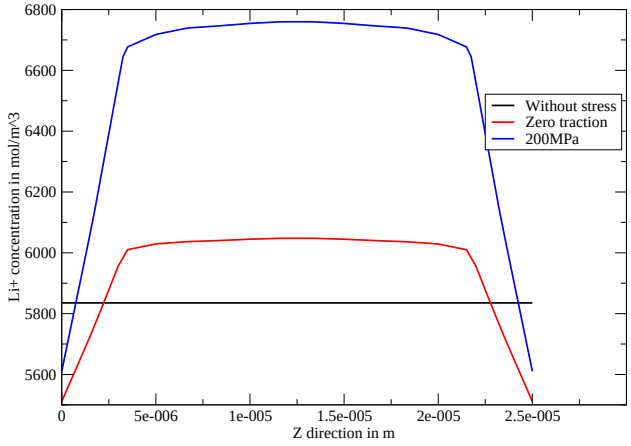

Figure 4.6: Lithium concentration ($\frac{mol}{m^3}$) distribution along the z direction of a cylindrical particle near the inner cylinder with and without stress effects

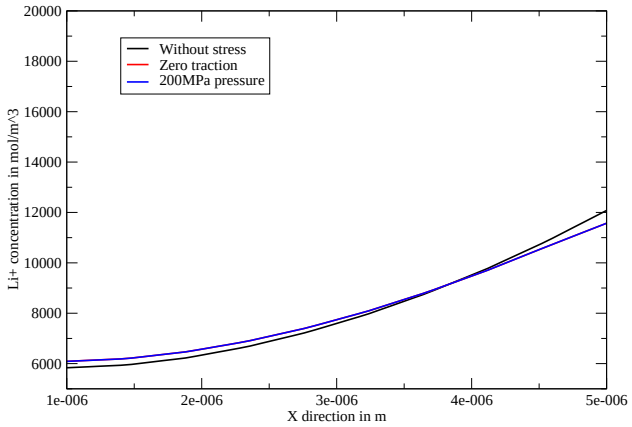

Figure 4.7: Lithium concentration ($\frac{mol}{m^3}$) distribution along the radial direction of a cylindrical particle for z = 0 with and without stress effects and fixed discplacement in the z direction. The red and blue lines coincide

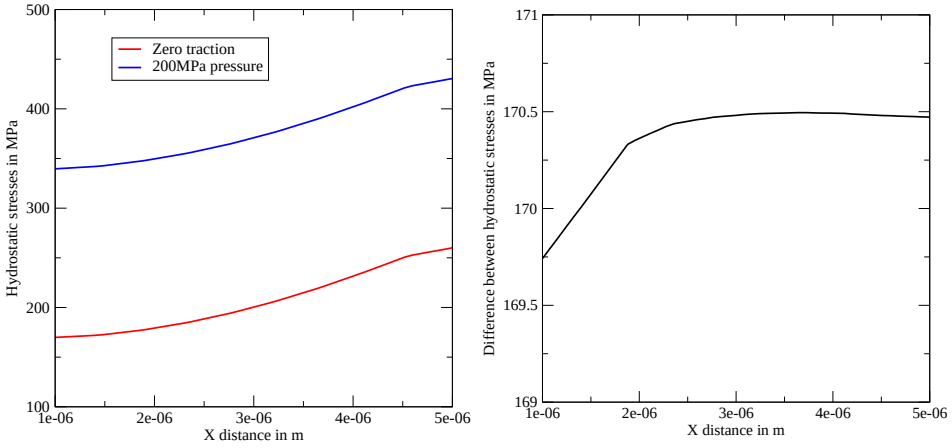

(a) Hydrostatic stress

(b) Difference in hydrostatic stresses

Figure 4.8: Hydrostatic stress (Pa) along the radial direction of a cylindrical particle for z = 0 with fixed discplacement in the z direction

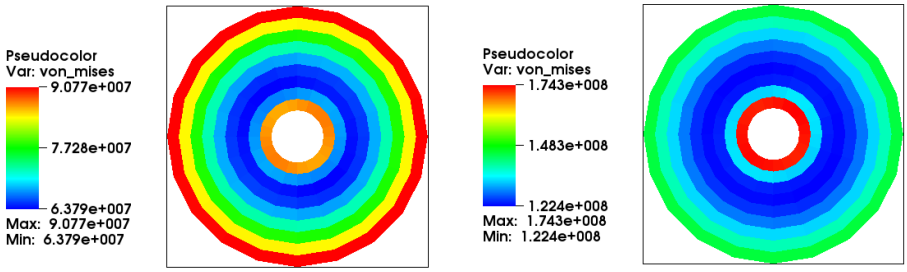

(a) zero traction boundary (b) 200MPa constant pressure boundary

Figure 4.9: Von Mises stress (Pa) for cylinder

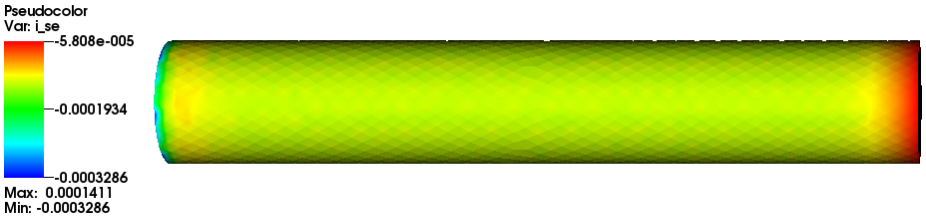

Figure 4.10: Value of i_{se} in a cylindrical particle after 1000s for 1C current

Figure 4.11: Concentration ($\frac{mol}{cm^3}$) in a cylindrical particle using the pure diffusion model after 1000s for 1C current

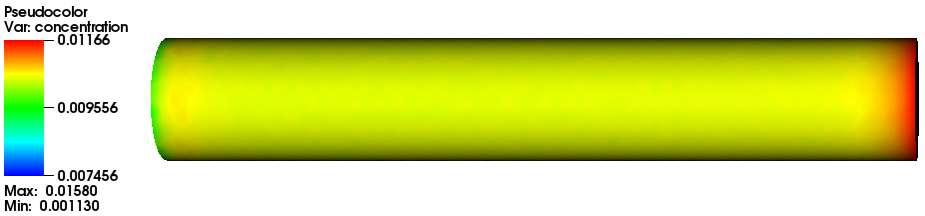

Figure 4.12: Concentration ($\frac{mol}{cm^3}$) in a cylindrical particle using the full electrochemical model after 1000s for 1C current

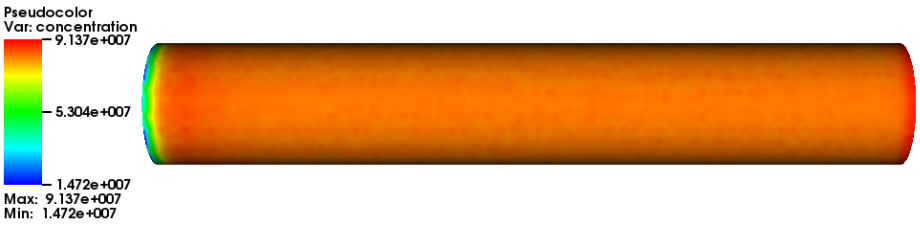

Figure 4.13: Hydrostatic stress (Pa) in a cylindrical particle using the pure diffusion model after 1000s for 1C current

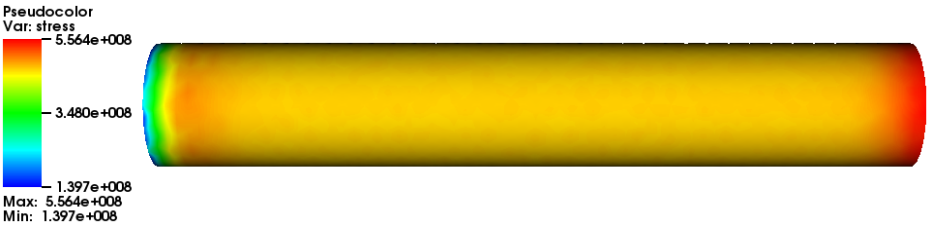

Figure 4.14: Hydrostatic stress (Pa) in a cylindrical particle using the full electrochemical model after 1000s for 1C current

Figure 4.15: Von Mises stress (Pa) in a cylindrical particle using the pure diffusion model after 1000s for 1C current

Figure 4.16: Von Mises stress (Pa) in a cylindrical particle using the full electrochemical model after 1000s for 1C current

4.3 Finite strain

Finite strain chemomechanical models for lithium-ion batteries are still relatively rare. Christensen and Newman [22] use Hooke's law to relate the Cauchy stress and the Eulerian strain, and use an additive split for the stresses. Bower et al. [10] use finite strains and also use a multiplicative decomposition for the chemical strains and elasto-plastic strains. They couple the second Piola-Kichhoff stress to the Green-Lagrange strain. Bower et al. [9] further couple this model to fracture and use it in FEM simulations. Similar model for elasto-plastic deformation, also with a multiplicative decomposition for the deformation gradient, is used by Zhao et al. [106]. In the latter model, the researchers couple the Cauchy stress to the logarithmic strain.
In our simulation, we are using a multiplicative decomposition of the deformation gradient, to account for the chemical straining. The elastic mechanical models we consider are the same elastic models used by Bower et al. [10] and by Zhao et al. [106]. These are also popular elastic models used in solid mechanics [7, 24]. We compare the two models, to study the range of stresses and strains obained by the different models, for realstic parameters used in batteries. We also include a dependence on the concentration for the Young's modulus. Since we use hyperelastic mechanical models, a short description is given in Section 4.3.1. Next, in Section 4.3.2 we present the models we consider. In Section 4.3.3 is given the discretization of the problem. Finally, in Section 4.3.4 we show our numerical results.

4.3.1 Hyperelasticity

For this section we mostly follow the book by Bonet and Wood [7] in the explanation. In hyperelasticity the main assumption is that the state of behavior of the materials can be determined from the current configuration only. After removal of the loads, the body restores its original configuration. We express hyperelastic laws using a stored strain energy function

$$\Psi = \Psi(\mathbf{C}) \tag{4.100}$$

which in our case is a function of the right Cauchy-Green deformation tensor. We find the second Piola-Kirchoff stress tensor by differentiating the elastic stored strain energy with respect to $\mathbf{E}$ to obtain

$$\mathbf{S}(\mathbf{C}, \mathbf{X}) = 2\frac{\partial \Psi}{\partial \mathbf{C}} = \frac{\partial \Psi}{\partial \mathbf{E}}; S_{IJ} = \frac{\partial \Psi}{\partial E_{IJ}} \tag{4.101}$$

We are mainly interested in isotropic materials where the material response is the same in any direction. For such materials we can consider the elastic potential to be a function only of the invariants of $\mathbf{C}$ (given in Section 2.7), namely

$$\Psi = \Psi(I_C, II_C, III_C) \tag{4.102}$$

and the second Piola-Kirchoff stress becomes

$$\mathbf{S} = 2\frac{\partial \Psi}{\partial \mathbf{C}} = 2\frac{\partial \Psi}{\partial I_C}\frac{\partial I_C}{\partial \mathbf{C}} + 2\frac{\partial \Psi}{\partial II_C}\frac{\partial II_C}{\partial \mathbf{C}} + 2\frac{\partial \Psi}{\partial III_C}\frac{\partial III_C}{\partial \mathbf{C}} \tag{4.103}$$

where the derivatives of the invariants with respect to $\mathbf{C}$ are given in Section 2.7. Therefore we have

$$\begin{aligned}
\mathbf{S} &= 2\frac{\partial \Psi}{\partial I_C}\mathbf{I} + 2\frac{\partial \Psi}{\partial II_C}\mathbf{C} + 2J^2\frac{\partial \Psi}{\partial III_C}\mathbf{C}^{-1} && (4.104)\\
&= 2\frac{\partial \Psi}{\partial I_C}\mathbf{Q}\mathbf{Q}^T + 2\frac{\partial \Psi}{\partial II_C}\mathbf{Q}\mathbf{\Lambda}^2\mathbf{Q}^T + 2J^2\frac{\partial \Psi}{\partial III_C}\mathbf{Q}\mathbf{\Lambda}^{-2}\mathbf{Q}^T \\
&= \mathbf{Q}\mathbf{\Lambda}_S\mathbf{Q}^T && (4.105)\\
\mathbf{\Lambda}_S &= 2\mathrm{diag}\left(\frac{\partial \Psi}{\partial I_C} + \frac{\partial \Psi}{\partial II_C}\lambda_i^2 + J^2\frac{\partial \Psi}{\partial III_C}\lambda_i^{-2}\right) && (4.106)
\end{aligned}$$

where it is easy to see that the term in the brackets is

$$\frac{\partial \Psi(I_C, II_C, III_C)}{\partial \lambda_i^2} = \frac{\partial \Psi}{\partial I_C}\frac{\partial I_C}{\partial \lambda_i^2} + \frac{\partial \Psi}{\partial II_C}\frac{\partial II_C}{\partial \lambda_i^2} + \frac{\partial \Psi}{\partial III_C}\frac{\partial III_C}{\partial \lambda_i^2} \tag{4.107}$$

and also

$$\frac{\partial \Psi}{\partial \lambda_i^2} = \frac{1}{2\lambda_i}\frac{\partial \Psi}{\partial \lambda_i} \tag{4.108}$$

The Cauchy stress is

$$\begin{aligned}
\boldsymbol{\sigma} &= \frac{1}{J}\mathbf{F}\mathbf{S}\mathbf{F}^T \\
&= \frac{1}{J}\mathbf{q}\mathbf{\Lambda}\mathbf{Q}^T\mathbf{Q}\mathbf{\Lambda}_S\mathbf{Q}^T\mathbf{Q}\mathbf{\Lambda}\mathbf{q}^T \\
&= \frac{1}{J}\mathbf{q}\mathbf{\Lambda}_\sigma\mathbf{q}^T && (4.109)\\
\mathbf{\Lambda}_\sigma &= \mathrm{diag}(\sigma_i) = \mathrm{diag}\left[\lambda_i\left(\frac{\partial \Psi}{\partial \lambda_i}\right)\right] && (4.110)
\end{aligned}$$

The values σ_i are called principal stresses.

4.3.2 Model

In the finite strain case, we no longer use the additive split of the mechanical and chemical strains. We assume that we can decompose the deformation into an elastic deformation, resulting from mechanical processes and a chemical deformation resuling from the intercalation of lithium ions. With this assumption in mind, the deformation gradient is split in an elastic and a chemical part

$$\mathbf{F} = \mathbf{F}_e\mathbf{F}_c \tag{4.111}$$

and also due to the properties of the determinant

$$J = \det(\mathbf{F}) = \det(\mathbf{F}_e)\det(\mathbf{F}_c) = J_eJ_c \tag{4.112}$$

Such a split is also used in large deformation analysis in other settings such as finite strain elasto-plasticity [60], finite strain thermoelasticity [88], etc. As in the small strain case, we again assume that the chemical expansion is isotropic and the chemical deformation gradient has the following general representation

$$\mathbf{F}_c = \alpha_T(c)\mathbf{I} \tag{4.113}$$

This representation is also used by other researchers [10, 106].
We also use the definition of the volume expansion coefficient as in Ryu et al.[78] where they assume a linear expansion with respect to the number of lithium ions, i.e.

$$V_{current} = V_{si} + \Omega n_{Li} \tag{4.114}$$

where Ω is again the partial molar volume and n_{Li} is the number of deposited lithium ions. Due to the definition of concentration

$$c = \frac{n_{Li}}{V_{current}} \tag{4.115}$$

the volumetric expansion coefficient they obtain [78] is

$$\alpha_V = \frac{\Omega}{1 - \Omega c} \tag{4.116}$$

Finally, the form that we use for $\mathbf{F}_c$ is

$$\mathbf{F}_c = (1 + \alpha_V c)^{1/3}\mathbf{I} \tag{4.117}$$

We can now determine $\mathbf{F}_e$ as

$$\mathbf{F}_e = \mathbf{F}\mathbf{F}_c^{-1} = (1 + \alpha_V c)^{-1/3}\mathbf{F} \tag{4.118}$$

We use two different elastic material laws for $\mathbf{F}_e$ to test the dependence of the results on the specific model. Note that the second Piola-Kirchhof stress is given as

$$\mathbf{S} = \frac{\partial \Psi_e}{\partial \mathbf{E}_e} \tag{4.119}$$

where $\mathbf{E}_e = \frac{1}{2}(\mathbf{F}_e^T\mathbf{F}_e - \mathbf{I})$ is the elastic Green-Lagrange strain. And in general we use here the notation with subscript e to denote quantities obtained with respect to the elastic deformation gradient $\mathbf{F}_e$.
The first model is given for the second Piola-Kirchoff stress tensor with respect to the elastic Green-Lagrange strain as

$$\mathbf{S} = J_c(2\mu(c)\mathbf{E}_e + (\lambda(c)\mathrm{tr}\mathbf{E}_e)\mathbf{I}) \tag{4.120}$$

and is known as St. Venant-Kirchoff model. This expession for the second Piola-Kirchoff stress can be obtained from the stored elastic strain energy function

$$\Psi_e(\mathbf{E}_e) = J_c\left(\mu(c)\mathbf{E}_e : \mathbf{E}_e + \frac{1}{2}\lambda(c)(\mathrm{tr}\mathbf{E}_e)^2\right) \tag{4.121}$$

We can also rewrite it as a function of the elastic stretches λ_{ei} as

$$\begin{aligned}\Psi_e(\lambda_{e1}, \lambda_{e2}, \lambda_{e3}) = J_c\Bigg(&\frac{\mu(c)}{4}(\lambda_{e1}^4 + \lambda_{e2}^4 + \lambda_{e3}^4 - 2(\lambda_{e1}^2 + \lambda_{e2}^2 + \lambda_{e3}^2) + 3) + \\ &\frac{\lambda(c)}{8}(\lambda_{e1}^2 + \lambda_{e2}^2 + \lambda_{e3}^2 - 3)^2\Bigg)\end{aligned} \tag{4.122}$$

In order to solve the model on the current configuration we need to find $\boldsymbol{\sigma}$ either by the push forward of $\mathbf{S}$ which in this case is

$$\boldsymbol{\sigma} = \frac{1}{J}\mathbf{F}_e\mathbf{S}\mathbf{F}_e^T \tag{4.123}$$

or by directly using Equations (4.110) and (4.122) to obtain the principal stresses. Either way we obtain

$$\sigma_i = \frac{1}{J_e}[\mu(\lambda_{ei}^4 - \lambda_{ei}^2) + \frac{\lambda}{2}(\lambda_{e1}^2 + \lambda_{e2}^2 + \lambda_{e3}^2 - 3)\lambda_{ei}^2] \tag{4.124}$$

The second model is given for the Cauchy stress with respect to the elastic logarithmic strain by

$$\sigma_i = \frac{2\mu(c)}{J_e} \ln \lambda_{ei} + \frac{\lambda(c)}{J_e} \ln J_e \tag{4.125}$$

It can also be written as

$$\boldsymbol{\sigma} = \frac{2\mu(c)}{J_e} \mathbf{e}_{0e} + \frac{\lambda(c)}{J_e} \mathrm{tr}(\mathbf{e}_{0e}) \mathbf{I} \tag{4.126}$$

The respective stored elastic strain energy function for this model is

$$\Psi_e = J_c \mu(c) [(\ln \lambda_{e1})^2 + (\ln \lambda_{e2})^2 + (\ln \lambda_{e3})^2] + J_c \frac{\lambda(c)}{2} (\ln J_e)^2 \tag{4.127}$$

As we already mentioned in the introduction to this chapter, the two models are popular elastic models from literature [7, 24]. Actually, it is easy to see why – in practice these two models give a Hooke's law-like relation for the different stress and strain measures. Namely, Equation (4.120) is Hooke's law between the second Piola-Kirchhoff stress and the Green-Lagrange strain, and Equation (4.126) is almost Hooke's law between the Cauchy stress and the logarithmic strain, with the difference being the presence of J_e in the denominator. Zhao et al. [106] also use the second model (4.125), but they further introduce a plastic stretch and assume the elastic deformation is isochoric. In this section we focus mainly on the influence of the concentration on the mechanical stress and omit the back coupling of the influence of stress on the lithium transport. In that sense we couple the equilibrium equation to the simple diffusion equation where we do not account for the stress effects. The only influence left is the deforming domain, where the equations are posed. Finally, we use the following expression for Young's modulus

$$E(c) = E_{Si} + \gamma_E c \tag{4.128}$$

since we have a phase change in the material and the final composition can potentially have vastly differing material properties than the original one. Linear dependence of elastic parameters on the concentration in general applications (not restricted to batteries) are also considered by other researchers, e.g. [102]. In the context of batteries, a concentration dependent Young's modulus is also used by, e.g. [10, 28]. Experimentally, Boles et al. [6] show that a fully lithiated Silicon has a much lower elastic modulus than pure Silicon and Shenoy et al. [85] show an almost linear dependence on the lithium fraction $\frac{x}{1+x}$ in $\mathrm{Li}_x\mathrm{Si}$, using a first-principles study.

4.3.3 Discretization

Here we give the discretization of the problem. For simplicity, in this section, we do not use the subscripts for the different configurations, but rather treat the problem as if it were a regular problem from solid mechanics. Due to the specifics of our problem the two descriptions would be almost the same, up to a difference in subscripts.
In order to fully discretize and solve the finite strain equilibrium equations we need both discretization and linearization. Let us rewrite equation (4.36) denoting the term on the left hand side a residual and putting $\mathbf{f}$ and $\mathbf{t}$ to zero since we do not consider in this model neither body nor surface external forces, i.e.

$$R(\mathbf{x}) = \int_{\Omega} \boldsymbol{\sigma} : \nabla \boldsymbol{\psi} dv \tag{4.129}$$

$$\tag{4.130}$$

and as usual we solve

$$R(\mathbf{x}) = 0 \tag{4.131}$$

In this instance we do the linearization using directional derivatives for convenience

$$R + DR[u] = 0 \tag{4.132}$$

For simplicity the directional derivative is sought on the reference configuration, where for the residual we use the left hand side of equation (4.47). We have

$$\begin{aligned}
DR[u] &= \int_{\Omega_0} D(\mathbf{S} : \mathbf{F}^T \nabla_0 \boldsymbol{\psi})[u] dV \\
&= \int_{\Omega_0} \mathbf{F}^T \nabla_0 \boldsymbol{\psi} : D(\mathbf{S})[u] dV + \int_{\Omega_0} \mathbf{S} : D(\mathbf{F}^T \nabla_0 \boldsymbol{\psi})[u] dV \\
&= \int_{\Omega_0} \mathbf{F}^T \nabla_0 \boldsymbol{\psi} : \mathcal{C} : D(\mathbf{E})[u] dV + \int_{\Omega_0} \mathbf{S} : D(\mathbf{F}^T)[u] \nabla_0 \boldsymbol{\psi} dV \\
&= \int_{\Omega_0} \mathbf{F}^T \nabla_0 \boldsymbol{\psi} : \mathcal{C} : 0.5(\nabla_0 \mathbf{u}^T \mathbf{F} + \mathbf{F}^T \nabla_0 \mathbf{u}) dV + \int_{\Omega_0} \mathbf{S} : \nabla_0 \mathbf{u}^T \nabla_0 \boldsymbol{\psi} dV \\
&= \int_{\Omega_0} \mathbf{F}^T \nabla_0 \boldsymbol{\psi} : \mathcal{C} : \mathbf{F}^T \nabla_0 \mathbf{u} dV + \int_{\Omega_0} \mathbf{S} : \nabla_0 \mathbf{u}^T \nabla_0 \boldsymbol{\psi} dV
\end{aligned} \tag{4.133}$$

We used that

$$D(\mathbf{S})[u] = \frac{\partial \mathbf{S}}{\partial \mathbf{E}} : D\mathbf{E}[u] = \mathcal{C} : D\mathbf{E}[u] \tag{4.134}$$

where we denoted with $\mathcal{C}$ the 4th order material elaticity tensor. Its elements are given by

$$C_{IJKL} = \frac{\partial S_{IJ}}{\partial E_{KL}} = 4\frac{\partial^2 \Psi}{\partial C_{IJ} \partial C_{KL}} = C_{KLIJ} \tag{4.135}$$

Besides that major symmetry written above, $\mathcal{C}$ also has two minor symmetries [7], i.e. $C_{IJKL} = C_{IJLK}$ and $C_{IJKL} = C_{JIKL}$. Due to them we have that

$$\mathcal{C} : \mathbf{A} = \mathcal{C} : \mathbf{A}^T \tag{4.136}$$

The directional derivative of $\mathbf{F}$ is

$$D\mathbf{F}[u] = \left(\frac{d}{d\varepsilon} \nabla_0 (\mathbf{x} + \varepsilon \mathbf{u}) \right) \Big|_{\varepsilon=0} = \nabla_0 \mathbf{u} \tag{4.137}$$

and the directional derivative of $\mathbf{E}$ is

$$\begin{aligned} D\mathbf{E}[u] &= \frac{1}{2} \left(\frac{d}{d\varepsilon} [\nabla_0 (\mathbf{x} + \varepsilon \mathbf{u})^T \nabla_0 (\mathbf{x} + \varepsilon \mathbf{u}) - \mathbf{I}] \right) \Big|_{\varepsilon=0} \\ &= \frac{1}{2} (\mathbf{F}^T \nabla_0 \mathbf{u} + \nabla_0 \mathbf{u}^T \mathbf{F}) \end{aligned} \tag{4.138}$$

Using (4.39) for the spatial derivatives, the directional derivative (4.133) of R in the current domain is

$$\begin{aligned} &\int_\Omega J^{-1} \mathbf{F}^T \nabla \boldsymbol{\psi} \mathbf{F} : \mathcal{C} : \mathbf{F}^T \nabla \mathbf{u} \mathbf{F} dv + \int_\Omega J^{-1} \mathbf{S} : \mathbf{F}^T \nabla \mathbf{u}^T \nabla \boldsymbol{\psi} \mathbf{F} dv \\ &= \int_\Omega \nabla \boldsymbol{\psi} : \mathbf{c} : \nabla \mathbf{u} dv + \int_\Omega \boldsymbol{\sigma} : \nabla \mathbf{u}^T \nabla \boldsymbol{\psi} dv \end{aligned} \tag{4.139}$$

where the spatial elasticity tensor $\mathbf{c}$ is given by

$$\mathbf{c}_{ijkl} = J^{-1} F_{iI} F_{jJ} F_{kK} F_{lL} C_{IJKL} \tag{4.140}$$

The first integral simplified due to

$$\begin{aligned} &\int_\Omega J^{-1} \mathbf{F}^T \nabla \boldsymbol{\psi} \mathbf{F} : \mathcal{C} : \mathbf{F}^T \nabla \mathbf{u} \mathbf{F} dv \\ &= \int_\Omega J^{-1} F_{iI} \psi_{i,j} F_{jJ} C_{IJKL} F_{kK} u_{k,l} F_{lL} dv \\ &= \int_\Omega \nabla \boldsymbol{\psi} : \mathbf{c} : \nabla \mathbf{u} dv \end{aligned} \tag{4.141}$$

and the second due to

$$\begin{aligned}
&\int_\Omega J^{-1}\mathbf{S} : \mathbf{F}^T\nabla\mathbf{u}^T\nabla\boldsymbol{\psi}\mathbf{F}dv \\
&= \int_\Omega J^{-1}\mathrm{tr}(\mathbf{S}^T\mathbf{F}^T\nabla\mathbf{u}^T\nabla\boldsymbol{\psi}\mathbf{F})dv \\
&= \int_\Omega J^{-1}\mathrm{tr}(\nabla\mathbf{u}^T\nabla\boldsymbol{\psi}\mathbf{F}\mathbf{S}^T\mathbf{F}^T)dv \\
&= \int_\Omega J^{-1}\mathbf{F}\mathbf{S}\mathbf{F}^T : \nabla\mathbf{u}^T\nabla\boldsymbol{\psi}dv \\
&= \int_\Omega \boldsymbol{\sigma} : \nabla\mathbf{u}^T\nabla\boldsymbol{\psi}dv
\end{aligned} \tag{4.142}$$

We now use the following discretizations

$$\mathbf{X} = \sum_{i=1}^{N}\varphi_i(\boldsymbol{\xi})\mathbf{X}_i \tag{4.143}$$

for the initial coordinates and

$$\mathbf{x} = \sum_{i=1}^{N}\varphi_i(\boldsymbol{\xi})\mathbf{x}_i(t) \tag{4.144}$$

for the current coordinates. We also interpolate the displacement $\mathbf{u}$

$$\mathbf{u} = \sum_{i=1}^{N}\varphi_i(\boldsymbol{\xi})\mathbf{u}_i(t) \tag{4.145}$$

In order to obtain the deformation gradient $\mathbf{F}$ at a point, we differentiate the interpolant for the current coordinates with respect to the original coordinates

$$\mathbf{F} = \sum_{i=1}^{N}\mathbf{x}_i\nabla_0\varphi_i^T \tag{4.146}$$

where the derivatives with respect to the initial configuration are computed as previously

$$\nabla_0\varphi_i = (\nabla_\xi\mathbf{X})^{-T}\nabla_\xi\varphi_i \tag{4.147}$$

We also have for the right and left Cauchy-green tensors

$$\mathbf{C} = \sum_{i,j} (\mathbf{x}_i \cdot \mathbf{x}_j) \nabla_0 \varphi_i \nabla_0 \varphi_j^T \tag{4.148}$$

$$\mathbf{B} = \sum_{i,j} (\nabla_0 \varphi_i \cdot \nabla_0 \varphi_j) \mathbf{x}_i \mathbf{x}_j^T \tag{4.149}$$

For the discretized residual R for basis function a we have

$$\mathbf{R}_a = \int_\Omega \boldsymbol{\sigma} \nabla \varphi_a dv \tag{4.150}$$

For the first term in Equation (4.139) we have

$$\int_\Omega \nabla \boldsymbol{\psi} : \mathbf{c} : \nabla \mathbf{u}_h dv = \int_\Omega \psi_{i,j} c_{ijkl} u_{bk} \varphi_{b,l} dv \tag{4.151}$$

and when we make the analogy for discretizing each equation of the vector equilibrium equation separately as in the case for small strains, i.e. that $\boldsymbol{\psi} = \varphi_a \mathbf{e}_i$, we obtain the contribution to the stiffness matrix of the first term as

$$K^1_{ab,ik} = \int_\Omega \varphi_{a,j} c_{ijkl} \varphi_{b,l} dv \tag{4.152}$$

For the second term we have

$$\int_\Omega \boldsymbol{\sigma} : \nabla \mathbf{u}_h^T \nabla \boldsymbol{\psi} dv = \int_\Omega \sigma_{kl} u_{m,k} \psi_{m,l} dv = \int_\Omega \sigma_{kl} u_{bm} \varphi_{b,k} \psi_{m,l} dv \tag{4.153}$$

and making the same analogy as before, the contribution of this term to the stiffness matrix is

$$K^2_{ab,ij} = \int_\Omega \sigma_{kl} \varphi_{b,k} \varphi_{a,l} dv \tag{4.154}$$

and the total nodal contribution for basis functions a and b is

$$\mathbf{K}_{ab} = \mathbf{K}^1_{ab} + \mathbf{K}^2_{ab} \tag{4.155}$$

We do not show again the discretization of the diffusion equation, but we still have to make some notes. Remember that in disretized form over a stationary domain it is given by

$$\int_\Omega \frac{c_h^{n+1} - c_h^n}{\Delta t} \varphi_i dv + \int_\Omega D \nabla c_h^n \nabla \varphi_i dv + \int_{\partial\Omega} i_{appl} \varphi_i da = 0 \tag{4.156}$$

Even though we do not include the mechanical effects explicitly in the diffusion equation as was the case in the small strain models, the domain of integration still changes. However, since we solve the diffusion and the mechanics in semi-implicit fashion, from the point of view of the diffusion equation, the domain can be considered stationary. For the discretized in time volumetric integral of the time derivative, we need the concentration from the previous time step, obtained on the previous geometry, on the current geometry. We use the conservation of mass equation (4.9) from the previous geometry to the current geometry, i.e.

$$c(\mathbf{x}^n, t_n) = J_n^{n+1} c(\mathbf{x}^{n+1}, t_n) \tag{4.157}$$

where J_n^{n+1} is the Jacobian of the transformation from the geometry on time step n to the geometry on time step $n+1$ and $\mathbf{x}^n$ and $\mathbf{x}^{n+1}$ relate the coordinates in the two geometries between the two time steps.
For the boundary integral note that we want to preseve the total flux across the boundary. Then similarly to the boundary condition for the equilibrium equation (4.46) shown earlier, we have for the applied current density that

$$i_{appl}^0 = i_{appl}^{n+1} \frac{da}{dA} \tag{4.158}$$

and so we pull back the whole boundary integral on to the reference configuration. Finally we solve the diffusion equation as

$$\int\limits_{\Omega} \frac{c_h^{n+1} - \frac{c_h^n}{J_n^{n+1}}}{\Delta t} \varphi_i dv + \int\limits_{\Omega} D \nabla c_h^{n+1} \nabla \varphi_i dv + \int\limits_{\partial\Omega_0} i_{appl} \varphi_i dA = 0 \tag{4.159}$$

4.3.4 Results

We test several scenarios with single particles which are of parallelepiped initial shape. We study the dependence of the magnitudes of the stress and strain on the size of the particle. Our aim here is to reproduce behavior similar to experimental results for the stress [84] and to show that for larger particles relatively high mechanical strains can occur. We also compare the two models (4.120) and (4.127) on two geometries to study the sensitivity of the results on the specific material model. The sizes of the particles are $2\mu m \times 2\mu m \times 1\mu m$ for the bigger particle and $2\mu m \times 2\mu m \times 250nm$ for the smaller particle. We charge the particle only on the top surface, i.e. where $z = 1\mu m$. Due to symmetry considerations we take only one quadrant of the structures on the $x - y$ plane. We also assume that the resulting parallelepipeds are situated in the octant of the coordinate system where all

three coordinates are positive and the walls of the structure are parallel to the $x-y, y-z, x-z$ planes. We perform a charge-discharge cycle of the particle, where we charge the particle until some point reaches 0.7 state of charge and then reverse the current and discharge until some point reaches zero state of charge. In summary these are the test cases we consider

1. Parallelepiped particle with domain $\Omega_0 = \{[0, 10^{-6}]\times[0, 10^{-6}]\times[0, 10^{-6}]\}$ (see Figure 4.17a) used with the material model (4.120); one charge-discharge cycle is performed; 24389 hexahedral elements, 27000 nodes

2. Parallelepiped particle with domain $\Omega_0 = \{[0, 10^{-6}]\times[0, 10^{-6}]\times[0, 0.25\times 10^{-6}]\}$ (see Figure 4.17b) used with the material model (4.120); two charge-discharge cycles are performed; 13689 hexahedral elements, 16000 nodes

3. Parallelepiped particle with domain $\Omega_0 = \{[0, 10^{-6}]\times[0, 10^{-6}]\times[0, 0.25\times 10^{-6}]\}$ used with the material model (4.127); one charge-discharge cycle is performed; 13689 hexahedral elements, 16000 nodes

4. Parallelepiped particle with domain $\Omega_0 = \{[0, 10^{-6}]\times[0, 10^{-6}]\times[0, 10^{-6}]\}$ used with the material model (4.127); one charge-discharge cycle is performed; 24389 hexahedral elements, 27000 nodes

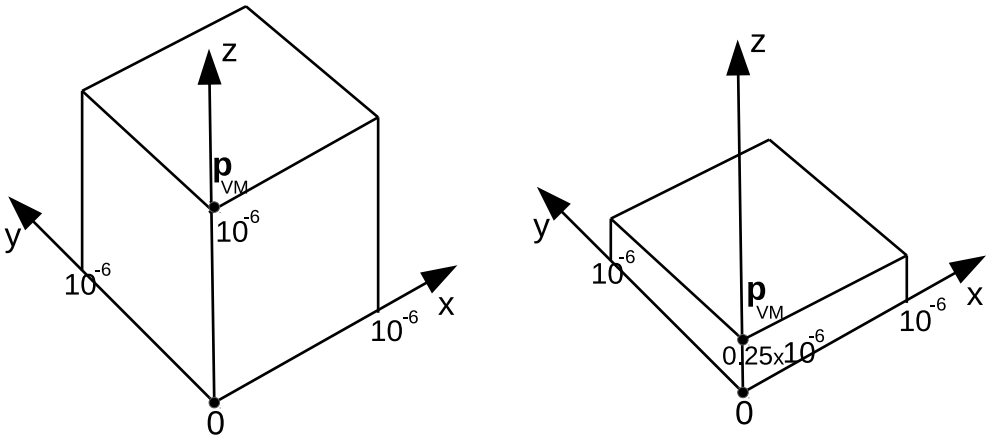

(a) Geometry for Test Cases 1 and 4

(b) Geometry for Test Cases 2 and 3

Figure 4.17: Geometries for finite strain experiments

The boundary conditions are as follows

$$u_1(\mathbf{X}) = 0, \quad \mathbf{X} \in \Gamma_x \tag{4.160}$$
$$\sigma_{ij} n_j = 0, \quad \mathbf{X} \in \Gamma_x, \quad i = 2,3 \tag{4.161}$$
$$u_2(\mathbf{X}) = 0, \quad \mathbf{X} \in \Gamma_y \tag{4.162}$$
$$\sigma_{ij} n_j = 0, \quad \mathbf{X} \in \Gamma_y, \quad i = 1,3 \tag{4.163}$$
$$u_3(\mathbf{X}) = 0, \quad \mathbf{X} \in \Gamma_z \tag{4.164}$$
$$\sigma_{ij} n_j = 0, \quad \mathbf{X} \in \Gamma_z, \quad i = 1,2 \tag{4.165}$$
$$\sigma_{ij} n_j = 0, \quad \mathbf{X} \in \Gamma_n \cup \Gamma_I, \quad i = 1,2,3 \tag{4.166}$$
$$\mathbf{N} \cdot \mathbf{n} = \frac{i_{appl}}{F}, \quad \mathbf{X} \in \Gamma_I \tag{4.167}$$
$$i_{appl} = 1.5 A/m^2 \tag{4.168}$$

where

$$\Gamma_x = \{\{0\} \times [0, 10^{-6}] \times [0, 10^{-6}]\}$$

$$\Gamma_y = \{[0, 10^{-6}] \times \{0\} \times [0, 10^{-6}]\}$$

$$\Gamma_z = \{[0, 10^{-6}] \times [0, 10^{-6}] \times \{0\}\}$$

are the sides of the structure that meet at the origin of the coordinate system and are parallel to the $y-z, x-z, x-y$ planes respectively.

$$\Gamma_n = \{\{10^{-6}\} \times [0, 10^{-6}] \times [0, 10^{-6}]\} \cup \{[0, 10^{-6}] \times \{10^{-6}\} \times [0, 10^{-6}]\}$$

is the union of the sides opposite to Γ_x and Γ_y, and

$$\Gamma_I = \{[0, 10^{-6}] \times [0, 10^{-6}] \times \{z_{max}\}\}$$

is opposite to Γ_z, where $z_{max} = 10^{-6}$ for cases 1 and 4, and $z_{max} = 0.25 \times 10^{-6}$ for cases 2 and 3.
The solution parameters are given in Table 4.2. We determine the value for γ_E from

$$E_{\mathrm{Li_{15}Si_4}} = E_{\mathrm{Si}} + \gamma_E c_{max}$$

or

$$\gamma_E = \frac{E_{\mathrm{Li_{15}Si_4}} - E_{\mathrm{Si}}}{c_{max}} = -\frac{55}{88670} = -6.2 \times 10^{-4} \text{GPa m}^3/\text{mol} \tag{4.169}$$

Table 4.2: Parameters for Li_xSi

Symbol	Name	Value
D	Diffusion constant	2×10^{-16}m^2/s [30]
E_{Si}	Young's modulus for amorphous Si	80 GPa [5]
$E_{Li_{15}Si_4}$	Young's modulus for $Li_{15}Si_4$	25 GPa [6]
ν	Poisson's ratio	0.3
Ω	Partial molar volume	8.539×10^{-6}m^3/mol [8]
c_{max}	Maximum concentration in $Li_{15}Si_4$	8.867×10^4 mol/m^3 [8]
γ_E	Rate of change of Young's modulus	-6.2×10^{-4}GPa m^3/mol

We make note that we are using the same applied current density for both geometries. In reality, of course, one of the benefits of using smaller particles is that we have higher surface area and hence lower current density. However, in this case we want to accent specifically that even using the same currents, we still obtain much lower stresses and strains with the smaller particle.
Let us first look at the concentration for the four cases at the end of the charging process and at the end of the discharging process. In Figures 4.18–4.21 we give the concentration for the four test cases, cut along the $x = y$ line. Due to the slow diffusion (for comparison, it is about 40 times slower than the one used in Chapter 3) we can see that there are strong gradients in the concentration. Especially for cases 1 and 4 we see that at the end of the charging process, the concentration on the top of the particle is more than two times higher than the one on the bottom. Conversely, at the end of the discharge process, the top is almost empty, while in the bottom the concentration is still about $3.5 \times 10^4 mol/m^3$. For the other two test cases, the difference between top and bottom is much smaller at about $10^4 mol/m^3$. We also use these figures to study the shape and size of the lithiated silicon. The black box outline in the figures is the original structure, before we deposit any lithium ions. While the cases with the bigger particle show noticeable bending, the other two test cases give much more uniform expansion. And finally, let us look at the volumes obtained at the different stages. The volume expansion of the particle in test cases 1 and 4 is about 54-55% at the end of the charging process, while for the other two cases we have about 93% for both. We consider now how close these numbers are to the the volume expansion prescribed by equation (4.114). For test case 1 the volume at the end of the charging is $1.54373 \times 10^{-18} m^3$ and the number of lithium ions is $6.39407 \times 10^{-14} mol$. Using relation (4.114) we determine the predicted volume as $1.54599 \times 10^{-18} m^3$, which gives a ratio of about 0.998 of real to predicted volume. The corresponding such ratios for test cases 2, 3 and 4 are 0.999, 0.9995 and 1.00005 respectively. Conversely, at the end of

the discharge process we have ratios of about 0.999, 1.0017, 1.002 and 1.0005 for test cases 1, 2, 3 and 4. This suggests that both in charge and discharge the elastic strain is relatively small, compared to the chemical strains. On that note, let us now study more closely the Von Mises strains (4.49) and Von Mises stresses (4.48).

In Figure 4.22 we show the evolution of the signed Von Mises strain (where for the sign, we take the sign of the hydrostratic strain, which is the trace of the strain tensor) at the point on the top side of the particles, which initially has coordinates $\mathbf{p}_{VM} = (0, 0, 1 \times 10^{-6})$ for the big particle geometry and $\mathbf{p}_{VM} = (0, 0, 0.25 \times 10^{-6})$ for the small particle geometry. In subfigure 4.22a the Von Mises strain is given with respect to time and in subfigure 4.22b, it is given with respect to the state of charge. We observe that at this spot for all cases, the strains are compressive during charging and tensile during discharging. Also, for cases 2 and 3, the Von Mises strain reaches about 3% in both negative (compressive) and positive (tensile) values, and on this scale the strain is practically indistinguishable between the two models. For test cases 1 and 4 the negative values are almost 8%, but the positive are only about 5%. These values are potentially in the inadmissible region, since according to Boles et al. [6], the fully lithiated silicon behaves similar to the pure silicon in the sense that it admits only several percent of straining before fracture. Furthermore, we can observe in Figures 4.24–4.27 that actually the highest and lowest values are reached in the exact opposite corner of the geometry with respect to point $\mathbf{p}_{VM}$. While this has no effect on the maximum and minimum values of test cases 2 and 3, for test cases 1 and 4 we have even bigger values than before. The maximum tensile strain achieved is about 7.5% for both cases while the minimum compressive strain is about 9.1% for test case 1 and about 9.7% in test case 4. This means that there is about 0.6% difference between the two models. Observe also in these figures that the strains on the free surfaces are mostly of the opposite sign to those in the core (recall that the surfaces meeting at the origin are in fact representative of the core of the whole particle as explained in the beginning of the section).

Moving on to the Von Mises stress, similarly to before, we show in Figure 4.23 the evolution of the Von Mises stress at the point $\mathbf{p}_{VM}$ with respect to time and state of charge. In these figures we see a very similar behavior of the stress to the one obtained experimentally by Sethuraman et al. [84]. Namely, during charging the stress first decreases rapidly and then evens out and starts to increase slowly. Of course, this is only a qualitative comparison, since for a quantitative analysis, we would need much more data about the exact specimen used. Note that as can be observed from Figure 4.22, in the charging scenario, the strains never stop decreasing. This means that if we

do not take into account the softening of the material by considering a concentration dependent Young's modulus, we would not obtain this behavior for the stress. In [12] the researchers obtain similar soc-stress curves for a spherical particle, using a plasticity model in spherical coordinates, which is solved in 1D. In our simulations we test in a fully three dimensional setting using an elastic model. Bower et al. [10] show results that are in good agreement with [84], also with a model that couples plasticity. We show that even using only elasticity we can obtain similar curves to the ones from experimental data, when we take the Young's modulus to be concentration-dependent. It is clear that by not accounting for inelastic effects, we are in essence restricted to always predict the same curves regardless of how many times we cycle the battery after the first cycle. This can be seen by the curve for test case 2 in Figures 4.22b and 4.23b, where we see that on the second cycle, the black curve joins the curves from the first cycle and from there on out, they coincide. However, our simulations can be used as a basis for future expansion, including plasticity, fracture, damage, etc.

Let us now focus on the differences between the mechanical models we consider. From Figure 4.22 we already observed that the strains at the point $\mathbf{p}_{VM}$ are almost the same. From the spatial distribution of the strain we saw that for test cases 1 and 4 the maximum difference is about 0.6%. Again at the point $\mathbf{p}_{VM}$ we see about 80MPa maximum difference between test cases 2 and 3 but about 500MPa difference between cases 1 and 4. From the spatial distribution of the stress, given in Figures 4.28–4.31, we see that for test cases 1 and 4 the maximum difference grows to about 2GPa in the corner where also the maximum difference in strains was attained. However, as already mentioned the strains in this case indicate that other effects, like fracture, would have already taken effect at this point. For the small particle cases 2 and 3 the maximum difference of 80MPa is the same also in the spatial distributions. This indicates that for the values of strain, where it is realistic to expect to still have an elastic response, the difference between the two models can be neglected.

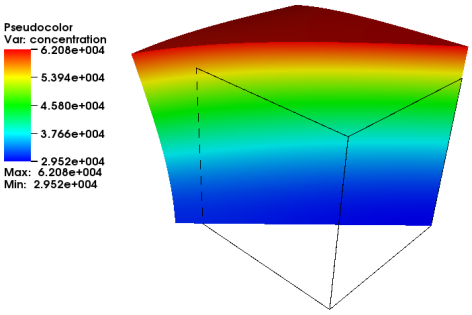

(a) At the end of charge process after 3856 seconds of simulation

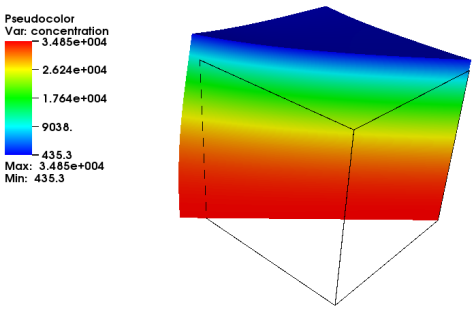

(b) At the end of discharge process after 5764 seconds of simulation

Figure 4.18: Lithium concentration ($\frac{mol}{m^3}$) for test case 1

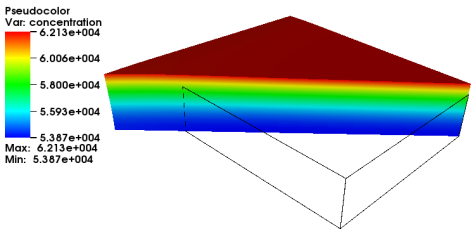

(a) At the end of charge process after 1652 seconds of simulation

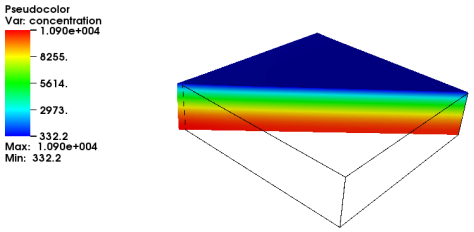

(b) At the end of discharge process after 3188 seconds of simulation

Figure 4.19: Lithium concentration ($\frac{mol}{m^3}$) for test case 2

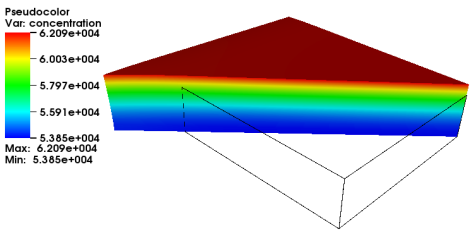

(a) At the end of charge process after 1652 seconds of simulation

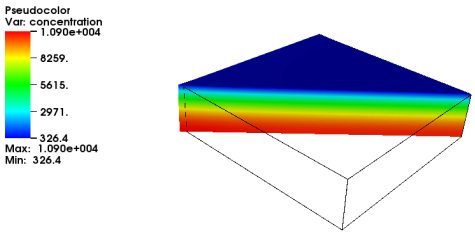

(b) At the end of discharge process after 3188 seconds of simulation

Figure 4.20: Lithium concentration ($\frac{mol}{m^3}$) for test case 3

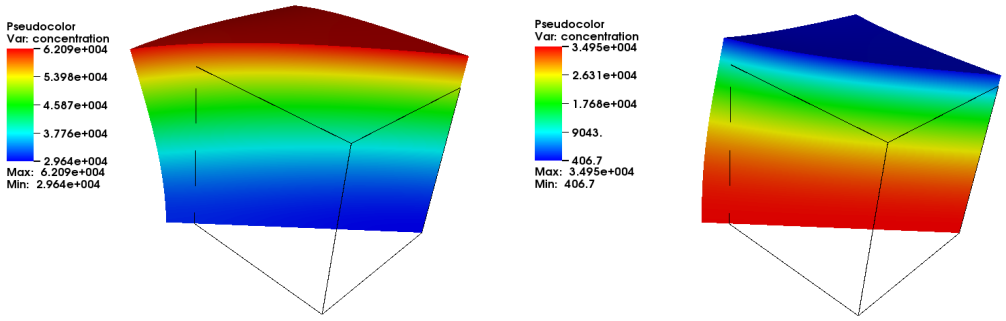

(a) At the end of charge process after 3884 seconds of simulation

(b) At the end of discharge process after 5812 seconds of simulation

Figure 4.21: Lithium concentration ($\frac{mol}{m^3}$) for test case 4

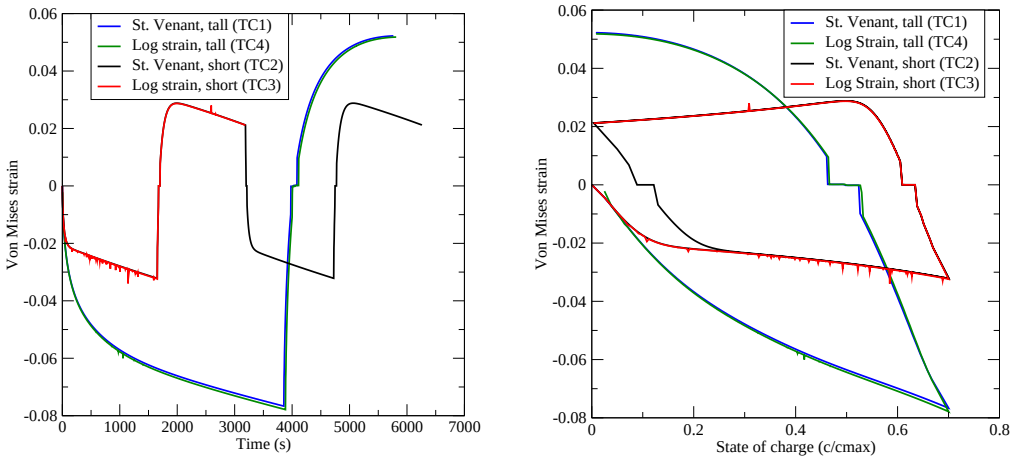

(a) versus time

(b) versus state of charge at point $\mathbf{p}_{VM}$

Figure 4.22: Von Mises strain at point $\mathbf{p}_{VM}$

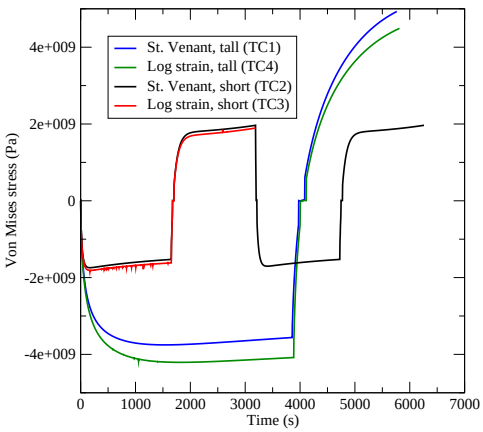

(a) versus time

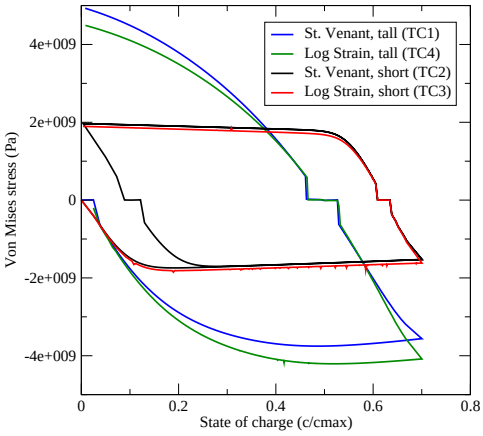

(b) versus state of charge at point $\mathbf{p}_{VM}$

Figure 4.23: Von Mises stress at point $\mathbf{p}_{VM}$

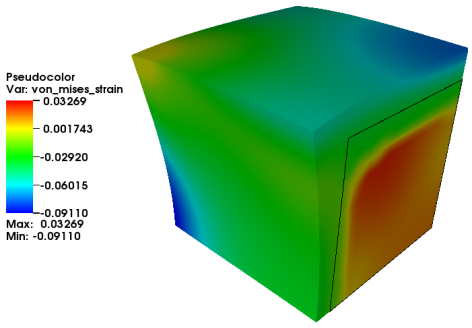

(a) At the end of charge process after 3856 seconds of simulation

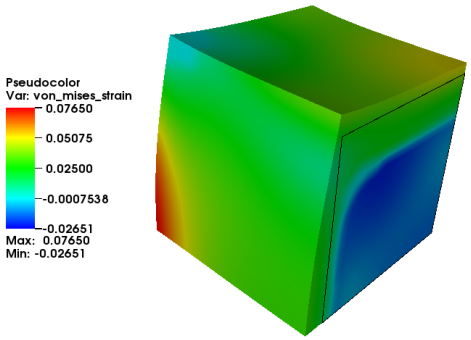

(b) At the end of discharge process after 5764 seconds of simulation

Figure 4.24: Von Mises strain for test case 1

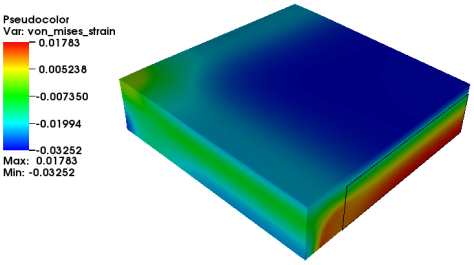

(a) At the end of charge process after 1652 seconds of simulation

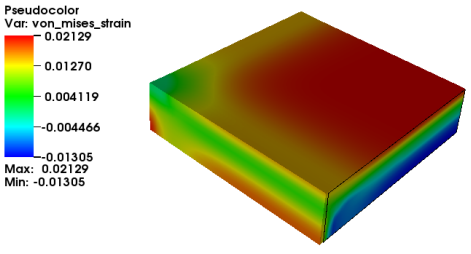

(b) At the end of discharge process after 3188 seconds of simulation

Figure 4.25: Von Mises strain for test case 2

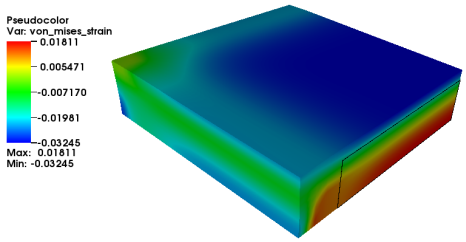

(a) At the end of charge process after 1652 seconds of simulation

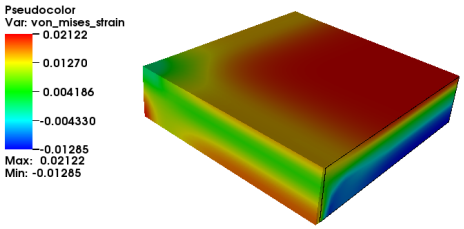

(b) At the end of discharge process after 3188 seconds of simulation

Figure 4.26: Von Mises strain for test case 3

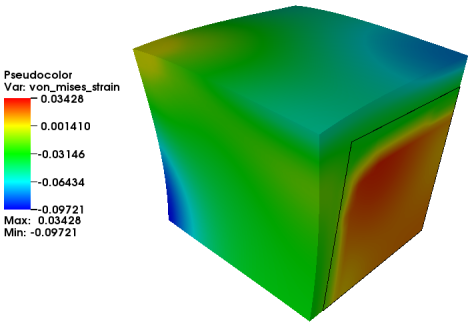

(a) At the end of charge process after 3884 seconds of simulation

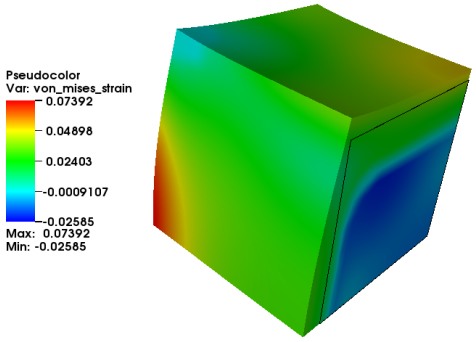

(b) At the end of discharge process after 5812 seconds of simulation

Figure 4.27: Von Mises strain for test case 4

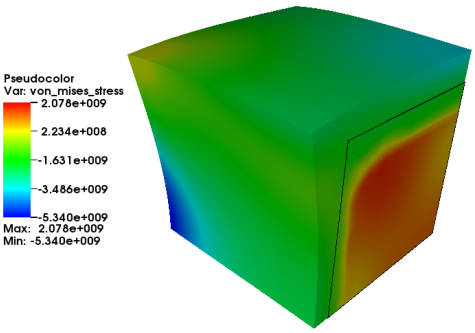

(a) At the end of charge process after 3856 seconds of simulation

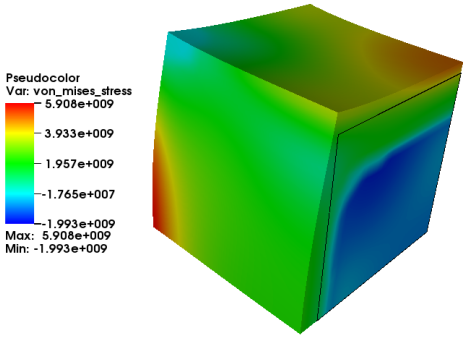

(b) At the end of discharge process after 5764 seconds of simulation

Figure 4.28: Von Mises stress (Pa) for test case 1

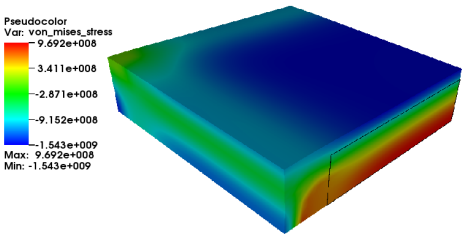

(a) At the end of charge process after 1652 seconds of simulation

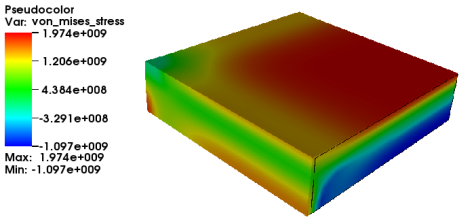

(b) At the end of discharge process after 3188 seconds of simulation

Figure 4.29: Von Mises stress (Pa) for test case 2

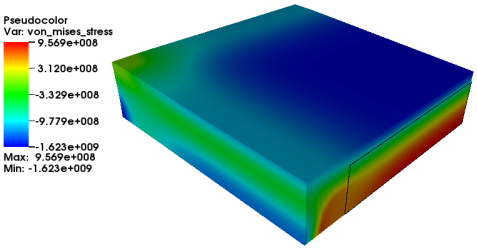

(a) At the end of charge process after 1652 seconds of simulation

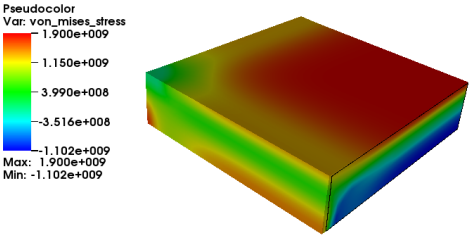

(b) At the end of discharge process after 3188 seconds of simulation

Figure 4.30: Von Mises stress (Pa) for test case 3

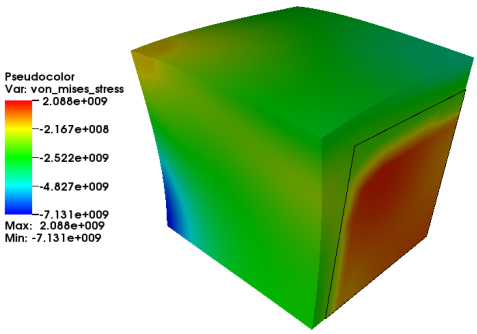

(a) At the end of charge process after 3884 seconds of simulation

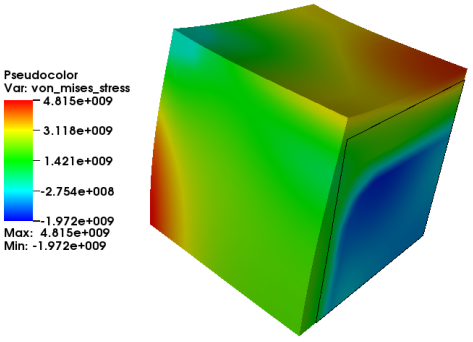

(b) At the end of discharge process after 5812 seconds of simulation

Figure 4.31: Von Mises stress (Pa) for test case 4

Chapter 5

Computer implementation and verification

In this chapter we give an overview of the design decisions and interfaces of the code we developed to run our simulations. We also dedicate a subsection to verification of the basic building blocks of our discretizations using known solutions.
Let us also mention here the external software that we use. For building the tetrahedal meshes, we used the Netgen mesh generator [83][82], version 5.3. For building the hexhedral meshes, we used either GeoDict[43] or our own code for the simpler meshes (the hexahedral meshes used in Chapter 4). For visualization, we used LLNL's VisIt software tool [21][66], version 2.7.1. The code was compiled using GCC4.8.1 [39].

5.1 Code overview

This section is meant to give only a brief overview of the design of the code and not go into specific details like function names. In that sense we also do not explain computer architecture or programming topics and assume some familiarity of the subject. For information on the C++ language, see [89], on the C++ object model, see [64] and about computer architectures, see [87]. We also present only the underlying FEM framework and not the implemented discretizations of the various problems.
Our target for the code was to give flexibility with respect to the usage of the different structures of the program. The motivation is that, since this is a scientific application, one might want to e.g. choose a different linear solver, or use the matrix structures, but use different discretization, etc. In that sense, for this application we preferred to use object composition as much as

possible rather than complex hierarchies, that can often restrict the extensibility of the code. The code is standard-compliant C++11 and is portable to all compilers that support the C++11 standard [49].
Let us first describe the discretization structures. We have three main building blocks in the discretization - elements, surfaces and points. We briefly explain each of the classes without going into detail describing all of their member functions and applications. The *point_t* structure contains the data about a single point. We keep the coordinates and the boundary condition of the point. However, due to the specifics of the application with regards to splitting the nodes on the interface, the structure also provides a possibility to store information about a potential double node. This can be also exploited if solving problems with periodic boundary conditions where one can provide the link between two periodic nodes.
For the *element_t* and $surface\_t$ structures, we wanted to provide the option of mixing different types of elements and consequently surfaces in the same mesh. This would usually be accomplished using an abstract base class, which is then inherited in classes representing specific element types. It is then used by declaring a pointer of the base class and specifying the concrete type when creating the object. However, even if one uses a smart pointer for the base class, so as to prevent memory leaks, we still have to deal with pointer semantics when handling variables of such type. We instead follow an approach proposed by Sean Parent [71] that rather leads to value semantics, i.e. one can copy and move the object as if it were a regular class. In this approach, the abstraction is hidden in a helper class and one does not need to inherit explicitly a base class, but just respect its interface. Our classes are also move-enabled as per the C++11 standard and if one wants to move the object rather than copy it, only the internal pointer is moved. For the elements, we provide functions for computing the shape functions, their derivatives with respect to both the reference coordinates and the real coordinates, the Jacobian of the transformation and other quantities at points on the reference domain. Using these functions, however, is useful only for fast prototyping, since this approach is inefficient both from algorithmic and from computing perspectives. From algorithmic side we have that many of the computations need to be repeated for multiple quantities, e.g. the Jacobi matrix is needed both for the derivatives with respect to the real coordinates and for computing the Jacobian, the shape functions are needed also for the transformation from reference to current coordinates, etc. From computing side we still need to consider that there is a virtual call that needs to be resolved at runtime rather than at compile time. Due to this dynamic binding, the compiler cannot inline any function calls to the member functions of the elements. This means that there is a function call that always needs to be

performed. For these reasons we provide two options for bulk computations of all quantities in an element. The first option is to compute everything at a single point in the reference domain. However, this can potentially still be ineffective since for certain elements, like P1 triangles and tetrahedra, the transformation matrices and the derivatives of the shape functions are constant in the whole element. Thus, the second option is to compute all the quantities in all the points required for a certain accuracy of numerical integration and put them in a special structure, where the accuracy is a parameter passed by the user. This has several benefits. Namely, there is only one function call per element, the redundant multiple computations of the same quantities are omitted, and since the data needed for the computation is relatively small it can fit in the Level 1 cache of the CPU, so there are not multiple transfers between main memory and the cache structures.
The *element_t*, $surface\_t$ and *point_t* structures are wrapped in the class *element_space_t*. We use it to manage the arrays of elements, surfaces and points. Mostly it acts as a thin wrapper around vectors of the three basic classes. However, the points in the elements and surfaces are given through pointers. If one wants to resize the points structure (e.g. for mesh refinement), all pointers in the elements and surfaces to the points would be invalidated. This class provides functions for resizing the internal vectors without such invalidation.
The final class associated with the discretization, that we describe here, is the solution description class. As we mentioned in Chapter 4, this class is useful when one has to match multiple solutions, possibly defined in different parts of the region. It is also useful if one does not want to manage the numbering of the degrees of freedom for the discretization of a system of PDEs. Furthermore it provides the option to specify if a certain solution is vector or scalar. We use this class in all of the discretized problems we consider, but it is most useful in the coupled problem between the full electrochemical model and the small strain elasticity, c.f. Section 4.2. The electrochemical quantities concentration and potential are defined in the whole domain, but the displacement is defined only in the electrodes.
We store the global matrices in Compressed Sparse Row format [79], where the matrix is described by three arrays. The first array stores row pointers, the second stores column indeces and the third stores the values of the elements of the matrix. The row pointers indicate where each row starts in the other two arrays. The column indeces and the values have the same size - the number of non-zero elements in the matrix. In the program, the positions (i.e. the row pointers and the column indeces vectors) of the non-zero elements are decoupled in a separate structure from the whole matrix. We do this in order to be able to potentially reuse the pattern in multiple

matrices without having to store it every time. We also provide functions for reading the mesh files (in Netgen and BEST formats), building the structure of the sparse matrices and for exporting the results in vtk files, but we do not present them in detail here.

5.2 Verification

In this section we give verification of the code by solving a simple problem. Namely, we solve the problem from Chapter 2 in the unit cube. We use a constant diffusion coefficient $D(x)$ and linear Neumann boundary condition $b(x)$. We use manufactured solutions, where we can calculate the L_2 norm of the error. The problem is solved using both tetrahedral and hexahedral elements, since they are the ones we use for solving the physical models presented in the thesis. To test the spatial discretization, we solve a stationary problem and to test the full discretization, we solve a time dependent problem. The first problem is

$$-\Delta u = f(\mathbf{x}), \quad \mathbf{x} \in \{[0,1] \times [0,1] \times [0,1]\} \tag{5.1}$$

$$-\nabla u \cdot \mathbf{n} = b(x), \quad \mathbf{x} \in \Gamma_N \tag{5.2}$$

$$u(\mathbf{x}) = u_D(\mathbf{x}), \quad \mathbf{x} \in \Gamma_D \tag{5.3}$$

where u_D are just the values of the known function on the boundary. Γ_N is the union of the two sides of the cube, where $\mathbf{x} \in \{\{0\} \times [0,1] \times [0,1]\}$ and $\mathbf{x} \in \{\{1\} \times [0,1] \times [0,1]\}$. We use three tetrahedral meshes and three hexahedral meshes to test the convergence rate. The tetrahedal meshes are

1. 6823 elements and 1534 points
2. 50852 elements and 10148 points
3. 418052 elements and 77378 points

and the hexahedral are

1. 1000 elements and 1331 points
2. 8000 elements and 9261 points
3. 64000 elements and 68921 points

As we already pointed out in Chapter 2 if a function u is an element of the finite space then $||u - u_h|| = 0$ in both the L_2 and H^1 norms. In that sense,

the first manufactured solutions we test with are

$$u_1(x_1, x_2, x_3) = 1 + x_1 + x_2 + x_3 \tag{5.4}$$
$$f(x_1, x_2, x_3) = 0 \tag{5.5}$$
$$b(x_1, x_2, x_3) = \begin{pmatrix} 1 \\ 1 \\ 1 \end{pmatrix} \cdot \mathbf{n} \tag{5.6}$$

for the tetrahedral elements and

$$u_2(x_1, x_2, x_3) = 1 + x_1 + x_2 + x_3 + x_1x_2 + x_1x_3 + x_2x_3 + x_1x_2x_3 \tag{5.7}$$
$$f(x_1, x_2, x_3) = 0 \tag{5.8}$$
$$b(x_1, x_2, x_3) = \begin{pmatrix} 1 + x_2 + x_3 + x_2x_3 \\ 1 + x_1 + x_3 + x_1x_3 \\ 1 + x_1 + x_2 + x_1x_2 \end{pmatrix} \cdot \mathbf{n} \tag{5.9}$$

for the hexahedral elements. For u_1 using tetrahedal elements we obtain an L_2 norm of $||u-u_h||_{L_2(\Omega)} = 1.78 \times 10^{-13}$ and an H^1 norm $||u-u_h||_{H^1(\Omega)} = 2.65 \times 10^{-12}$. For u_2 and hexhedral elements we have $||u - u_h||_{L_2(\Omega)} = 2.45 \times 10^{-13}$ and $||u - u_h||_{H^1(\Omega)} = 1.72 \times 10^{-12}$. The final stationary problem we consider is

$$u_3(x_1, x_2, x_3) = x_1^2 + x_2^2 - x_3^2 \tag{5.10}$$
$$f(x_1, x_2, x_3) = -2 \tag{5.11}$$
$$b(x_1, x_2, x_3) = \begin{pmatrix} 2x_1 \\ 2x_2 \\ 2x_3 \end{pmatrix} \cdot \mathbf{n} \tag{5.12}$$

The norms are given in Table 5.1

Table 5.1: L_2 and H^1 error norms for problem (5.10)

Tetrahedral Mesh	$\|\|u - u_h\|\|_{L_2} \times 10^4$	rate	$\|\|u - u_h\|\|_{H^1} \times 10^2$	rate
h	14.62	-	9.884	-
$h/2$	3.687	1.99	4.999	0.98
$h/4$	0.866	2.09	2.488	1.01
Hexahedral Mesh	$\|\|u - u_h\|\|_{L_2} \times 10^4$	rate	$\|\|u - u_h\|\|_{H^1} \times 10^2$	rate
h	16.666	-	10	-
$h/2$	4.167	2	5	1
$h/4$	1.042	2	2.5	1

As one can observe, the convergence rates are consistent with the expected results, namely for u_1 and u_2, the FEM solutions are exact within machine accuracy and for u_3 we obtain second order convergence in the L_2 norm and first order in H^1 for both tetrahedal and hexahedral elements.
Finally, let us also show a single test case for the time dependent diffusion equation

$$u_4(x_1, x_2, x_3, t) = t^2 x_1 x_2 + x_3^2 - x_2^2 x_3 \tag{5.13}$$
$$u_t - \Delta u = 2t x_1 x_2 + 2x_3 - 2 \tag{5.14}$$
$$\nabla u \cdot \mathbf{n} = \begin{pmatrix} t^2 x_2 \\ t^2 x_1 - 2x_2 x_3 \\ 2x_3 - x_2^2 \end{pmatrix} \cdot \mathbf{n}, \quad \mathbf{x} \in \Gamma_N \tag{5.15}$$
$$u(x_1, x_2, x_3, t) = u_4(x_1, x_2, x_3, t), \quad \mathbf{x} \in \Gamma_D \tag{5.16}$$
$$u(x_1, x_2, x_3, 0) = u_4(x_1, x_2, x_3, 0), \quad \mathbf{x} \in \bar{\Omega} \tag{5.17}$$

We give the L_2 and H^1 norm for consistent mass and lumped mass approaches, using only hexahedral elements when $t = 4$. The results are given in Table 5.2

Table 5.2: L_2 and H^1 error norms for problem (5.13) at $t = 4$ using hexahedral elements. u_{ch} is the solution with consistent mass matrix and u_{lh} is the solution with lumped mass

mesh size	Δt	$\|\|u - u_{ch}\|\|_{L_2} \times 10^3$	rate	$\|\|u - u_{lh}\|\|_{L_2} \times 10^3$	rate
h	1	11.85	-	11.695	-
$h/2$	0.25	2.983	2	2.941	2
$h/4$	0.0625	0.7471	2	0.7365	2
mesh size	Δt	$\|\|u - u_{ch}\|\|_{H^1} \times 10^2$	rate	$\|\|u - u_{lh}\|\|_{H^1} \times 10^2$	rate
h	1	8.677	-	8.606	-
$h/2$	0.5	4.348	1	4.328	1
$h/4$	0.25	2.175	1	2.17	1

The error is of order $O(\Delta t + h^2)$ for the L_2 norm and $O(\Delta t + h)$ for the H^1 norm for both the consistent mass and the lumped mass approaches.

Chapter 6

Summary

In this work we studied degradation phenomena in lithium-ion batteries, related to intercalation of lithium ions on the microscale. We investigated the following topics:

- Solution of three-dimensional isothermal [59] and non-isothermal [58] electrochemical models on spatially resolved porous microstructures
- Comparison between the finite element method (FEM) and the voxel-based cell centered finite volume method (FVM) to study the dependence of the solution of the isothermal electrochemical model [59] on the discretization method
- Analysis of the spatial data from the electrochemical simulations to identify possible hotspots in the battery
- Derivation of an ODE form of the energy balance equation from the non-isothermal model
- Application of a certain single phase small strain model [105] to observe the generation of mechanical stress from the diffusion of lithium ions and its influence on said diffusion
- Coupling of the single phase small strain model [105] to the isothermal electrochemical model [59] and numerical investigation of the resulting model for cylindrical particles
- Study of the behavior of the stress using large strain elastic models with concentration-dependent Young's modulus
- Identification of an appropriate elastic finite strain model for Silicon electrodes that expand up to several hundred percent

We successfully discretized and numerically solved the isothermal [59] and non-isothermal [58] electrochemical models (Chapter 3). This allowed us to analyze where the individual heat sources exhibit exceptional behavior. We further observed that even though we simulated the heat equation on spatially resolved electrodes, for the investigated cases the temperature was increasing as a macroscopic quantity. This allowed us to decrease the computational effort for the heat equation by reformulating it as an ODE and removing the necessity of solving an algebraic system of equations (Section 3.3). For the isothermal model, we also compared FEM to the voxel-based FVM for small electrodes with several spherical particles. We observed that due to the voxelization of the geometry and the absence of values on the interface, the FVM underestimates the cell voltage of the battery. Also, the concentration distribution on the surface of the spherical particles had variations in the FVM, in places where the FEM gave uniform values.
For the small strain model [105] (Section 4.2) we observed that even for single particle configurations, depending on the boundary conditions, the convective term in the concentration equation can influence negatively the uniformity of the concentration. We also successfully coupled the full electrochemical model to the small strain equilibrium equation and solved the resulting system. For our test case we observed that the hydrostatic stress, which includes a concentration-dependent term, was indeed influenced by the different distribution of the concentration. However, the Von Mises stress, which depends on the deviatoric stress tensor and hence does not include the concentration explicitly, was mostly influenced by the boundary condition of fixed displacement on the current collector.
Finally, for the finite strain case (Section 4.3) we compared two elastic models to study the sensitivity of the results on the specific model used. We observed that for realistic values of mechanical strain, the two models give close results. Note that, while we do not include here inelastic effects, many models that do include them still rely on identifying the range of the elastic regime. In that sense, choosing an appropriate elastic model can be just as important as the inelastic model used, as an incorrect prediction of the mechanical stress and strain can cause overestimation or underestimation of the respective inelastic effects. We also observed that when we account for the softening of the material as it undergoes lithiation, we managed to reproduce the general behavior of specific experimental results [84].
As future extensions of this work, one could investigate the influence of the temperature on the degradation of the materials. Also, the inelastic effects observed in practice, like fracture, could be included. Other models for the electrochemical transport in the particles and in the electrolyte can be used for materials where it makes sense.

Appendix A

Element types

We show briefly in this chapter the various elements we use, their shape functions and their transformation matrices. For the volumetric elements we show also the derivatives of the shape functions. For the tetrahedral element we also give the Jacobi matrix, since it is constant.

A.1 Volume elements

A.1.1 Tetrahedron element

Shape functions

$$\varphi_1(\xi_1, \xi_2, \xi_3) = \xi_1 \tag{A.1}$$
$$\varphi_2(\xi_1, \xi_2, \xi_3) = \xi_2 \tag{A.2}$$
$$\varphi_3(\xi_1, \xi_2, \xi_3) = \xi_3 \tag{A.3}$$
$$\varphi_4(\xi_1, \xi_2, \xi_3) = 1 - \xi_1 - \xi_2 - \xi_3 \tag{A.4}$$

Derivatives

$$\nabla\varphi_1(\xi_1, \xi_2, \xi_3) = (1, 0, 0)^T \tag{A.5}$$
$$\nabla\varphi_2(\xi_1, \xi_2, \xi_3) = (0, 1, 0)^T \tag{A.6}$$
$$\nabla\varphi_3(\xi_1, \xi_2, \xi_3) = (0, 0, 1)^T \tag{A.7}$$
$$\nabla\varphi_4(\xi_1, \xi_2, \xi_3) = (-1, -1, -1)^T \tag{A.8}$$

The Jacobi matrix is

$$\mathbf{J} = \begin{pmatrix} x_1 - x_4 & x_2 - x_4 & x_3 - x_4 \\ y_1 - y_4 & y_2 - y_4 & y_3 - y_4 \\ z_1 - z_4 & z_2 - z_4 & z_3 - z_4 \end{pmatrix} \tag{A.9}$$

Note that for this element the derivatives and consequently the Jacobi matrix and the Jacobian are constant.

A.1.2 Hexahedron element

Shape functions

$$\varphi_1(\xi_1,\xi_2,\xi_3) = \frac{1}{8}(1-\xi_1)(1-\xi_2)(1-\xi_3)$$
$$\varphi_2(\xi_1,\xi_2,\xi_3) = \frac{1}{8}(1+\xi_1)(1-\xi_2)(1-\xi_3)$$
$$\varphi_3(\xi_1,\xi_2,\xi_3) = \frac{1}{8}(1-\xi_1)(1+\xi_2)(1-\xi_3)$$
$$\varphi_4(\xi_1,\xi_2,\xi_3) = \frac{1}{8}(1+\xi_1)(1+\xi_2)(1-\xi_3)$$
$$\varphi_5(\xi_1,\xi_2,\xi_3) = \frac{1}{8}(1-\xi_1)(1-\xi_2)(1+\xi_3)$$
$$\varphi_6(\xi_1,\xi_2,\xi_3) = \frac{1}{8}(1+\xi_1)(1-\xi_2)(1+\xi_3)$$
$$\varphi_7(\xi_1,\xi_2,\xi_3) = \frac{1}{8}(1-\xi_1)(1+\xi_2)(1+\xi_3)$$
$$\varphi_8(\xi_1,\xi_2,\xi_3) = \frac{1}{8}(1+\xi_1)(1+\xi_2)(1+\xi_3)$$

Derivatives

$$\nabla\varphi_1(\xi_1,\xi_2,\xi_3) = \frac{1}{8}\left(-(1-\xi_2)(1-\xi_3), -(1-\xi_1)(1-\xi_3), -(1-\xi_1)(1-\xi_2)\right)^T$$
$$\nabla\varphi_2(\xi_1,\xi_2,\xi_3) = \frac{1}{8}\left((1-\xi_2)(1-\xi_3), -(1+\xi_1)(1-\xi_3), -(1+\xi_1)(1-\xi_2)\right)^T$$
$$\nabla\varphi_3(\xi_1,\xi_2,\xi_3) = \frac{1}{8}\left(-(1+\xi_2)(1-\xi_3), (1-\xi_1)(1-\xi_3), -(1-\xi_1)(1+\xi_2)\right)^T$$
$$\nabla\varphi_4(\xi_1,\xi_2,\xi_3) = \frac{1}{8}\left((1+\xi_2)(1-\xi_3), (1+\xi_1)(1-\xi_3), -(1+\xi_1)(1+\xi_2)\right)^T$$
$$\nabla\varphi_5(\xi_1,\xi_2,\xi_3) = \frac{1}{8}\left(-(1-\xi_2)(1+\xi_3), -(1-\xi_1)(1+\xi_3), (1-\xi_1)(1-\xi_2)\right)^T$$
$$\nabla\varphi_6(\xi_1,\xi_2,\xi_3) = \frac{1}{8}\left((1-\xi_2)(1+\xi_3), -(1+\xi_1)(1+\xi_3), (1+\xi_1)(1-\xi_2)\right)^T$$
$$\nabla\varphi_7(\xi_1,\xi_2,\xi_3) = \frac{1}{8}\left(-(1+\xi_2)(1+\xi_3), (1-\xi_1)(1+\xi_3), (1-\xi_1)(1+\xi_2)\right)^T$$
$$\nabla\varphi_8(\xi_1,\xi_2,\xi_3) = \frac{1}{8}\left((1+\xi_2)(1+\xi_3), (1+\xi_1)(1+\xi_3), (1+\xi_1)(1+\xi_2)\right)^T$$

A.2 Surface elements

The transformation from reference to current coordinates is

$$x_1 = \sum_{j=1}^{n} x_{1j}\varphi_j(\xi_1, \xi_2)$$
$$x_2 = \sum_{j=1}^{n} x_{2j}\varphi_j(\xi_1, \xi_2)$$
$$x_3 = \sum_{j=1}^{n} x_{3j}\varphi_j(\xi_1, \xi_2)$$

where n is the number of shape functions

A.2.1 Triangle element

Shape functions

$$\varphi_1(\xi_1, \xi_2) = \xi_1 \tag{A.10}$$
$$\varphi_2(\xi_1, \xi_2) = \xi_2 \tag{A.11}$$
$$\varphi_3(\xi_1, \xi_2) = 1 - \xi_1 - \xi_2 \tag{A.12}$$

Derivatives

$$\nabla\varphi_1(\xi_1, \xi_2) = (1, 0)^T \tag{A.13}$$
$$\nabla\varphi_2(\xi_1, \xi_2) = (0, 1)^T \tag{A.14}$$
$$\nabla\varphi_3(\xi_1, \xi_2) = (-1, -1)^T \tag{A.15}$$

A.2.2 Rectangle element

Shape functions

$$\varphi_1(\xi_1, \xi_2) = \frac{1}{4}(1 - \xi_1)(1 - \xi_2)$$
$$\varphi_2(\xi_1, \xi_2) = \frac{1}{4}(1 + \xi_1)(1 - \xi_2)$$
$$\varphi_3(\xi_1, \xi_2) = \frac{1}{4}(1 - \xi_1)(1 + \xi_2)$$
$$\varphi_4(\xi_1, \xi_2) = \frac{1}{4}(1 + \xi_1)(1 + \xi_2)$$

Derivatives

$$\nabla\varphi_1(\xi_1,\xi_2) = \frac{1}{4}(-(1-\xi_2),-(1-\xi_1))^T$$
$$\nabla\varphi_2(\xi_1,\xi_2) = \frac{1}{4}((1-\xi_2),-(1+\xi_1))^T$$
$$\nabla\varphi_3(\xi_1,\xi_2) = \frac{1}{4}(-(1+\xi_2),(1-\xi_1))^T$$
$$\nabla\varphi_4(\xi_1,\xi_2) = \frac{1}{4}((1+\xi_2),(1+\xi_1))^T$$

Bibliography

[1] Peter Atkins and Julio de Paula. *Physical Chemistry*. W. H. Freeman, 9th edition, 2009.

[2] Doron Aurbach, Ella Zinigrad, Yaron Cohen, and Hanan Teller. A short review of failure mechanisms of lithium metal and lithiated graphite anodes in liquid electrolyte solutions. *Solid State Ionics*, 148(3–4):405–416, 2002. Proceedings of the Symposium on Materials for Advanced Batteries and Fuel Cells. Organised in conjunction with the International Conference on Materials for Advanced Technologies (ICMAT 2001).

[3] Klaus-Jürgen Bathe. *Finite Element Procedures*. Prentice-Hall, Inc., 1996.

[4] L. Y. Beaulieu, K. W. Eberman, R. L. Turner, L. J. Krause, and J. R. Dahn. Colossal reversible volume changes in lithium alloys. *Electrochem. Solid-State Lett.*, 4(9):A137–A140, 2001.

[5] Tanmay K. Bhandakkar and Huajian Gao. Cohesive modeling of crack nucleation under diffusion induced stresses in a thin strip: Implications on the critical size for flaw tolerant battery electrodes. *International Journal of Solids and Structures*, 47(10):1424 – 1434, 2010.

[6] Steven T. Boles, Carl V. Thompson, Oliver Kraft, and Reiner Mönig. In situ tensile and creep testing of lithiated silicon nanowires. *Applied Physics Letters*, 103(26):–, 2013.

[7] Javier Bonet and Richard Wood. *Nonlinear Continuum Mechanics for Finite Element Analysis*. Cambridge University Press, 2nd edition, 2009.

[8] B. A. Boukamp, G. C. Lesh, and R. A. Huggins. All–solid lithium electrodes with mixed–conductor matrix. *J. Electrochem. Soc.*, 128(4):725 – 729, 1981.

[9] A F Bower and P R Guduru. A simple finite element model of diffusion, finite deformation, plasticity and fracture in lithium ion insertion electrode materials. *Modelling and Simulation in Materials Science and Engineering*, 20(4):045004, 2012.

[10] A.F. Bower, P.R. Guduru, and V.A. Sethuraman. A finite strain model of stress, diffusion, plastic flow, and electrochemical reactions in a lithium-ion half-cell. *Journal of the Mechanics and Physics of Solids*, 59(4):804–828, 2011.

[11] Jan H. Brandts, Sergey Korotov, and Michal Kíek. The discrete maximum principle for linear simplicial finite element approximations of a reaction–diffusion problem. *Linear Algebra and its Applications*, 429(10):2344–2357, 2008. Special Issue in honor of Richard S. Varga.

[12] Laurence Brassart, Kejie Zhao, and Zhigang Suo. Cyclic plasticity and shakedown in high-capacity electrodes of lithium-ion batteries. *International Journal of Solids and Structures*, 50(78):1120 – 1129, 2013.

[13] Susanne C. Brenner and L. Ridgway Scott. *The Mathematical Theory of Finite Element Methods*. Springer, 3rd edition, 2008.

[14] M. Broussely, Ph. Biensan, F. Bonhomme, Ph. Blanchard, S. Herreyre, K. Nechev, and R.J. Staniewicz. Main aging mechanisms in li ion batteries. *Journal of Power Sources*, 146(1-2):90 – 96, 2005. Selected papers pressented at the 12th International Meeting on Lithium Batteries.

[15] CD-adapco. Battery design studio. `http://www.cd-adapco.com/`.

[16] P. Chatzipantelidis, R. D. Lazarov, and V. Thomée. Some error estimates for the lumped mass finite element method for a parabolic problem. *Mathematics of Computation*, 81:1–20, 2012.

[17] C. M. Chen and V. Thome. The lumped mass finite element method for a parabolic problem. *The Journal of the Australian Mathematical Society. Series B. Applied Mathematics*, 26:329–354, 1 1985.

[18] Yufei Chen and J.W. Evans. Heat transfer phenomena in lithium/polymer-electrolyte batteries for electric vehicle application. *Journal of the Electrochemical Society*, 140:7, 1993.

[19] Yufei Chen and J.W. Evans. Three-dimensional thermal modeling of lithium-polymer batteries under galvanostatic discharge and dynamic power profile. *Journal of the Electrochemical Society*, 141:11, 1994.

[20] Zhangxin Chen. *Finite Element Methods and Their Applications*. Springer, 2005.

[21] Hank Childs, Eric Brugger, Brad Whitlock, Jeremy Meredith, Sean Ahern, David Pugmire, Kathleen Biagas, Mark Miller, Cyrus Harrison, Gunther H. Weber, Hari Krishnan, Thomas Fogal, Allen Sanderson, Christoph Garth, E. Wes Bethel, David Camp, Oliver Rübel, Marc Durant, Jean M. Favre, and Paul Navrátil. VisIt: An End-User Tool For Visualizing and Analyzing Very Large Data. In *High Performance Visualization–Enabling Extreme-Scale Scientific Insight*, pages 357–372. Chapman and Hall/CRC, Oct 2012.

[22] John Christensen and John Newman. Stress generation and fracture in lithium insertion materials. *Journal of Solid State Electrochemistry*, 10(5):293–319, 2006.

[23] Philippe Ciarlet. Discrete maximum principle for finite-difference operators. *aequationes mathematicae*, 4(3):338–352, 1970.

[24] Philippe Ciarlet. *Mathematical Elasticity I: Three-Dimensional Elasticity*, volume 20 of *Studies in Mathematics and Its Applications*. Elsevier Science Publishers, 1988.

[25] CNN. Fire aboard empty 787 dreamliner prompts investigation. `http://edition.cnn.com/2013/01/07/travel/dreamliner-fire/index.html`, January 2013. Accessed: 2015-01-15.

[26] G. R. Cowper. Gaussian quadrature formulas for triangles. *International Journal for Numerical Methods in Engineering*, 7(3):405–408, 1973.

[27] CPSC. Sony recalls notebook computer batteries due to previous fires. `http://www.cpsc.gov/en/Recalls/2007/Sony-Recalls-Notebook-Computer-Batteries-Due-to-Previous-Fires/`, October 2006. Accessed: 2015-01-15.

[28] Christopher M. DeLuca, Kurt Maute, and Martin L. Dunn. Effects of electrode particle morphology on stress generation in silicon during lithium insertion. *Journal of Power Sources*, 196(22):9672–9681, 2011.

[29] Peter Deuflhard. *Iterative Solution of Nonlinear Equations in Several Variables*. Springer, 2004.

[30] N. Ding, J. Xu, Y.X. Yao, G. Wegner, X. Fang, C.H. Chen, and I. Lieberwirth. Determination of the diffusion coefficient of lithium ions in nano-si. *Solid State Ionics*, 180(23):222 – 225, 2009.

[31] Marc Doyle, Thomas F. Fuller, and John Newman. Modeling of galvanostatic charge and discharge of the lithium/polymer/insertion cell. *J. Electrochem. Soc.*, 140(6):1526–1533, 1993.

[32] Andrei Draganescu, Todd Dupont, and L. Ridgway Scott. Failure of the discrete maximum principle for an elliptic finite element problem. *Mathematics of Computation*, 74:1–23, 2005.

[33] Wolfgang Dreyer, Clemens Guhlke, and Michael Herrmann. Hysteresis and phase transition in many-particle storage systems. *Continuum Mech. Thermodyn.*, 23(3):211–231, 2011.

[34] Wolfgang Dreyer, Clemens Guhlke, and Rudiger Muller. Overcoming the shortcomings of the nernst-planck model. *Phys. Chem. Chem. Phys.*, 15:7075–7086, 2013.

[35] Yalchin Efendiev, Oleg Iliev, and Vasilena Taralova. Upscaling of an isothermal li-ion battery model via the homogenization theory. *Berichte des Fraunhofer ITWM, Nr. 230*, 2013.

[36] C.M. Elliot, D.A. French, and F.A. Milner. A second order splitting method for the cahn-hilliard equation. *Numer. Math.*, 54:575–590, 1989.

[37] Lawrence C. Evans. *Partial Differential Equations*. American Mathematical Society, 1998.

[38] I. Faragó, R. Horváth, and S. Korotov. Discrete maximum principle for linear parabolic problems solved on hybrid meshes. *Applied Numerical Mathematics*, 53(2–4):249–264, 2005. Tenth Seminar on Numerical Solution of Differential and Differntial-Algebraic Euqations (NUMDIFF-10).

[39] Free Software Foundation. GNU Compiler Collection. `https://gcc.gnu.org/`.

[40] T.F. Fuller, M. Doyle, and J. Newman. Simulation and optimization of the dual lithium ion insertion cell. *J. Electrochem. Soc.*, 141(1):1–10, 1994.

[41] R. Edwin García, Yet-Ming Chang, W. Craig Carter, Pimpa Limthongkul, and Catherine Bishop. Microstructural modeling and design of rechargable lithium-ion batteries. *J. Electrochem. Soc.*, 152(1):A255–A263, 2005.

[42] William C. Gear. *Numerical Initial Value Problems in Ordinary Differential Equations*. Prentice-Hall Inc., 1971.

[43] Math2Market GmbH. Geodict. `http://www.geodict.com/`.

[44] H. Frank Gibbard. Thermal Properties of Battery Systems. *Journal of The Electrochemical Society*, 125(3):353–358, 1978.

[45] P. C. Hammer, O. J. Marlowe, and A. H. Stroud. Numerical integration over simplexes and cones. *Math. Comp.*, 10(55):130–137, 1956.

[46] Stephen J. Harris, Adam Timmons, Daniel R. Baker, and Charles Monroe. Direct in situ measurements of li transport in li-ion battery negative electrodes. *Chemical Physics Letters*, 485(4–6):265–274, 2010.

[47] Jeong Hun, Myoungdo Chung, Myounggu Park, Sang Woo, Xiangchun Zhang, and Ann Marie Sastry. Generation of realistic particle structures and simulations of internal stress: A numerical/AFM study of LiMn2O4 particles. *Journal of The Electrochemical Society*, 158(4):A434–A442, 2011.

[48] COMSOL Inc. Comsol multiphysics. `http://www.comsol.com/`.

[49] ISO/IEC 14882:2011. *Information technology – Programming languages – C++*. ISO, Geneva, Switzerland, 2011.

[50] Fraunhofer ITWM. BEST – Battery and Electrochemistry Modeling. `http://www.itwm.fraunhofer.de/best`.

[51] Rudolph G. Jungst, Ganesan Nagasubramanian, Chris C. Crafts, David Ingersoll, and Daniel H. Doughty. *Analysis of Lithium-Ion Battery Degradation During Thermal Aging*. Nov 2000.

[52] S. Kalnaus, K. Rhodes, and C. Daniel. A study of lithium ion intercalation induced fracture of silicon particles used as anode material in li-ion battery. *Journal of Power Sources*, 196(19):8116–8124, 2011.

[53] Sergey Korotov and Tomáš Vejchodský. A comparison of simplicial and block finite elements. In Gunilla Kreiss, Per Lötstedt, Axel Målqvist, and Maya Neytcheva, editors, *Numerical Mathematics and Advanced Applications 2009*, pages 533–541. Springer Berlin Heidelberg, 2010.

[54] D. Kuzmin, M. J. Shashkov, and D. Svyatskiy. A constrained finite element method satisfying the discrete maximum principle for anisotropic diffusion problems. *J. Comput. Phys.*, 228(9):3448–3463, May 2009.

[55] Dmitri Kuzmin. *A Guide to Numerical Methods for Transport Equations*. Friedrich-Alexander-Universität Erlangen-Nürnberg, 2010.

[56] Wei Lai and Francesco Ciucci. Derivation of micro/macro lithium battery models from homogenization. *Transport in Porous Media*, 88:249–270, 2011.

[57] Wei Lai and Francesco Ciucci. Mathematical modeling of porous battery electrodes – Revisit of Newman's model. *Electrochimica Acta*, 56(11):4369 – 4377, 2011.

[58] Arnulf Latz and Jochen Zausch. Thermodynamic consistent transport theory of li-ion batteries. *Journal of Power Sources*, 196(6):3296–3302, 2011.

[59] Arnulf Latz, Jochen Zausch, and Oleg Iliev. Modeling of species and charge transport in li-ion batteries based on non-equilibrium thermodynamics. In *Proceedings of the 7th international conference on Numerical methods and applications*, NMA'10, pages 329–337, Berlin, Heidelberg, 2011. Springer-Verlag.

[60] E. H. Lee. Elastic-plastic deformation at finite strains. *J. Appl. Mech.*, 36:1–6, 1969.

[61] G. B. Less, J. H. Seo, S. Han, A. M. Sastry, J. Zausch, A. Latz, S. Schmidt, C. Wieser, D. Kehrwald, and S. Fell. Micro-scale modeling of li-ion batteries: Parameterization and validation. *Journal of The Electrochemical Society*, 159(6):A697–A704, 2012.

[62] Pimpa Limthongkul, Young-Il Jang, Nancy J. Dudney, and Yet-Ming Chiang. Electrochemically-driven solid-state amorphization in lithium-silicon alloys and implications for lithium storage. *Acta Materialia*, 51(4):1103 – 1113, 2003.

[63] David Linden and Thomas B. Reddy. *Handbook of Batteries*. McGraw-Hill Professional, 3rd edition, 2001.

[64] Stanley B. Lippman. *Inside the C++ Object Model*. Addison-Wesley, 1996.

[65] Xiao Hua Liu, He Zheng, Li Zhong, Shan Huang, Khim Karki, Li Qiang Zhang, Yang Liu, Akihiro Kushima, Wen Tao Liang, Jiang Wei Wang, Jeong-Hyun Cho, Eric Epstein, Shadi A. Dayeh, S. Tom Picraux, Ting Zhu, Ju Li, John P. Sullivan, John Cumings, Chunsheng Wang, Scott X. Mao, Zhi Zhen Ye, Sulin Zhang, and Jian Yu Huang. Anisotropic swelling and fracture of silicon nanowires during lithiation. *Nano Letters*, 11(8):3312–3318, 2011. PMID: 21707052.

[66] LLNL. VisIt. `https://wci.llnl.gov/simulation/computer-codes/visit/`.

[67] John Newman and Karen E. Thomas-Alyea. *Electrochemical Systems*. Wiley-Interscience, 3rd edition, 2004.

[68] NTSB. Chairman's closing remarks, boeing 787 battery investigative hearing. `http://www.ntsb.gov/news/speeches/DHersman/Pages/Chairmans_Closing_Remarks_Boeing_787_Battery_Investigative_Hearing.aspx`, April 2013. Accessed: 2015-01-15.

[69] J.M. Ortega and W.C. Rheinboldt. *Iterative Solution of Nonlinear Equations in Several Variables*. SIAM, 1970.

[70] Carolyn R. Pals and John Newman. Thermal modeling of the lithium/polymer battery .1. discharge behavior of a single-cell. *Journal of the Electrochemical Society*, 142(10):3274–3281, 1995.

[71] Sean Parent. Value semantics and concepts-based polymorphism. Presented at C++Now, 2012.

[72] P. Popov, Y. Vutov, S. Margenov, and O. Iliev. Finite volume discretization of equations describing nonlinear diffusion in li-ion batteries. In *Proceedings of the 7th international conference on Numerical methods and applications*, NMA'10, pages 338–346, Berlin, Heidelberg, 2011. Springer-Verlag.

[73] S. Prussin. Generation and distribution of dislocations by solute diffusion. *Journal of Applied Physics*, 32(10):1876–1881, 1961.

[74] Lin Rao and John Newman. Heat-generation rate and general energy balance for insertion battery systems. *Journal of The Electrochemical Society*, 144(8):2697–2704, 1997.

[75] Junuthula N. Reddy. *An Introduction to the Finite Element Method*. McGraw-Hill, Inc., 2nd edition, 1993.

[76] Michael Renardy and Robert Rogers. *An Introduction to Partial Differential Equations*. Springer, 2nd edition, 2004.

[77] Reuters. Boeing dreamliners grounded worldwide on battery checks. `http://www.reuters.com/article/2013/01/17/us-boeing-dreamliner-idUSBRE90F1N820130117`, January 2013. Accessed: 2015-01-15.

[78] Ill Ryu, Jang Wook Choi, Yi Cui, and William D. Nix. Size-dependent fracture of si nanowire battery anodes. *Journal of the Mechanics and Physics of Solids*, 59(9):1717 – 1730, 2011.

[79] Yousef Saad. *Iterative Methods for Sparse Linear Systems*. SIAM, 2nd edition, 2003.

[80] Shriram Santhanagopalan, Qi Zhang, Karthikeyan Kumaresan, and Ralph E. White. Thermal Properties of Battery Systems. *Journal of The Electrochemical Society*, 155(4):A345–A353, 2008.

[81] Fraunhofer SCAI. SAMG. `http://www.scai.fraunhofer.de/en/business-research-areas/numerical-software/products/samg.html`.

[82] Joachim Schöberl. Netgen Mesh Generator. `http://sourceforge.net/projects/netgen-mesher/`.

[83] Joachim Schöberl. NETGEN - An advancing front 2D/3D-mesh generator based on abstract rules. *Comput.Visual.Sci*, 1:41–52, 1997.

[84] Vijay A. Sethuraman, Michael J. Chon, Maxwell Shimshak, Venkat Srinivasan, and Pradeep R. Guduru. In situ measurements of stress evolution in silicon thin films during electrochemical lithiation and delithiation. *Journal of Power Sources*, 195(15):5062–5066, 2010.

[85] Vivek Shenoy, P. Johari, and Y. Qi. Elastic softening of amorphous and crystalline li-si phases with increasing li concentration: A first-principles study. *Meeting Abstracts*, MA2010-02(11):1135, 2010.

[86] Gogi K. Singh, Gerbrand Ceder, and Martin Z. Bazant. Intercalation dynamics in rechargeable battery materials: General theory and phase-transformation waves in lifepo4. *Electrochimica Acta*, 53(26):7599–7613, 2008.

[87] William Stallings. *Computer Organization and Architecture*. Prentice Hall, 9th edition, 2012.

[88] Rastko Stojanovitch. On the stress relation in non-linear thermoelasticity. *International Journal of Non-Linear Mechanics*, 4(3):217 – 233, 1969.

[89] Bjarne Stroustrup. *The C++ Programming Language*. Addison-Wesley, 4th edition, 2013.

[90] Maxim Taralov. Mathematical Modeling of Electrochemical Processes in Li-ion Batteries with Thermic Effects. Master's thesis, Sofia Univeristy, 2011.

[91] Maxim Taralov, Vasilena Taralova, Peter Popov, Oleg Iliev, Arnulf Latz, and Jochen Zausch. On 2D Finite Element Simulation of a Thermodynamically Consistent Li-ion Battery Microscale Model. *Mathemathics in Industry*, pages 148–161, 2014.

[92] Karen E. Thomas and John Newman. Thermal modeling of porous insertion electrodes. *Journal of The Electrochemical Society*, 150(2):A176–A192, 2003.

[93] NY Times. Sony warns some new laptop batteries may catch fire. `http://www.nytimes.com/2014/04/12/technology/sony-warns-some-new-laptop-batteries-may-catch-fire.html?_r=0`, April 2014. Accessed: 2015-01-15.

[94] H.A. van der Voorst. Bi-CGSTAB: A fast and smoothly converging variant of Bi-CG for the solution of nonsymmetric linear systems. *SIAM Journal on Scientific and Statistical Computing*, 13:631–644, 1992.

[95] Richard Varga. On a discrete maximum principle. *SIAM Journal on Numerical Analysis*, 3(2):355–359, 1966.

[96] J. Vetter, P. Novk, M.R. Wagner, C. Veit, K.-C. Mller, J.O. Besenhard, M. Winter, M. Wohlfahrt-Mehrens, C. Vogler, and A. Hammouche. Ageing mechanisms in lithium-ion batteries. *Journal of Power Sources*, 147(1-2):269 – 281, 2005.

[97] Chia-Wei Wang and Ann Marie Sastry. Mesoscale modeling of a li-ion polymer cell. *Journal of The Electrochemical Society*, 154(11):A1035–A1047, 2007.

[98] Jiang Wei Wang, Yu He, Feifei Fan, Xiao Hua Liu, Shuman Xia, Yang Liu, C. Thomas Harris, Hong Li, Jian Yu Huang, Scott X. Mao, and Ting Zhu. Two-phase electrochemical lithiation in amorphous silicon. *Nano Letters*, 13(2):709–715, 2013. PMID: 23323743.

[99] William H. Woodford, W. Craig Carter, and Yet-Ming Chiang. Strategies to avert electrochemical shock and their demonstration in spinels. *Journal of The Electrochemical Society*, 161(11):F3005–F3009, 2014.

[100] Hui Xia, Zhentao Luo, and Jianping Xie. Nanostructured limn2o4 and their composites as high-performance cathodes for lithium-ion batteries. *Progress in Natural Science: Materials International*, 22(6):572 – 584, 2012.

[101] Fuqian Yang. Interaction between diffusion and chemical stresses. *Materials Science and Engineering: A*, 409(1–2):153–159, 2005. Micromechanics of Advanced Materials {II} {TMS} 2005 Annual Meeting, in Honour of James C.M. Li's 80th Birthday.

[102] Fuqian Yang. Diffusion-induced stress in inhomogeneous materials: concentration-dependent elastic modulus. *Science China Physics, Mechanics and Astronomy*, 55(6):955–962, 2012.

[103] Shiquan Zhang, Oleg Iliev, Sebastian Schmidt, and Jochen Zausch. Comparison of two approaches for treatment of the interface conditions in FV discretization of pore scale models for Li-Ion batteries. 78:731–738, 2014.

[104] Xiangchun Zhang, Ann Marie Sastry, and Wei Shyy. Intercalation-induced stress and heat generation within single lithium-ion battery cathode particles. *Journal of The Electrochemical Society*, 155(7):A542–A552, 2008.

[105] Xiangchun Zhang, Wei Shyy, and Ann Marie Sastry. Numerical simulation of intercalation-induced stress in li-ion battery electrode particles. *Journal of The Electrochemical Society*, 154(10):A910–A916, 2007.

[106] Kejie Zhao, Matt Pharr, Shengqiang Cai, Joost J. Vlassak, and Zhigang Suo. Large plastic deformation in high-capacity lithium-ion batteries caused by charge and discharge. *Journal of the American Ceramic Society*, 94(S1):S226–S235, 2011.

[107] Kejie Zhao, Matt Pharr, Joost J. Vlassak, and Zhigang Suo. Fracture of electrodes in lithium-ion batteries caused by fast charging. *Journal of Applied Physics*, 108(7):–, 2010.

[108] Kejie Zhao, Matt Pharr, Joost J. Vlassak, and Zhigang Suo. Inelastic hosts as electrodes for high-capacity lithium-ion batteries. *Journal of Applied Physics*, 109(1):–, 2011.

[109] Olgierd C. Zienkiewicz, Robert L. Taylor, and P. Nithiarasu. *The Finite Element Method for Fluid Dynamics*. Elsevier Butterworth-Heinemann, 6th edition, 2005.

Academic Career

10/2011–05/2015	PhD student at Fraunhofer Institute for Industrial Mathematics (ITWM), Department Flow and Material Simulation, and Technical University of Kaiserslautern, Department of Mathematics, Kaiserslautern, Germany
04/2013	Visiting researcher at the Institute for Scientific Computation (ISC) at Texas A&M University, College Station, USA
07/2011–10/2011	Researcher at Fraunhofer Institute for Industrial Mathematics (ITWM) with scholarship awarded by the German Academic Exchange Service (Deutscher Akademischer Austauschdienst, DAAD), Kaiserslautern, Germany
03/2011–07/2011	Mathematician, working on the international project "IterUpscale - FSI", Bulgarian Academy of Sciences, Institute for Information and Communication Technologies
08/2010–10/2010	Internship at Fraunhofer Institute for Industrial Mathematics (ITWM), Kaiserslautern, Germany
01/2010–06/2010	Mathematician, working on the international project "IterUpscale - FSI", Bulgarian Academy of Sciences, Institute for Information and Communication Technologies
11/2009–06/2011	Master's degree in Computational Mathematics and Mathematical Modeling, University of Sofia "St. Kliment Ohridski", Faculty of Mathematics and Informatics, Sofia, Bulgaria
10/2005–09/2009	Bachelor's degree in Applied Mathematics, University of Sofia "St. Kliment Ohridski", Faculty of Mathematics and Informatics, Sofia, Bulgaria

Akademischer Werdegang

10/2011–05/2015	Promotion am Fraunhofer-Institut für Techno- und Wirtschaftsmathematik (ITWM), Abteilung Strömungs- und Materialsimulation, und Technische Universität Kaiserslautern, Fachbereich Mathematik, Kaiserslautern, Deutschland
04/2013	Gastwissenschaftler am Institute for Scientific Computation (ISC) at Texas A&M University, College Station, USA
07/2011–10/2011	DAAD-Stipendiat am Fraunhofer-Institut für Techno- und Wirtschaftsmathematik (ITWM) Kaiserslautern, Deutschland
03/2011–07/2011	Mathematiker, Bulgarische Akademie der Wissenschaften, Institute for Information and Communication Technologies
08/2010–10/2010	Forschungsaufenthalt am Fraunhofer-Institut für Techno- und Wirtschaftsmathematik (ITWM), Kaiserslautern, Deutschland
01/2010–06/2010	Mathematiker, Bulgarische Akademie der Wissenschaften, Institute for Information and Communication Technologies
11/2009–06/2011	Master in Numerische Mathematik und Mathematische Modellierung, Universität zu Sofia "St. Kliment Ohridski", Fachbereich Mathematik und Informatik, Sofia, Bulgarien
10/2005–09/2009	Bachelor in Angewandte Mathematik, Universität zu Sofia "St. Kliment Ohridski", Fachbereich Mathematik und Informatik, Sofia, Bulgarien